Mechanically tuned conductivity in piezoelectric semiconductors

Vom Fachbereich Material- und Geowissenschaften
zur Erlangung des akademischen Grades Doktor Ingenieur (Dr.-Ing.)
genehmigte Dissertation von Peter Keil aus Darmstadt

1. Gutachten: Prof. Dr. Jürgen Rödel
2. Gutachten: Prof. Dr. Andreas Klein

Februar 2019 – Darmstadt – D17

TECHNISCHE
UNIVERSITÄT
DARMSTADT

Mechanically tuned conductivity in piezoelectric semiconductors

Genehmigte Dissertation von Peter Keil aus Darmstadt

1.Gutachten: Prof. Dr. Jürgen Rödel
2. Gutachten: Prof. Dr. Andreas Klein

Tag der Einreichung: 08.02.2019
Tag der Prüfung: 20.03.2019

Fachbereich Material- und Geowissenschaften
Februar 2019 – Darmstadt – D 17

Thesis Statement pursuant to § 22 paragraph 7 and § 23 paragraph 7 of APB TU Darmstadt

I herewith formally declare that I, Peter Keil, have written the submitted thesis independently pursuant to § 22 paragraph 7 of APB TU Darmstadt. I did not use any outside support except for the quoted literature and other sources mentioned in the paper. I clearly marked and separately listed all of the literature and all of the other sources which I employed when producing this academic work, either literally or in content. This thesis has not been handed in or published before in the same or similar form.

In the submitted thesis the written copies and the electronic version for archiving are pursuant to § 23 paragraph 7 of APB identical in content.

Date: Signature:

Table of content

List of figures

List of symbols

a, c	Lattice constants of the hexagonal wurtzite structure
α	Coefficient of nonlinearity (varistor)
α_{CPE}	CPE parameter
A^*	Richardson constant
C	Capacity
C_{Int}	Interface capacitance
c_{ijkl}	Elastic stiffness coefficient
d_{ijk}	Piezoelectric stress coefficient
$\Delta\varPhi_{DSB}$	Change in double Schottky barrier height
$\Delta\varPhi_{SB}$	Change in Schottky barrier height
e_{ijk}	Piezoelectric strain coefficient
ε_0	Vacuum permittivity
ε_{Int}	Relative permittivity of interface region
ε_r	Relative permittivity
ξ	Difference between Fermi-level and CBM
ϵ_ξ	Position of Fermi-level with respect to CBM
E	Electric field
E_A	Activation energy
E_{CBM}	Energetic position of conduction band maximum
E_D	Energetic position of donor states
E_F	Energetic position of the Fermi-level
E_{Vac}	Vacuum energy
E_{VBM}	Energetic position of valence band minimum
$f(E)$	Fermi-level distribution
$\varPhi_{DSB}$	Double Schottky barrier height
$\varPhi_M$	Metal work function
$\varPhi_{SB}$	Schottky barrier height
$\varPhi_S$	Semiconductor work function
δ_{Gap}	Thickness of interfacial layer (Schottky contact)
G	Conductance
$\delta(x)$	Dirac delta function
δ_{Gap}	Thickness of interfacial gap

I	Current
$I(Z), Z'$	Imaginary part of impedance
J	Current density
$J_{M \rightarrow SC}$	Current density flowing from the metal to the semiconductor
$J_{SC \rightarrow M}$	Current density flowing from the semiconductor to the metal
J_{TE}	Thermally emitted current density
J_0	Saturation current density
k	Boltzmann constant
m_0	Electron rest mass
μ_n	Electron mobility
n	Concentration of free electrons
$\boldsymbol{n}$	Grain boundary normal vector
ν	Frequency
η	Ideality factor
N_D	Donor state density
N_i	Interfacial defect state density
ξ_i	Fermi-level at varistor interface
P	Piezoelectric polarization
P_S	Spontaneous polarization
q	Elementary charge of an electron
Q	Electric charge
Q_{GS}	Gap state charge
Q_i	Bound interfacial sheet charge
Q_M	Negative sheet charge within metal electrode
Q_P	Piezoelectric polarization charge
Q_{SC}	Semiconductor charge within depletion region
R	Resistance
R_{Bulk}	Bulk resistance
R_{Int}	Interface resistance
$Re(Z), Z'$	Real part of impedance
$\rho(x)$	Spatial charge distribution
ρ_{Piezo}	Piezoelectric charge density
S_{kl}	Strain tensor
σ_{el}	Electrical conductivity
σ_{ij}	Mechanical stress tensor

T	Temperature
$\Theta(x)$	Heaviside step function
u	Internal cell parameter of the hexagonal wurtzite structure
V	Voltage
V_B	Breakdown voltage of double Schottky barrier
V_{Bi}	Built-in potential
V_{Int}	Voltage drop across interface
V_{rms}	Root mean square of probe signal
ω	Angular frequency
W_D	Depletion region width
W_{Dl}	Depletion region width within left grain
W_{Dr}	Depletion region width within right grain
W_{Piezo}	Piezoelectric charge distribution width
χ	Electron affinity of a semiconductor
Z	Impedance

List of abbreviations

1-D	One-dimensional
2-D	Two-dimensional
3-D	Three-dimensional
2DEG	Two-dimensional electron gas
ac	Alternating current
BSE	Backscatter electron mode
CBM	Conduction band minimum
CNL	Charge neutrality level
CPE	Constant phase element
dc	Direct current
DOS	Density of states
DSB	Double Schottky barrier
EDS	Energy-dispersive X-Ray spectroscopy
FE	Ferroelectric
GB	Grain boundary
HAADF	High-angle annular dark field
HFET	Heterojunction field-effect transistor
ITO	Indium tin oxide
M	Metal
PZT	Lead zirconate titanate
SAED	Selected area electron diffraction
SC	Semiconductor
SEM	Scanning electron microscopy
TEM	Transmission electron microscopy
VAC	Vacuum
VBM	Valence band maximum

Abstract

In this work, different ZnO interfaces were studied with respect to their performance in piezotronic applications. The electrical conductivity across metal – ZnO Schottky contacts as well as varistor-type ZnO-ZnO interfaces was measured as a function of uniaxial compressive stress. In addition, temperature-dependent measurements of the direct piezoelectric response of ZnO single crystals with and without the existence of a highly resistive space charge region were performed.

The electrical conductivity across potential barriers at metal – ZnO Schottky contacts on either the Zn- or O-terminated surface of a bulk ZnO single crystal was measured under increasing uniaxial compressive stress. The generation of negative or positive piezoelectric polarization charges was found to increase or decrease the Schottky barrier height depending on the sign of the piezoelectric charge. The evolution of potential barrier height with increasing amount of positive piezoelectric charge was determined from *I-V* deconvolution techniques and allowed a comparison of the experimental data with different theoretical models. Measurements were performed on bulk ZnO single crystals to overcome shortcomings in existing literature in which studies are mainly based on metal-ZnO nanostructure contacts. Thereby the fundamental concept of the piezotronic effect could be confirmed and the current understanding is extended.

Direct piezoelectric measurements on bulk ZnO single crystals with and without the existence of a highly resistive space charge region were performed as a function of temperature and loading frequency. A decreasing number of free charge carriers with decreasing temperature revealed a correlation between free charge carrier density and screening of the piezoelectric potential. An increase in attainable piezoelectric polarization with decreasing temperature was evident for the crystals with and without space charge region. In addition, the generation of a highly resistive space charge region in the vicinity of a Schottky contact allowed a measurement of the piezoelectric potential already at room temperature and for low loading frequencies. The shift of the attainable piezoelectric response to higher temperatures and lower loading frequencies due to the existence of a depletion region is of great importance for piezotronic applications.

Besides metal-ZnO contacts, ZnO bicrystal interfaces were prepared by epitaxial solid-state transformation. The preparation process allows for both, a defined orientation of the

polarization vector as well as tailoring of the defect state density at the ZnO-ZnO interface. Consequently, the interaction between positive and negative piezoelectric charges and the electrostatic potential barrier at the bicrystal interface could be systematically investigated. Stress-dependent conductivity measurements revealed a decreasing barrier for positive piezoelectric charges and an increasing potential barrier for negative piezoelectric charges. The magnitude of this coupling was compared to theoretical models as well as to experimental results obtained on metal-ZnO Schottky contacts. In comparison to the Schottky contact, potential barriers at ZnO-ZnO interfaces featured a much higher stress sensitivity. For the lowering case by positive piezoelectric charges an almost complete extinction of the electrostatic potential barrier could be achieved. The obtained results demonstrate the potential of individual ZnO-ZnO interfaces as promising alternative to metal-ZnO Schottky contacts in future piezotronic applications.

By interrupting the epitaxial solid-state transformation process at different times during the high temperature treatment, single crystal – polycrystal structures with varying amount of remaining polycrystalline material in between two well oriented single crystals were prepared. Temperature-dependent conductivity measurements were applied to determine the influence of the high temperature treatment on the potential barrier height at varistor-type interfaces during bicrystal fabrication by epitaxial solid-state transformation. Furthermore, stress-dependent *I*-*V* measurements revealed extremely high stress sensitivities for structures with intermediate times of high temperature treatment. These measurements close the gap between piezotronic systems based on polycrystalline varistor ceramics and individual bicrystal interfaces and reveal the future potential of microstructural engineering for the development of varistor-based piezotronic devices.

1. Introduction

The piezotronic effect describes the interaction between two fundamental physical properties. Piezoelectric and semiconducting properties are coupled to tune the electrical transport across contact interfaces like metal-semiconductor or semiconductor-semiconductor junctions. The term "*piezotronics*" was introduced in 2007 by Zhong Lin Wang[1] to cumulate innovative applications based on the modification of semiconducting properties by strain induced piezoelectric polarization under one generic term. In the following years the piezotronic effect gained considerable interest within the scientific community with a large number of publications on possible applications like energy harvesters, strain triggered transistors or strain sensors.[2, 3] Most publications focus on zinc oxide (ZnO)-based devices because of its comparably high piezoelectric coefficient and semiconducting properties. Furthermore, ZnO can be easily fabricated in a large variety of nanostructures and high quality ZnO single crystals are available.[4, 5] Similar physical mechanisms, however, were already previously described for several semiconductor and ferroelectric contact interfaces.

In wurtzite group-III nitrides, such as GaN, polarization effects on the performance of electronic and optoelectronic device properties were studied since the 1990s.[6] One prominent example is the formation of a 2-D electron gas (2DEG) by polarization charges at GaN-based heterojunctions.[7, 8] Furthermore, it has been demonstrated that Schottky contacts to GaN are influenced by spontaneous or piezoelectric polarization.[9] Polarization effects can increase the Schottky barrier height in GaN-based heterojunction field-effect transistors (HFET) leading to a reduced reverse-bias leakage and forward-bias current which improves the performance of the transistor.[10] In the HFET, static piezoelectric polarization charges in epitaxial grown GaN are utilized to optimize the Schottky barrier height during device fabrication. However, a dynamic piezoelectric polarization charge can be induced by external mechanical strain, opening the possibility to control electrical transport by mechanical stimuli.[11] A similar effect has been observed for a Schottky contact to piezoelectric GaAs.[12] The mechanism is comparable to the fundamental theory of piezotronic devices based on ZnO – metal contacts, which are in detail reviewed within chapter 2.2. Strittmatter *et al.*[13] reported on the strain sensing capability of GaN Schottky diodes, where a sinusoidal mechanical load generates piezoelectric polarization charges within the depletion region of the Schottky contact. Due to the reduced free charge carrier density within the depletion region, the piezoelectric potential cannot be screened and a voltage signal can be detected with a suitable readout circuit. The concept is analogous to the basic principle of piezotronic energy harvesters.[14]

As piezoelectric polarization modifies the Schottky barrier height at metal-semiconductor interfaces, ferroelectric polarization is capable to alter the potential barrier height at ferroelectric-metal heterojunctions.[15, 16] Hence, in metal-ferroelectric-metal (M-FE-M) structures a diode like rectifying behavior can be induced by ferroelectric polarization. The diode like behavior results from a decrease in Schottky barrier height at the metal contact with positive ferroelectric polarization and an increase in Schottky barrier height of the metal contact with negative polarization. Polarization in ferroelectric materials can be switched by the application of a sufficiently large electric field resulting in a switched diode characteristic with feasible application as ferroelectric-resistive memory.[17-19] In M-FE-M junctions with ultrathin FE, electrons can tunnel through the insulating FE material. For metal electrodes with different screening length, the electrostatic potential profile across the tunnel junction can be modified by the direction of ferroelectric polarization which results in a change of electrical conductivity by orders of magnitude.[20, 21] By replacing the classical metal electrodes with ferromagnetic electrodes spin-polarized transport through the tunnel junction adds an additional degree of freedom, in principle enabling the four-state memory device.[22]

In 1976 Wong and Bundy[23] discovered a pronounced change in electrical conductivity of ZnO-based varistor ceramics under the application of mechanical stress. Emtage[24] attributed the conductivity change to the interaction between electrostatic potential barriers at the grain boundaries of the electroceramic and stress-induced piezoelectric polarization charges. The increase in electrical conductivity due to mechanical stress was mainly treated as an unwanted effect since it decreases figures of merit for varistor ceramics when used as surge protection. Internal stresses, resulting from anisotropy or mismatch in thermal expansion, increase the leakage current and decrease the coefficient of nonlinearity.[25] As a consequence of the high interest in piezotronic applications, the modulation of electrical conductivity in polycrystalline varistor ceramics by mechanical stress experienced new attention.[26, 27] A major part of these works is based on varistor-like potential barriers, therefore the barrier formation process and their modification by piezoelectric polarization are reviewed in chapter 2.3.

Regardless of the large number of research areas describing the coupling of piezoelectric charge and semiconducting properties, great interest in piezotronic devices was triggered in 2006 by two publications from Z.L. Wang's group, outlining the potential of the interaction between piezoelectric and semiconducting properties in ZnO nanowire structures.[28, 29] The first publication proposed a nanogenerator based on ZnO nanowires where a mechanical deflection of the nanowire generates piezoelectric polarization which can induce a current flow through an external circuit. To improve power output vertical and lateral alignment of ZnO nanowire arrays was applied.[30] Prototypes were fabricated which demonstrate the capability of harvesting abundant mechanical energy from the environment such as vibrational energy (e.g. sound)[31] or from the human body (e.g. muscle contraction)[32] opening the pathway to self-powered sensor networks. The second publication in 2006 proposed the use of stress-induced piezoelectric polarization within the ZnO nanowire to tune the electrical conductivity through the nanowire-metal structure. The concept can be seen as stress-triggered piezoelectric field-effect transistor where the mechanical stress substitutes for the gate voltage within a classical field-effect transistor.[33] Besides ZnO nanostructures, piezotronic transistor devices based on ZnO thin films or 2-D MoS_2 have been demonstrated.[34, 35] The working principle of piezotronic transistor devices is the interaction between stress-induced piezoelectric polarization charges and the Schottky barrier height at metal contacts which defines the electrical conductivity across the metal-semiconductor junction.[36] A straight forward application besides logic devices is to utilize the piezotronic modulation of electrical conductivity for strain sensing.[37, 38] Large-area patterning of ZnO nanowire stress sensors allowed lateral pressure mapping with possible application as artificial skin for next generation robotics and human-computer interfacing.[39, 40]

Despite the large interest in piezotronic applications and the multitude of proposed functional devices, several questions remain unresolved. Until now, most publications utilize metal-ZnO nanowire Schottky contacts as piezotronic element leading to inhomogeneous distributions of the piezoelectric potential within the nanostructures. Furthermore, Schottky contacts are often applied on both sides and even partially on basal planes of the nanostructures which makes it difficult to fully explore the physical mechanism behind the piezotronic effect. Therefore, in this work, the piezotronic effect will be characterized on bulk ZnO single crystals with only one Schottky contact on either the Zn- or O-terminated surface of a single crystal. Further controversial discussions came up due to a possible screening of the piezoelectric potential by free charge carriers within the ZnO. This controversy will be addressed by direct piezoelectric measurements as a function of temperature and loading frequency on ZnO single crystals with and without a highly resistive depletion region. Besides the metal-ZnO Schottky contact, doped ZnO-ZnO interfaces, as they can be found in polycrystalline varistor ceramics demonstrated a pronounced stress sensitivity. Therefore, individual bicrystal interfaces have been prepared within this work and tested for their piezotronic performance. The new approach may combine the high stress sensitivity of piezotronic devices based on polycrystalline varistor ceramics and the predictable electrical properties of individual Schottky contacts.

2. Theory and literature review

2.1. ZnO as piezotronic material

The piezotronic effect relies on the coupling of piezoelectric and semiconducting properties to tune the electrical transport across contact interfaces. Piezoelectric properties are related to the crystal structure of a material and can be observed in crystals of non-centrosymmetric point groups. Relevant piezoelectric materials are often of perovskite structure like lead zirconate titanate (PZT) or barium titanate ($BaTiO_3$), which typically show an electrically insulating behavior.[41] On the other hand, the classical semiconductor material silicon (Si) does not show piezoelectric properties due to its centrosymmetric crystal structure.[42] Wurtzite structured materials like ZnO, InN and GaN combine semiconducting and piezoelectric properties and are therefore the materials of choice for piezotronic applications. Most piezotronic systems are based on ZnO due to its good piezoelectric properties and the possibility to fabricate it in a large variety of nanostructures, thin films, single crystals or polycrystalline ceramics.[4, 5, 43-47]

In this chapter, the crystal structure as well as the piezoelectric and semiconducting properties of ZnO are reviewed.

2.1.1. Crystal structure of ZnO

Possible crystal structures of ZnO are the cubic zinc blende, rocksalt, and hexagonal wurtzite structure.[48] While the zinc blende structure may only be observed by the growth of ZnO on cubic substrates and the rocksalt or NaCl structure being obtained under high pressure, the thermodynamically stable structure under ambient condition is the wurtzite crystal structure.[49-51] Wurtzite has a hexagonal unit cell and belongs to the $P6_3mc$ space group in Hermann-Mauguin notation. Figure 2-1 shows the wurtzite crystal structure with its two lattice parameters a and c. The c/a-ratio of ZnO is reported to be smaller than the ideal value for an wurtzite structure of 1.633.[52, 53] Hence, the internal cell parameter u which defines the anion-cation bond length along the c-direction is slightly larger than the ideal one. The Zn^{2+} cations and O^{2-} anions each build a hexagonal close-packed sublattice including four atoms per unit cell. The Zn^{2+} cations are surrounded by four O^{2-} anions, which are positioned at the edges of a tetrahedron. The tetrahedral coordination is typical for the sp^3 covalent bonding nature, but due to the high difference in electronegativity between Zn and O, ZnO features a significant ionic character.[54]

Due to the lack of inversion symmetry of the wurtzite-type crystal structure, ZnO possesses a polarity along the c-axis ([0001] direction). Hence, the surfaces perpendicular to the c-axis are either Zn-terminated, labeled as (0001) plane or O-terminated, labeled as $(000\bar{1})$ plane. The convention is that the [0001] direction points from the $(000\bar{1})$ plane to the (0001) plane, which is defined as the positive z-direction. Throughout this work, the (0001) plane will be referred to as Zn-polar and the $(000\bar{1})$ plane as O-polar surface.

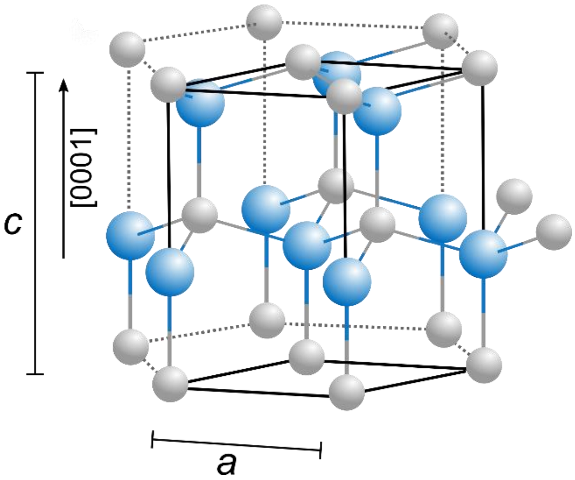

Figure 2-1: Schematic representation of the wurtzite crystal structure of ZnO with the lattice constants a and c. The polar c-axis [0001] pointing from the O-polar plane (blue) towards the Zn-polar plane (grey).

Many properties of ZnO like crystal growth, etch rate, spontaneous polarization and piezoelectricity depend on its crystal structure and polarity. Crystal growth rate along the [0001] direction is the fastest, while the $[000\bar{1}]$ direction shows the slowest growth rate.[55, 56] On the other hand, it was shown that the O-polar surface is more rapidly etched than the Zn-polar surface if an oxidizing etchant is used.[57] Furthermore, a characteristic hillock morphology appears on etched O-polar surfaces, while on the Zn-polar surface, only dislocation etch pits occur. This fundamental difference in etching behavior can be used to determine the orientation of the polar axis in a single crystal. A detailed discussion on piezoelectricity and spontaneous polarization in ZnO is given in chapter 2.1.2.

2.1.2. Piezoelectric properties of ZnO

When a mechanical stress σ is applied to a solid material, it responds with a proportional strain S. Within the elastic limits, S and σ are related by the elastic stiffness coefficient C_{ijkl} as described by Hooke's law:

$$\sigma_{ij} = C_{ijkl}\, S_{kl}\,. \tag{2.1}$$

In a piezoelectric material, additional polarization charges are induced when the material is mechanically stressed, generating a potential difference within the material. The electric field originates from the deformation of the unit cell and a concurrent separation of the positive and negative centers of charge, which in turn results in the formation of dipole moments. In ZnO, the Zn^{2+} cations and the O^{2-} anions are coordinated tetrahedrally (Figure 2-2 (a)). When a mechanical stress is applied in the c-direction of the crystal, the centers of the Zn^{2+} cation and the O^{2-} anion sublattices are shifted relatively to each other. As a consequence, a dipole moment is induced along the c-axis of the ZnO crystal (Figure 2-2 (b)). In this configuration, negative polarization charges are generated on the Zn-polar surface while positive polarization charges are induced on the O-polar surface. A mechanical stress perpendicular to the c-axis results in an opposite relative shift of the positive and negative center of charge. Hence, the Zn-polar surface will be positively charged and the O-polar surface negatively (Figure 2-2 (c)). Throughout this work, the sign of the polarization charges is referred to as the ionic charge generated due to the stress-induced, relative displacement of ions within the crystal.

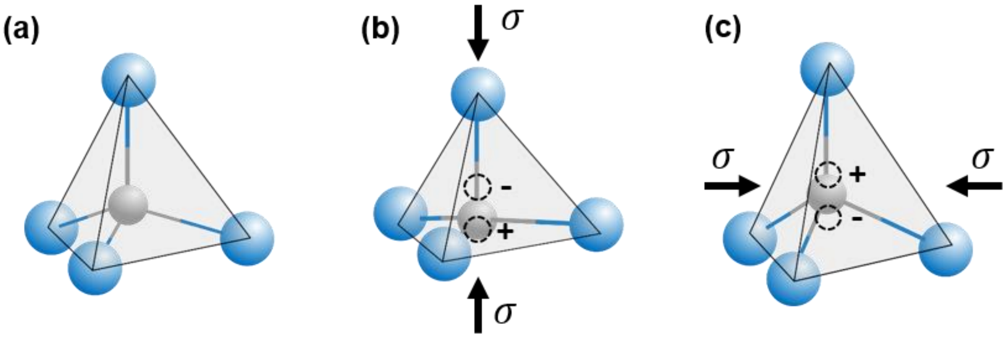

Figure 2-2: Atomic model of the tetrahedrally coordinated Zn^{2+} cations (grey) by O^{2-} anions (blue). The application of a mechanical stress along (b) or perpendicular (c) to the c-axis results in a relative shift of the cation and anion sublattices. As a consequence, a dipole moment along the c-direction is induced.

The generation of piezoelectric polarization by the application of a mechanical stress or strain is referred to as the *direct* piezoelectric effect. The piezoelectric stress coefficients d_{ijk} and strain coefficients e_{ijk} correlate the produced piezoelectric polarization (P_i) to the applied stress or strain:

$$P_i = d_{ijk}\sigma_{jk} = e_{ijk}S_{jk}\,. \tag{2.2}$$

When an external electric field (E) is applied to a piezoelectric crystal, the material produces strain. This effect is referred to as the converse piezoelectric effect:

$$S_{ij} = d_{ijk} \mathrm{E}_k \,. \tag{2.3}$$

Following the Voigt natation and under uniaxial stress, the three indices of the piezoelectric tensor (d_{ijk}) can be reduced to only two indices. The piezoelectric stress tensor (d_{ijk}) of wurtzite structured ZnO (space group *P6₃mc*), has 3 independent components d_{31}, d_{33}, and d_{15}:

$$d_{ijk} = \begin{pmatrix} 0 & 0 & 0 & 0 & d_{15} & 0 \\ 0 & 0 & 0 & d_{15} & 0 & 0 \\ d_{31} & d_{31} & d_{33} & 0 & 0 & 0 \end{pmatrix}. \tag{2.4}$$

The coefficients d_{31} and d_{33} relate the piezoelectric potential induced along the c-axis by a uniform stress in the basal plane (d_{31}) and along the c-direction (d_{33}), respectively. The d_{15} value describes the polarization induced perpendicular to the c-direction by a shear strain. The sign of the piezoelectric tensor is defined with the positive direction going along the c-axis from the cation to the anion.[47, 48]

However, the high intrinsic n-type conductivity of as grown ZnO can cancel the piezoelectric potential by redistribution of internal charges. This screening mechanism is detrimental of a detection of a piezoelectric potential and makes it difficult to measure the piezoelectric coefficients of ZnO.[58, 59] However, experimentally measured piezoelectric coefficients are available from a resonance-antiresonance method on lithium doped ZnO crystals. Hutson[60] reported piezoelectric coefficients of d_{33}=12 pC/N and d_{31}=-4.7 pC/N while Kobiakov[61] measured d_{33}=12.3 pC/N and d_{31}=-5.12 pC/N. Measurements were performed on lithium doped crystals since it reduces the free charge carrier density and thereby possible screening effects of polarization charge. The screening mechanism by free charge carriers not only complicates the determination of piezoelectric coefficients in ZnO but is also discussed as the limiting parameter when using ZnO in energy harvesting applications.[62] In addition, an influence of the free charge carrier density on piezotronic strain sensors has been reported, which will be further discussed in chapter 2.2.5. Besides reducing the internal charge carrier concentration, also the formation of a depletion region in the vicinity of a Schottky contact is known to prevent screening of the piezoelectric potential and can thereby improve the performance of piezotronic devices. Therefore, the influence of free charge carrier density as well as the existence of a depletion layer on the attainable piezoelectric properties of ZnO is experimentally addressed by measuring d_{31} and d_{33} as a function of temperature, frequency, and electrode material within chapter 5.2.

Spontaneous polarization

The wurtzite crystal is the structure with highest symmetry capable to exhibit spontaneous polarization (P_S).[63] Wurtzite structured ZnO fulfills all three requirements for the existence of spontaneous polarization, *i.e.* the presence of a unique polar axis, the deviation of the internal cell parameter u from its ideal value of 3/8 and the ionic bond character. The spontaneous polarization induces negative polarization charge on the Zn-polar surface, and positive polarization charges on the O-polar surface. Most reports on the magnitude of the spontaneous polarization in ZnO are based on *ab initio* calculations. Massidda *et al.*[64] report a value of $P_S = -0.047\ C/m^2$ while Dal Corso *et al.*[47] give a slightly higher value of $P_S = -0.057\ C/m^2$.

2.1.3. Semiconducting properties of ZnO

ZnO is a direct wide band gap semiconductor with a large free-exciton binding energy of about 60 meV.[65] The experimental band gap of ZnO is reported to be in the range of 3.3 to 3.44 eV.[65, 66] Large bulk ZnO single crystals are commercially available, often fabricated by the hydrothermal method.[67] A major issue for the development of semiconductor devices based on ZnO is the control over the electrical conductivity. ZnO crystals nearly always feature unintentional n-type conductivity for which native point defects and impurities are discussed as possible origin.[68] The tendency of ZnO to preferentially exhibit n-type conductivity makes it an interesting candidate for the fabrication of transparent conducting films, possibly replacing the widely used indium tin oxide films in such applications.[69]

On the other hand, reliable p-type doping is therefore a very difficult challenge where native point defects can act as compensating species for intentional acceptor doping.[70] Since defects define the electrical conductivity of ZnO single crystals, which in turn influences the performance of piezotronic devices, the role of important native point defects and impurities shall be briefly reviewed. In this chapter, numerous information was taken from review papers by A. Janotti and C.G. Van de Walle[71], M.D. McCluskey and S.J. Jokela[72], and P. Erhart *et al.*[73].

Oxygen vacancies

The oxygen vacancy (V_O) was historically often discussed as source of unintentional n-type conductivity in ZnO. The reason was, that V_O can act as donor and has a rather low formation energy compared to other donor type defects.[74] Recent theoretical and experimental work demonstrates, that V_O is more a deep than shallow donor.[75, 76] In addition, when the Fermi-level (E_F) moves close to the conduction band minimum (CBM) the formation energy of V_O increases and therefore cannot be responsible for the unintentional n-type conductivity.[74] For E_F moving close to the valence band maximum (VBM) which is the case for p-type condition the stable state for V_O is the double positively charged state ($V_O^{\cdot\cdot}$) with low formation energy.[75] Hence, V_O can act as compensating center in p-type ZnO.

Zinc vacancies

The removal of a Zn atom and formation of a Zn vacancy (V_{Zn}) results in a defect capable to accept two electrons. Consequently, V_{Zn} acts as acceptor. The formation energy of acceptor defects is low in n-type material (E_F close to CBM) and high in p-type material (E_F close to VBM). Therefore, V_{Zn} should play a minor role for p-type doping of ZnO but it has been proven to be one of the dominating centers for n-type compensation.[77]

Zinc interstitials

Zinc interstitials (Zn_i) donate two electrons to the conduction band and will therefore act as shallow donor. Like other donors, Zn_i features a high formation energy in n-type material.[78] Furthermore, they have low migration energy and become mobile at temperatures of around 130 K and therefore tend to diffuse out of the sample or to bind with other defects or impurities.[74, 79, 80] As a consequence of the high formation energy and low migration energy, Zn_i are very unlikely to significantly contribute to unintentional n-type conductivity in ZnO.

Other native defects

The formation energies of O and Zn antisites, and O interstitials are high, making them unlikely to be present in high concentrations at ambient condition.[74]

Since the above discussed native defects are shown not to be responsible for the observed unintentional n-type conductivity in as grown ZnO single crystals, impurities acting as shallow donors or acceptors are discussed in the following.

Donor impurities

An important group for donor doping in ZnO are the group-III elements such as boron, aluminum, gallium and indium. When incorporated on the Zn-site of the ZnO lattice, they act as shallow donor introducing one free electron to the conduction band at moderate temperatures. Doping strategies based on group-III elements are often applied in the field of ZnO-based transparent conductive thin films to increase the electrical conductivity.[81-83] But also in as grown single crystals, impurities of group-III elements are reported to be present, thus possibly contributing to the observed unintentional n-type conductivity.[84] Recently hydrogen is seen as a promising candidate to explain the background n-type conductivity in ZnO crystals. It has been shown that interstitial hydrogen does not behave as amphoteric dopant in ZnO, as it does in almost all other semiconductors, but that $H_i^{\cdot}$ is the only thermodynamically stable state. Hydrogen can therefore exclusively act as donor in ZnO.[85] Experimental evidence of hydrogen acting as donor dates back to the 1950s when Thomas and Lander[86] reported an increase in electrical conductivity of ZnO single crystals due to the incorporation of hydrogen into the ZnO lattice. Similar to group-III elements, hydrogen is known to be present in nominally undoped ZnO single crystals.[87]

Acceptor impurities

Despite the controversy about reproducible and stable p-type doping of ZnO, several acceptor states are known for ZnO which at least have a pronounced influence on the electrical properties by compensating n-type conductivity. Possible acceptor dopants are the group-I elements lithium (Li), sodium (Na) and potassium (K) as well as the group-V elements nitrogen (N), phosphorus (P) and arsenic (As). Li is known to be present in hydrothermally grown ZnO single crystals. In n-type ZnO, Li is incorporated on a Zn lattice site where it acts as shallow acceptor compensating n-type conductivity, Incorporation of Li is there a possible explanation for the observed low electrical conductivity in hydrothermally grown ZnO single crystals.[88] By reducing the free charge carrier density, Li doping enabled the first experimental measurements of the piezoelectric coefficients in ZnO as discussed in section 2.1.2.[60]

2.2. Metal-semiconductor contacts

Metal-semiconductor contacts play an important role in semiconductor industry either as rectifying “Schottky” or as low resistive “ohmic” contacts. Ohmic contacts are designed to have a polarity independent current-voltage (*I-V*) behavior with as low as possible contact resistance to get signals in and out of semiconductor devices. On the other hand, rectifying Schottky contacts are active elements with diode and transistor applications.[89] The same applies for piezotronic devices, where ohmic contacts are used to sense the piezotronic effect, while Schottky contacts are active elements which can be tuned by stress-induced piezoelectric polarization. In this chapter, the Schottky barrier formation and piezotronic modification of the potential barrier to ZnO shall be introduced.

2.2.1. Schottky barrier formation

Whether a metal-semiconductor contact shows rectifying or ohmic behavior is defined by the presence or absence of an electrostatic potential barrier at the interface. The potential barrier formation process was first described by Walter H. Schottky[90] and Neville F. Mott.[91] When a metal makes intimate contact to a semiconducting material, two requirements must be fulfilled. The Fermi-levels of both materials align, and the vacuum level has to be continuous. Consequently, the Schottky barrier height between a metal and n-type semiconductor (Φ_{SB}) is in first approximation defined by the difference between the metal work function (Φ_M) and the electron affinity of the semiconductor (χ):

$$\Phi_{SB} = \Phi_M - \chi \,. \tag{2.5}$$

Throughout this work, Φ_{SB}, Φ_M, and χ are defined as energy in electron volt (eV). The barrier formation process of a metal - n-type semiconductor contact is schematically depicted in Figure 2-3. In contact, electric charges redistribute between the metal and the semiconductor. To align the Fermi-levels, electrons flow from the semiconductor to the metal, leaving behind positively charged donor states within the depletion region of the width W_D. If the metal is seen as an ideal conductor, the electrons flown from the semiconductor to the metal, accumulate in a very narrow layer at the metal-semiconductor interface. The built-in potential (V_{Bi}) describes the potential across the depletion region within the semiconductor.

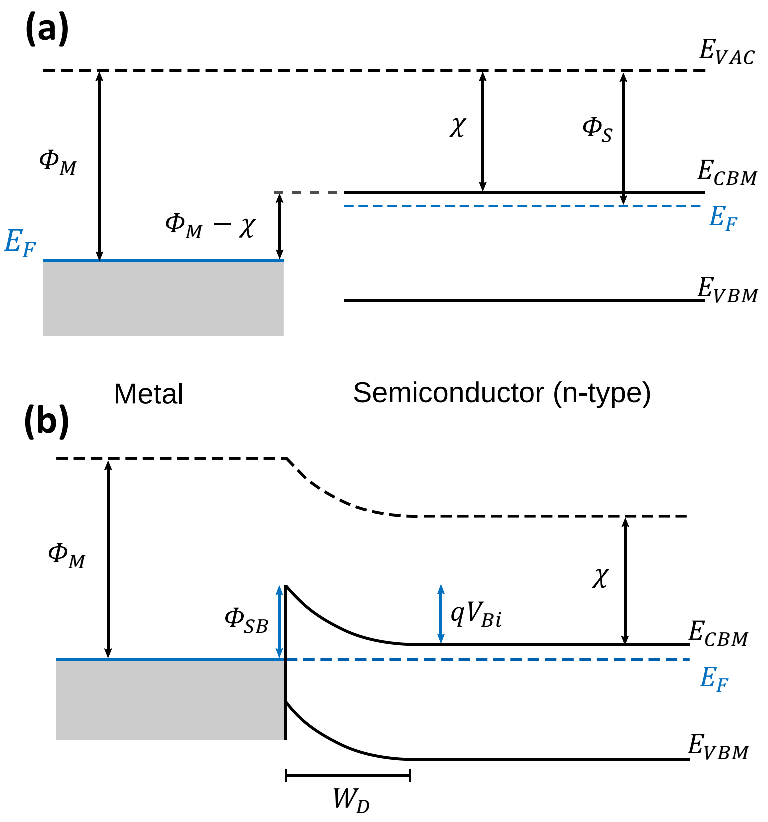

Figure 2-3: Barrier formation process of metal – n-type semiconductor Schottky contact. (a) Energy band diagram of metal and n-type semiconductor before contact. (b) Energy band diagram of the Schottky contact in thermal equilibrium (Redrawn after S.M. Sze[92]).

The electric field distribution (E(x)) and from this the potential variation ($V(x)$) can be calculated by solving the one-dimensional (1-D) Poisson equation:

$$\frac{\rho(x)}{\varepsilon_r \varepsilon_0} = \frac{d\mathrm{E}}{dx} = -\frac{d^2V}{dx^2}, \tag{2.6}$$

with $\rho(x)$ the charge distribution, ε_r the relative permittivity of the semiconductor and ε_0 the permittivity of vacuum. Under full depletion approximation, $\rho(x)$ equals the effective donor density qN_D for $0 < x < W_D$ while $\rho(x) = 0$ for $x \geq W_D$, with q being the elementary charge. The charge distribution of a Schottky contact under full depletion approximation is depicted in Figure 2-4 (a). The positive charge inside the depletion region of the semiconductor (Q_{SC}) is exactly the same as the negative sheet charge in the metal (Q_M). The resulting electric field distribution (Figure 2-4 (b)) as well as the potential (Figure 2-4 (c)) variation can be calculated using the Poisson equation (equation 2.6).

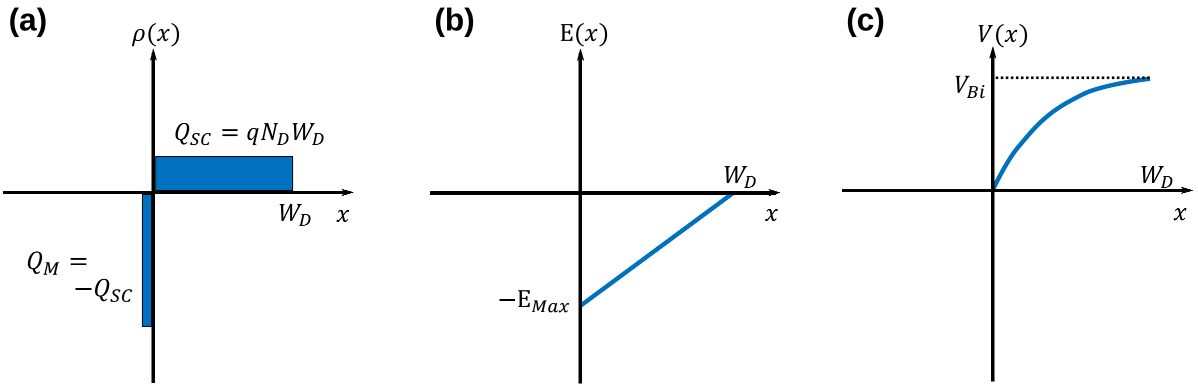

Figure 2-4: Charge distribution (a), electric field distribution (b) and potential variation (c) of a Schottky contact.

The electric field decreases linearly within the depletion region with the maximum electric field (E_{Max}) being located at the interface:

$$\mathrm{E}_{Max} = \frac{qN_DW_D}{\varepsilon_r\varepsilon_0}. \tag{2.7}$$

The width of the depletion layer is related to the built-in potential by,

$$W_D = \sqrt{\frac{2\varepsilon_r\varepsilon_0V_{Bi}}{qN_D}}. \tag{2.8}$$

In reality, the strong dependence of the Schottky barrier height on only the metal work function and the semiconductor electron affinity, i.e. the Mott-Schottky relationship as described by equation 2.5, is often not confirmed by experiment. The discrepancy between experiment and Mott-Schottky relationship is attributed to the "Fermi-level pinning" phenomena. A vast number of different models to explain the observed experimental data can be found in literature. A detailed review of the different mechanisms and proposed models responsible for the pinning effect was given in 2001 by R. T. Tung.[93] The models introduce a dipole across the interface with concurrent voltage drop (V_{Int}) to describe the pinning mechanism i.e. the insensitivity of Φ_{SB} on Φ_M. The Schottky barrier height with the presence of an interface dipole is given by:[94]

$$\Phi_{SB} = \Phi_M - \chi + qV_{Int}\,. \tag{2.9}$$

Ascribed physical mechanisms responsible for the formation of the interface dipole are either interfacial defect states located within the band gap of the semiconductor or polarization of chemical bonds which form between the metal and the semiconductor.[95, 96] Surface defect states, metal induced gap states, defect states, or disorder induced gap states have been reported to be responsible for the formation of interfacial gap states. Figure 2-5 depicts the band diagram of a metal-semiconductor contact with interfacial defect states. Depending on the position of the charge neutrality level (CNL) relative to the Fermi-level at the interface, the net charge of the gap states is either negative or positive. The net gap state charge is negative for CNL lower than E_F while a positive net gap state charge can be seen if the position of the CNL within the band gap is higher than E_F. An electric dipole is formed between the charged gap states and image charges within the metal, separated by a dielectric layer of a thickness δ_{Gap}. The voltage drop (V_{Int}) across the interface depends on the net charge of the gap states (Q_{GS}), and the thickness (δ_{Gap}) and dielectric constant (ε_{Int}) of the interface region:

$$V_{Int} = \frac{\delta_{Gap} Q_{GS}}{\varepsilon_{Int} \varepsilon_0}. \tag{2.10}$$

As a consequence, the observed Schottky barrier heights rather depend on the position of the CNL at the interface than on the metal work function and the electron affinity of the semiconductor as it would be predicted by the Mott-Schottky relation (equation 2.5).

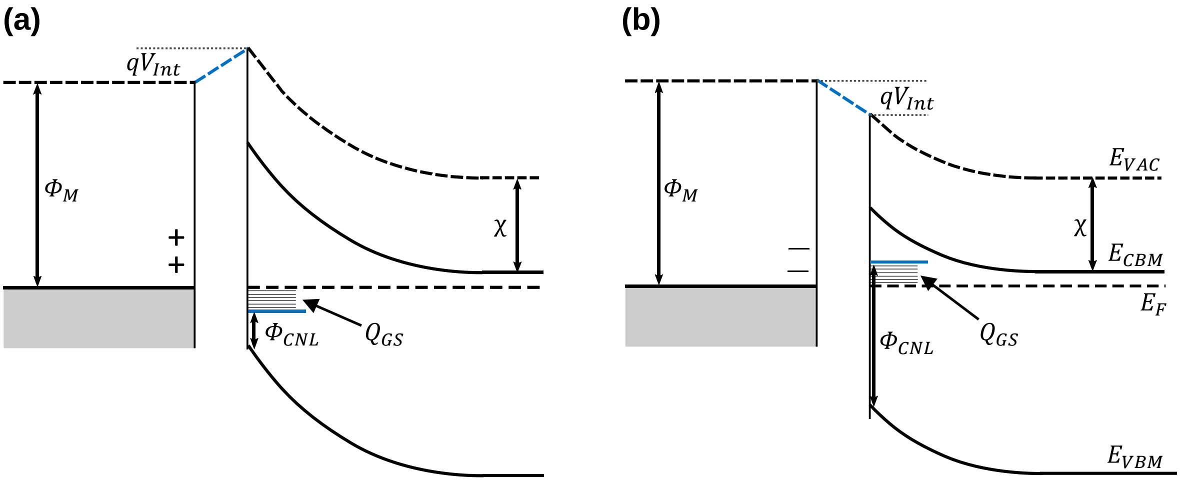

Figure 2-5: Energy band diagram of a metal-semiconductor contact with interfacial gap states located inside the bandgap of the semiconductor. (a) Charge neutrality level below the Fermi-level resulting in negative charged gap states and (b) charge neutrality level above the Fermi-level resulting in positively charged gap states (Redrawn after Tung[93]).

2.2.2. Schottky barrier characterization

Current transport across Schottky contacts can be facilitated by different mechanisms such as thermionic emission across the barrier, tunneling or field emission through the barrier as well as recombination in the space charge region and minority carrier injection. For Schottky contacts, the current transport is mainly dominated by majority charge carriers (electrons for n-type semiconductors).[92] The direction-independent current transport across laterally homogeneous barriers to moderately doped semiconductors in thermal equilibrium can be described by the thermionic emission of electrons across the potential barrier:[92]

$$J_{TE} = A^{*}T^{2}exp\left(-\frac{q\Phi_{SB}}{kT}\right), \tag{2.11}$$

with J_{TE} the current density, A^{*} the Richardson constant of the semiconductor, k the Boltzmann constant, and T the temperature. The rectifying properties arise from the different response of the barrier to forward or reverse biasing (see Figure 2-6).

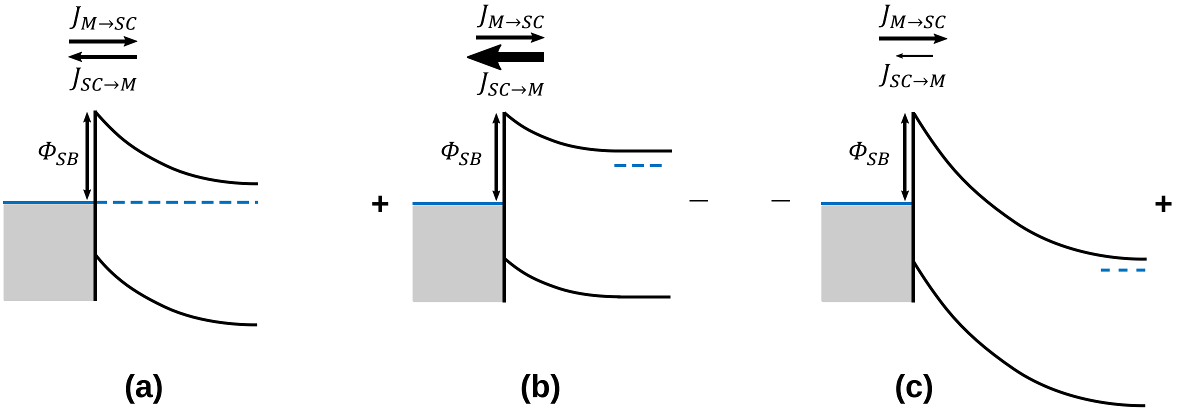

Figure 2-6: Current transport across a Schottky barrier by thermal emission process in thermal equilibrium (a), under forward bias (b), and under reverse bias (c).

Under forward biasing (Figure 2-6 (b)), the barrier for the electrons flowing from the semiconductor to the metal ($J_{SC\rightarrow M}$) is reduced to $\Phi_{SB} - qV$ with,

$$J_{SC\rightarrow M} = A^{*}T^{2}exp\left(-\frac{(\Phi_{SB} - qV)}{kT}\right). \tag{2.12}$$

The current density flowing from the metal to the semiconductor ($J_{M\rightarrow SC}$), however, is not dependent on the applied voltage and is given by equation 2.11. $J_{M\rightarrow SC}$ is in literature referred to as saturation current density J_0. The net current flow across the Schottky contact (J) is hence given by:

$$J = J_{SC\rightarrow M} - J_0 = J_0 \left[exp\left(\frac{qV}{kT}\right) - 1\right], \tag{2.13}$$

$$\text{with} \qquad J_0 = A^{*}T^{2}exp\left(-\frac{q\Phi_{SB}}{kT}\right). \tag{2.14}$$

For forward biased ideal Schottky contacts, the -1 term in equation 2.13 can be neglected if the applied voltage is sufficiently large ($V \gg kT/q$). Hence, the current density increases exponentially with increasing voltage. For the reverse biased ideal Schottky contact (Figure 2-6 (c)), $J_{SC\rightarrow M}$ becomes much smaller compared to $J_{M\rightarrow SC}$ and the reverse current density is given by J_0. Since lateral inhomogeneity, image force lowering and deviations from pure thermionic emission lead to deviations from the ideal current-voltage (*I-V*) response as described by equation 2.13, the empirical ideality factor η has been introduced:

$$J = J_0 \left[exp\left(\frac{qV}{\eta kT}\right) - 1\right]. \tag{2.15}$$

For an ideal Schottky contact, η should be unity, however, the analysis of real *I-V* characteristics often reveals $\eta > 1$. For semi-logarithmically plotted *I-V* characteristics, η can be determined from the slope of the linear region in the forward biased region:[97]

$$\eta = \frac{q}{kT}\left(\frac{dlnJ}{dV}\right)^{-1}. \tag{2.16}$$

By extrapolating the linear region to $V = 0$, the saturation current J_0 can be determined, from which the effective barrier height Φ_{SB} can be calculated by:[92]

$$\Phi_{SB} = \frac{kT}{q}\, ln\left(\frac{A^{*}T^{2}}{J_0}\right). \tag{2.17}$$

Figure 2-7 schematically depict the linear (a) and semi-logarithmic (b) *I-V* plot of a typical Schottky contact.

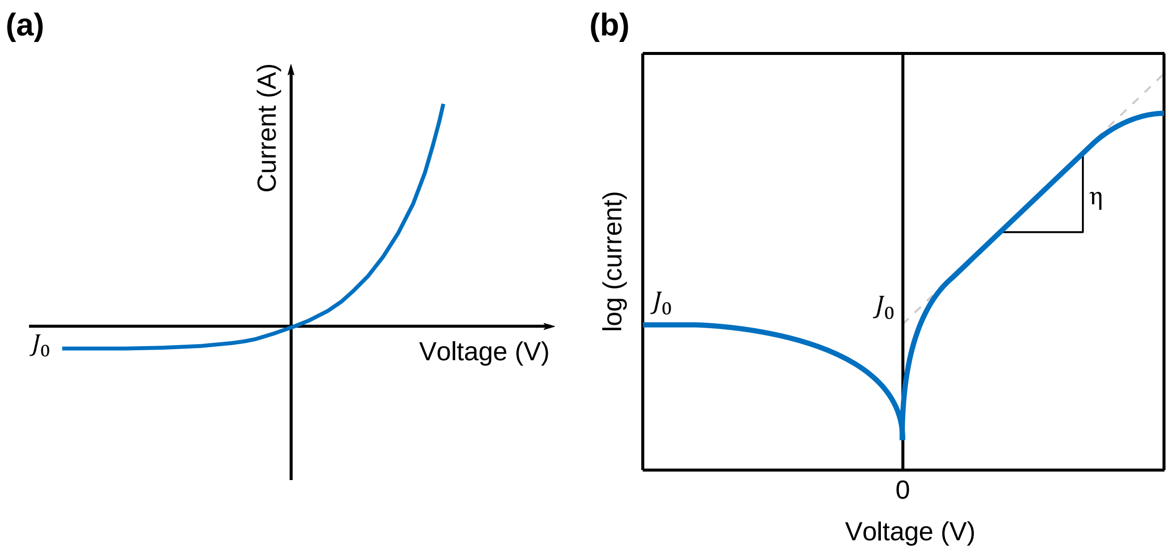

Figure 2-7: Schematic *I-V* characteristic of a typical Schottky contact. (a) Linear representation with reverse biasing (left) and forward biasing (right). (b) Semi-logarithmic representation from which J_0 and η can be determined.

2.2.3. Schottky barrier formation at metal – ZnO interfaces

Reliable fabrication of Schottky contacts to ZnO remains a challenge with a broad range of reported Schottky barrier heights for the same metal as summarized in a comprehensive review paper by Brillson and Lu[98]. Silver (Ag), Gold (Au), and Platinum (Pt) are widely used to create comparably high Schottky barriers to ZnO, but the classical Mott-Schottky relation as described by equation 2.5 barely holds for the prepared contacts. Values for Φ_{SB} to n-type ZnO for Ag, Au, and Pt contacts are reported to be in the range between 0.6 and 0.8 eV, regardless of their different work functions.[99-102] Extrinsic factors such as surface defect density, morphology, chemical composition, and chemical interaction between the metal and ZnO crystal play a crucial role for fabricating high quality Schottky contacts. For example, with increasing density of native defects at and below the surface of a ZnO crystal, the contacts can change from ohmic (high defect density) to strongly rectifying (low defect density).[103] Allen and Durbin[104] correlated the density of oxygen vacancies at the interface to the magnitude of the observed Fermi-level pinning at 0.7 eV below the conduction band. Hence, for the preparation of higher Schottky barriers, a low density of oxygen vacancies would be required. In addition, hydrocarbon and hydroxyl adsorbates at the surface were reported to strongly influence the quality of the Schottky contacts, emphasizing proper cleaning of the surface, for example by a remote oxygen plasma.[105-107] Further complexity arises, when a chemical interaction between the deposited metal and the ZnO semiconductor is accounted for. In II-VI semiconductors, such interactions can dominate the overall Schottky barrier formation process.[108] Chemical bonds formed between the metal and the semiconductor can be polarized and hence, change the obtained barrier heights by creating an interfacial dipole with concurrent voltage drop (V_{Int}).[94] Furthermore, the chemical reaction can induce defects, such as oxygen vacancies which strongly pin the Fermi-level.[104, 109, 110] The above mentioned mechanisms can have a strong lateral variation across a ZnO surface, making it difficult to prepare contacts with homogeneous barrier height, especially for large area contacts.[111] In addition, various studies report an influence of the polarity on the attainable Schottky barrier height. Most reports state higher Φ_{SB} for contacts fabricated on the Zn-polar surface than on the O-polar surface. The differences were attributed to different defect formation energies depending on Zn- or O-termination or the difference in band bending due to the existence of spontaneous polarization.[112, 113] In summary, despite the recent progress in understanding and optimizing the Schottky barrier formation process to ZnO together with the introduction of different theoretical models to quantitatively describe the formation process, experimental fabrication of homogeneous barriers with large area and low ideality factors remains a non-trivial task.

2.2.4. Ohmic contact formation in ZnO

To create an ohmic contact, the potential barrier height created at the metal – ZnO interface should be as low as possible. Therefore, the difference between the work function of the metal and the electron affinity of ZnO should be small. Due to the interaction between the metal and the semiconductor, this simple rule is often violated since Fermi-level pinning, as already described in chapter 2.2.1, leads to deviations from the Mott-Schottky equation. By the introduction of a highly doped layer at the surface of the semiconductor, the depletion width can be reduced, increasing the tunnel probability. Hence, basically an ohmic contact is formed. For ZnO, various metallization schemes are utilized to prepare ohmic contacts, as summarized in a review article by Brillson and Lu[98]. Titanium (Ti) and aluminum (Al) are widely employed to fabricate ohmic contacts to ZnO with low contact resistance.[114, 115] The work function of Ti (4.28 eV) and Al (4.33 eV) are in the range of the electron affinity of ZnO (~4.2 eV).[116, 117] In addition, Ti and Al are reactive metals which tend to react with oxygen when brought in contact with ZnO and thereby increase the oxygen vacancy concentration.[118] Therefore, an increase in defect concentration increases the subsurface donor doping level which in turn reduces the depletion width so that tunneling is facilitated. The high reactivity of Ti and Al makes it necessary to cover the contact with a thin layer of Au to prevent surface oxidization. Besides ohmic contacts based on elementary metals, annealed indium tin oxide (ITO) on ZnO has also been shown to exhibit ohmic characteristics, which is especially useful when transparent contacts are required for the desired application.[119]

2.2.5. Piezotronic modulation of Schottky contacts

As stated before, the piezotronic effect describes the modulation of electrostatic potential barriers by stress-induced piezoelectric polarization charges. The term “piezotronics” was coined, when a change in electrostatic potential barrier could be observed at a metal – ZnO nanowire contact.[1] In this chapter, the current understanding of the fundamental mechanism of the piezotronic influence on metal – ZnO Schottky contacts will be reviewed. Following the Poisson equation (equation 2.6), the potential distribution at a metal-semiconductor contact and with this, the Schottky barrier height is defined by the spatial electric charge distribution. Hence, it is straightforward to expect a direct influence of piezoelectric charges on the properties of a Schottky contact. Experimental evidence for the interaction between piezoelectric charge and the Schottky barrier height was already observed in the 1990s for GaN and GaAs.[10, 12] In 2011 Y. Zhang *et al.*[36] published an article on the fundamental theory of piezotronics to rationalize the increasing experimental work on ZnO-based piezotronic devices. The piezoelectric properties of the material are characterized by the polarization vector P_i as described by equation 2.2. Depending on the applied stress together with the piezoelectric stress coefficient of the material, positive or negative polarization charges will be generated on the Zn- or O- polar surfaces of a ZnO single crystal. In classical theory of piezoelectric materials, this polarization charge is considered as a surface charge. If a positive piezoelectric surface charge (Q_P) is induced at a Schottky contact, an increase in Q_M by the same amount will compensate for Q_P. Depending on the position of Q_M and Q_P, the electric field distribution in the vicinity of the contact will change and hence, a change in Schottky barrier height will be observed. Figure 2-8 depicts different situations which could rationalize the observed piezotronic modulation of metal-semiconductor contacts.

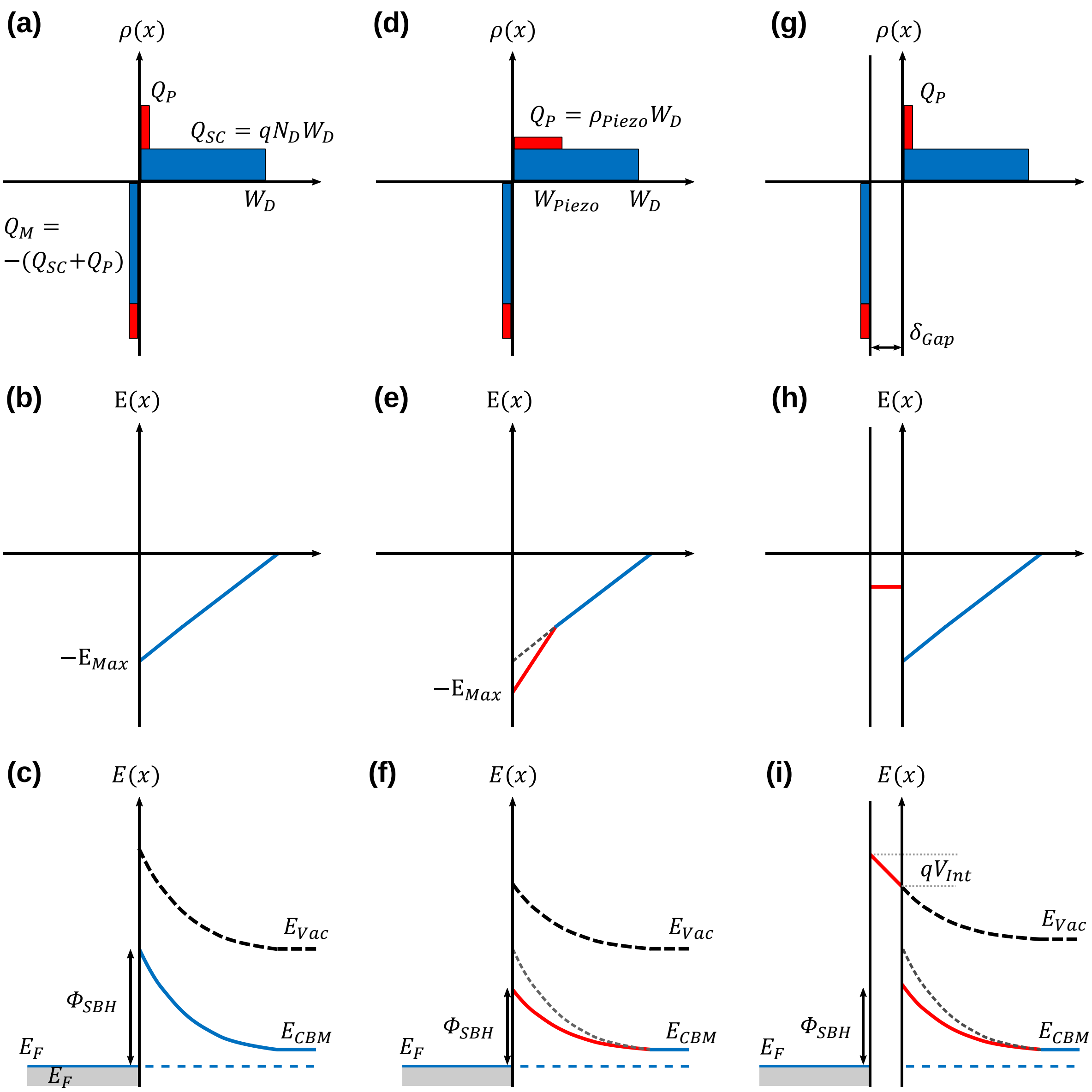

Figure 2-8: Schematic diagrams of the charge distribution ((a),(d),(g)), electric field distribution ((b),(e),(h)) and the resulting energy band diagram ((c), (f), (i)) of a Schottky contact with stress-induced positive polarization charges. In (a),(b), and (c) the piezoelectric charges are fully screened by free electrons in the metal, hence no piezotronic modulation of the Schottky contact can be observed. In (d), (e), and (f) the piezoelectric charges are assumed to be distributed within a finite width W_{Piezo}. In (g), (h), and (i) the piezoelectric charges are again assumed to be surface charges, but are separated by a finite distance, δ_{Gap}, from the screening charges within the metal.

In Figure 2-8 (a)-(c), the piezoelectric charges are assumed to be an infinitely thin surface charge density at the top layer of the piezoelectric semiconductor. The metal is assumed to be an ideal electrode with infinitely small screening length. Hence, the piezoelectric charge will be perfectly screened by free electrons in the metal. As a consequence, the electric field distribution and with this, the energy band diagram of the Schottky contact are not affected by stress-induced piezoelectric charges. Similar considerations are discussed within the field of thin film ferroelectrics, where the screening properties of metallic electrodes have profound influence on e.g. the magnitude of ferroelectric properties.[120, 121] Since perfectly screened piezoelectric charges do not rationalize the observed modulation of Schottky barriers, different models which could explain the change in electric field distribution have been introduced. They rely on a spatial separation of the piezoelectric charge and the metal screening charge.

Zhang *et al.*[36] assumed the nature of the piezoelectric charges not being an infinitely thin surface charge density but a spatial piezoelectric charge distribution within a defined width W_{Piezo}, as depicted in Figure 2-8 (d). In analogy with the classical theory of Schottky contact formation, the electric field distribution can be calculated by solving the 1-D Poisson equation (equation 2.6). The changed maximum electric field (E_{Max}) located at the interface can be calculated when the piezoelectric charge density (ρ_{Piezo}) is known:

$$|E_{Max}| = \frac{q}{\varepsilon_r \varepsilon_0} [N_D W_D + \rho_{Piezo} W_{Piezo}]. \tag{2.18}$$

From solving the Poisson equation for the charge distribution as depicted in Figure 2-8 (a), an increase in potential barrier height would be observed. However, Zhang *et al.* assumed a change in W_D by the generation of piezoelectric charges and considered the piezoelectric polarization as “perturbation” to the CBM. Subsequently, the resulting change in potential distribution and with this, the change in Schottky barrier height due to the generation of piezoelectric charge in their model is given by:

$$\Phi_{SB} = \Phi_{SB}^0 - \frac{q^2 \rho_{Piezo} W_{Piezo}^2}{2\varepsilon_r \varepsilon_0}. \tag{2.19}$$

The model as described by equation 2.19 rationalizes the experimentally observed decrease in potential barrier height for positive piezoelectric charges as well as the increase in potential barrier height for negative piezoelectric charges. It further prompts, that the magnitude of the barrier change does not only depend on the amount of stress-induced piezoelectric charge, but also on their spatial distribution (W_{Piezo}). Zhang *et al.*[36] assumed W_{Piezo} to be 0.25 nm for their calculations without giving further explanation of the physical origin for their assumption. Later, first principle simulations were applied, to shed light on the physical origin and width of the piezoelectric charge distribution.[122, 123] From density functional theory (DFT) calculations, the atomic arrangement and with this, the piezoelectric charge distribution width were determined. Liu *et al.*[122] determined $W_{Piezo} = 4.1$ Å for an Ag contact on the O-terminated surface of an ZnO single crystal and $W_{Piezo} = 3.7$ Å for an Ag contact on the Zn-terminated surface, respectively. In comparison to the depletion width (W_D), W_{Piezo} is rather small. Therefore, the expected changes in potential barrier height should also be small, especially for low values of applied mechanical stress. A similar concept was utilized to explain the barrier height adjustment by introducing a thin dopant layer (<10 nm) into the surface of the semiconductor prior to the Schottky barrier fabrication.[124] The introduction of different ions by low-energy ion implantation was used to reduce or increase the effective Schottky barrier height at a metal-semiconductor contact.[125, 126] However, the doping concentrations and the width of the ion distribution are much higher compared to typical values of piezoelectric polarization. Furthermore, the mechanism behind the interaction of surface doping and barrier height was attributed to enhanced quantum mechanical tunneling.[126]

Another model which may be highly applicable to describe the piezotronic modulation of Schottky contacts was proposed by Pintilie and Alexe[15]. The model was originally introduced to explain the interaction between ferroelectric polarization and Schottky contacts in metal-ferroelectric-metal heterostructures. In contrast to the model presented by Zhang, the polarization charges are not distributed over a finite distance (W_{Piezo}) but are present as a sheet of surface charge. The model assumes a finite distance (δ_{Gap}) between the polarization surface charge and the physical interface of the metal (Figure 2-8 (g)-(i)). The polarization cannot be completely screened by free charge carriers in the metal, hence the imperfect screening at the interface results in a potential drop across the junction.[127] The potential which forms across the interface can be calculated similar to equation 2.10 with the charge density of the gap states being replaced by the piezoelectric polarization charge (Q_P):

$$V_{Int} = \frac{\delta_{Gap} Q_P}{\varepsilon_{Int} \varepsilon_0}. \tag{2.20}$$

The change in potential barrier height is then given by:

$$\Phi_{SB} = \Phi_{SB}^0 - q \frac{\delta_{Gap} Q_P}{\varepsilon_{Int} \varepsilon_0}. \tag{2.21}$$

Similar to the model by Zhang[36], the magnitude of the barrier height change does not only depend on the amount of piezoelectric charge, but also on the interfacial distance between Q_P and Q_M. The thickness of the interfacial layer δ_{Gap} for metal-semiconductor contacts is reported to be in the range of a few Angstrom, originating from adsorbed gas molecules or from an oxide layer present between the semiconductor and metal electrode.[128, 129]

Internal charge compensation

In general, the piezotronic effect scales with the amount of stress-induced piezoelectric polarization charge. Primarily, this linearly depends on the applied mechanical stress and the piezoelectric coefficient of the material. However, materials for piezotronic applications are not ideal insulators but semiconductors with a finite number of free charge carriers. Therefore, internal compensation of piezoelectric polarization by free charge carriers needs to be considered as already pointed out by Alexe *et al.*[59]. In n-type ZnO, the free charge carriers are electrons and their density depends on the intrinsic and extrinsic defect concentration as described in chapter 2.1.3. Furthermore, the abundant excitation energy, mainly thermal energy and light energy, can modify the free charge carrier density and with this, the internal charge compensation. Hu *et al.*[130] studied the influence of temperature on the piezotronic performance of n-type ZnO nanowires with low, moderate, and high initial free charge carrier density. They found, that with decreasing temperature, the piezotronic effect could be enhanced for all types of nanowires. In addition, nanowires with low initial free charge carrier density featured the highest piezotronic effect. The enhanced piezotronic performance was attributed to a reduced compensation of the piezoelectric polarization by reducing the number of free charge carriers. Lu *et al.*[131] confirmed the proposed mechanism by artificially tuning the free charge carrier density under ultraviolet illumination. In the vicinity of a Schottky contact, the semiconductor is depleted from free charge carriers, which further reduces the internal compensation of the piezoelectric polarization as pointed out by Lu *et al.*.[132]

2.3. ZnO-based varistor interfaces

Similar to the Schottky barrier height at metal-ZnO junctions, stress-induced piezoelectric polarization can modify so called double Schottky barriers (DSB) at ZnO-ZnO interfaces. This mechanism was first discovered at the grain boundaries in polycrystalline varistor ceramics and experienced renewed interest when ZL Wang introduced the field of piezotronics.[1] A main objective of this work is to study the piezotronic potential of individual ZnO-ZnO varistor-like interfaces. Therefore, the formation mechanism of DSBs as well as their interaction with piezoelectric polarization will be reviewed in this chapter.

2.3.1. Double Schottky barrier formation

The distinctive feature of DSBs at ZnO-ZnO interfaces is their highly nonlinear *I-V* characteristic. Below a breakdown voltage (V_B), only a small leakage current flows, while the current increases by orders of magnitude when V_B is exceeded.[133, 134] The origin of the nonlinear *I-V* behavior is the existence of an electrostatic potential barrier, induced by a bound negative sheet charge at the ZnO-ZnO interface. The barrier formation process can be visualized by a thought experiment based on a bicrystal configuration as introduced by Pike.[135]

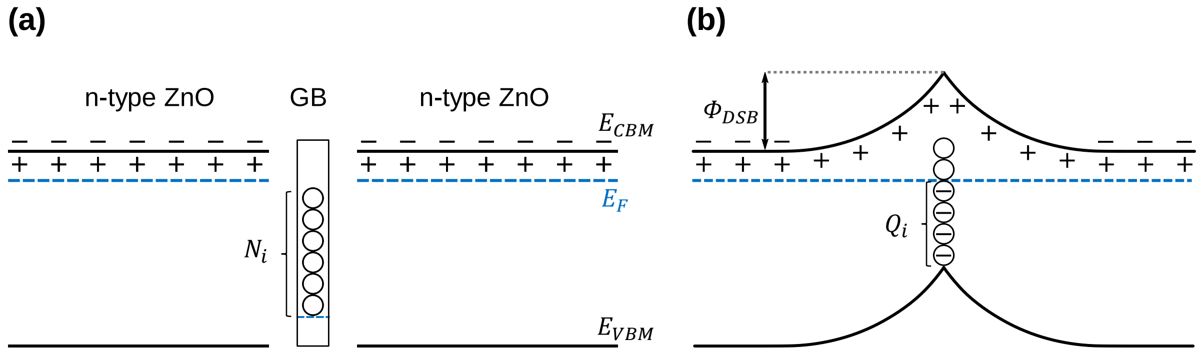

Figure 2-9: Schematic band diagram of the double Schottky barrier formation process at ZnO-ZnO interfaces. (a) Separated bicrystal configuration with defect state located within the grain boundary (GB) layer. (b) Fermi-level aligned bicrystal configuration with bound negative sheet charge captured in GB defect states, leading to symmetric band bending into adjacent ZnO crystals (redrawn after Pike[135]).

Figure 2-9 depicts the double Schottky barrier formation process at ZnO-ZnO interfaces. Two n-type ZnO crystals are separated by an interface or grain boundary (GB) material. The GB material is assumed to be of the same material as the ZnO crystals, hence it exhibits the same band gap. In contrast to the crystals, the GB material has defect states located within the band gap, which results in a different position of the Fermi-level (see Figure 2-9 (a)). In contact, free electrons from the n-type ZnO crystals will flow into the GB and occupy defect states until the Fermi-level is aligned across the interface. A negative sheet charge builds up at the interface (Q_i), generating an electric field and inducing band bending into the two adjacent ZnO crystals (see Figure 2-9 (b)). A detailed and widely accepted model for the potential barrier formation at charged grain boundaries in semiconductors can be found in several reports, e.g. by Blatter and Greuter.[136-138] The band bending around the charged interface and from this the barrier height (Φ_{DSB}) and depletion width (W_D) can be calculated from the 1-D Poisson equation (equation 2.6). Therefore, Φ_{DSB} sensitively depends on the details of the electronic charge distribution at and in close vicinity to the interface as shown in Figure 2-10 (a).

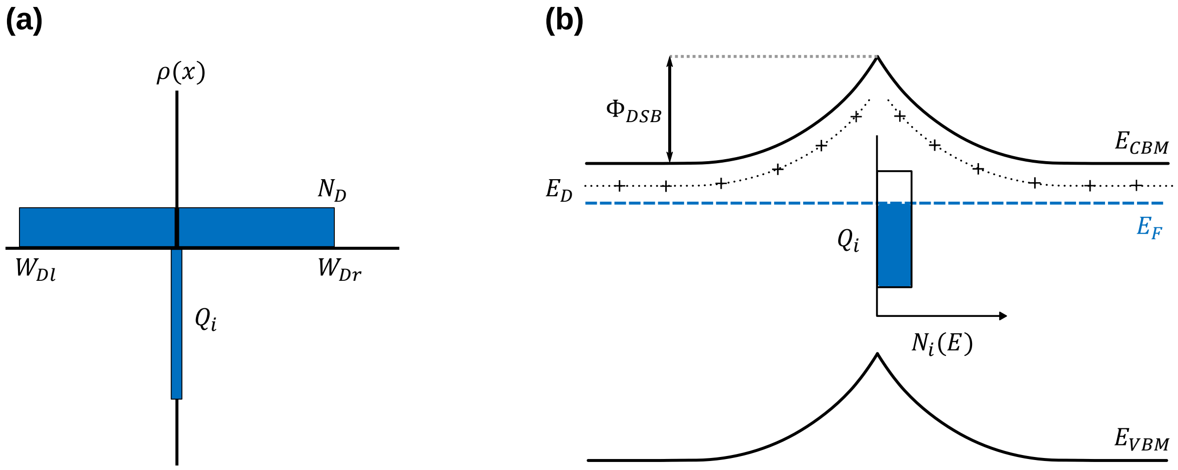

Figure 2-10: (a) Charge distribution of a symmetric double Schottky barrier at a ZnO-ZnO interface. (b) Energy band diagram for constant distribution of interfacial defect states and only one shallow donor defect state in the ZnO crystals (simplified from Blatter and Greuter[136]).

The charge distribution for only one bulk donor defect state and a constant distribution of interfacial defect states ($N_i(E)$) is given by:

$$\rho(x) = qN_D\,[\Theta(x - W_{Dl}) - \Theta(x + W_{Dr})] - Q_i\delta(x)\,, \tag{2.22}$$

with N_D the density of shallow donors in the bulk, W_{Dl} and W_{Dr} the depletion width in the left and right crystal, Θ the Heaviside step function, and δ the Dirac delta function. The resulting potential barrier height is then given by:

$$\Phi_{DSB} = \frac{(Q_i)^2}{8q\varepsilon_r\varepsilon_0 N_D}. \tag{2.23}$$

The potential barrier height exponentially depends on the negative sheet charge accumulated within the interfacial defect states. As origin of the defect states within the band gap and with this the varistor action of the interface, dangling bonds as well as doping with large-sized ions were discussed. In the following section, a short review on the current understanding of the microscopic origin of the acceptor-like interface states is given.

Microscopic origin of interfacial defect states

The fast development of ZnO-based varistor ceramics since its discovery in the 1970s yielded commercially successful products. A large extent of this development was driven by heuristic methods with emphasis on optimizing compositions and manufacturing processes. Still, within decade long research in the field, many reports tried to identify the defect formation mechanism responsible for the varistor behavior. Starting from Matsuoka in 1971, bismuth and oxygen are mainly discussed to have a key role in generating varistor behavior by segregating to the GBs in ZnO.[46, 139, 140] Deep level transient spectroscopy and *I-V* deconvolution techniques were utilized to shed light on the identity and distribution of interfacial defect states in polycrystalline varistor ceramics.[141-143] Up to three independent defect state levels were found within the bandgap at the interface, from which some are only partly filled. It was further shown, that by varying the doping concentration or heat treatment, their concentration could be changed, but their energetic position remained unchanged.[143] In addition, by moving from Bi to praseodymium (Pr) doping, defect states with the same energy-position are observed. Therefore, it is seen more likely, that large-sized ions like Bi and Pr do not directly form acceptor-like defect states but are involved in their formation. A proposed mechanism is, that Bi and Pr promote the formation of acceptor-like native defects at the GB, namely V_{Zn} and O_i.[144 145] First-principle calculations by Carlsson *et al.* further suggest, that a defect complex (Bi_{Zn} - V_{Zn} - O_i) is formed at the interface, especially in O-rich condition and that the complex induces acceptor states within the band gap.[145, 146]

Despite the fact, that GB misorientation and thereby dangling bonds alone are found not to be responsible for acceptor state formation, in individual Pr doped ZnO interfaces, an increase in *I-V* nonlinearity was observed with decreasing GB coherency.[147-149] The increase in nonlinearity was attributed to a higher segregation of the large-sized ion Pr to the incoherent GB and hence a higher interfacial defect state density. Also in Bi doped ZnO interfaces, an influence of the GB structure on the electrical properties is known.[150] Furthermore, an influence of the GB polarity on the attainable barrier height was demonstrated. High barriers were predominantly observed at interfaces with at least one O-polar plane of an adjacent ZnO grain contributing to the GB formation.[151, 152]

The complex interaction between extrinsic and intrinsic defect states can also be accounted for to describe the high sensitivity of the barrier formation process on the details of the temperature treatment. Temperature treatment during manufacturing (sintering) and during a possible subsequent annealing step influences the potential barrier height. ZnO and Bi_2O_3 form an eutectic phase at 740 °C, therefore ZnO-Bi_2O_3-based varistors are typically prepared by liquid phase sintering at around 1100 °C for several hours.[153] Besides the modification of the microstructure, e.g. grain size, a prolonged sintering time as well as too high sintering temperatures can reduce the Bi concentration at ZnO interfaces due to the volatility of Bi and hence reduce the desired varistor behavior.[154] Furthermore, the segregation behavior and phase type of Bi at the GB depends on the cooling rate.[155] The concentration and distribution of native defects, which are known to have a profound influence on the potential barrier height can be influenced by temperature treatments.[156] Especially the present atmosphere during the heat treatment is known to play a major role in the barrier formation process. Oxidizing atmospheres have been shown to be beneficial for varistor behavior, while reducing atmospheres show opposite effects. This was attributed to oxygen incorporation into the GBs of the ZnO ceramic.[157, 158]

2.3.2. Electrical transport across double Schottky barriers

The formation of a double Schottky barrier at the grain boundaries of varistor ceramics results in a typical nonlinear current voltage characteristic, which will be described in the first part of this section. A detailed theoretical model of the charge transport across doped semiconductor grain boundaries was given by Blatter and Greuter within two publications in 1986.[136, 159] The most relevant aspects therefrom, regarding this work, will be summarized in the second part of this section.

Typical *I-V* characteristic of a varistor-type double Schottky barrier

Figure 2-11 depicts the typical *I-V* characteristic of a ZnO-based varistor ceramic. Due to the symmetry of the double Schottky barrier, the *I-V* characteristic of a varistor is independent on the polarity of the applied voltage. Below a characteristic “switch” or “breakdown” voltage (V_B), the current is determined by thermionic emission of charge carriers across the potential barrier and follows an ohmic behavior (*leakage current regime*). When V_B is reached, a highly nonlinear increase in current can be observed with only a small increase in electric field. This regime is often described by the empiric power law:[46, 160]

$$I \propto V^{\alpha}, \tag{2.24}$$

where α is the coefficient of nonlinearity. The α value can be calculated by:

$$\alpha = \frac{d(\ln I)}{d(lnV)}. \tag{2.25}$$

High α values are desirable for the application of varistors in the field of surge protection. Most commercial varistor ceramics exhibit α values in the range between 30 and 80.[134] The breakdown voltage for individual grain boundaries, which may be determined as the point where α exhibits its maximum, is reported to be in the range of 3-3.5 V.[160] But slightly smaller or large values were also reported for different kinds of grain boundaries.[161, 162] Last, in the high current regime, the *I*-*V* characteristic again follows an ohmic behavior, where the resistivity is mainly controlled by the resistivity of the ZnO grains.

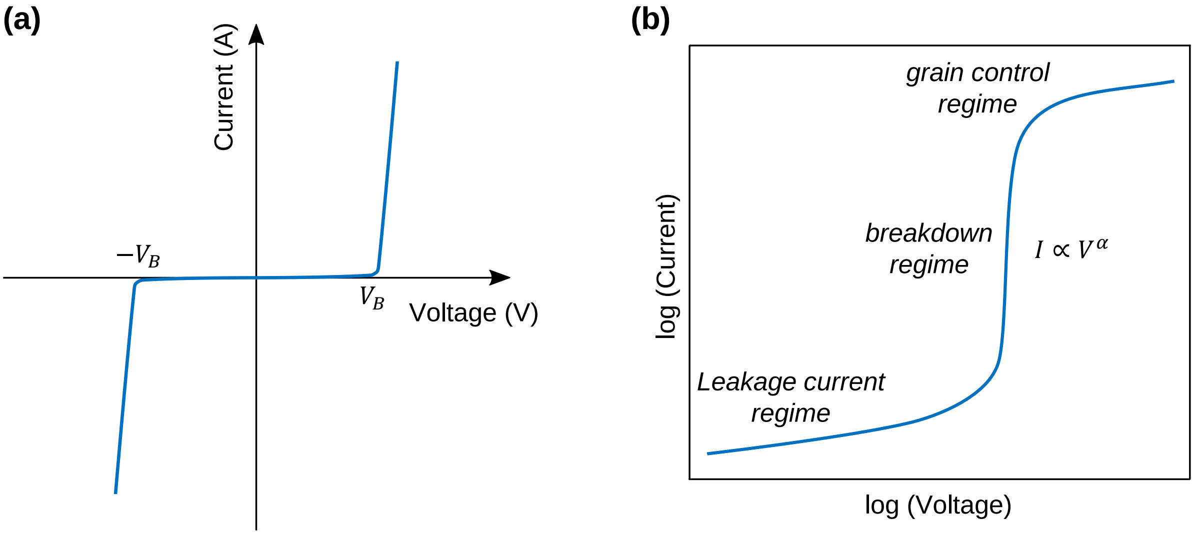

Figure 2-11: Typical current voltage characteristic of a double Schottky barrier. (a) Linear representation, demonstrating the polarity-independent breakdown behavior. (b) Double logarithmic *I*-*V* response visualizing the three distinct regimes.

Theoretical description of charge carrier transport

The electrical transport across DSBs can in general be described by thermionic emission of majority charge carriers (electrons) across the potential barrier (Φ_{DSB}) as described by equation 2.11:

$$J_{TE} = A^{*}T^{2}\exp\left(\frac{-(\Phi_{DSB} + \epsilon_{\xi})}{kT}\right), \tag{2.26}$$

with ϵ_ξ being the position of the Fermi-level with respect to the CBM. Without the application of an external voltage, J_{TE} flowing from the left grain to the right grain equals J_{TE} flowing in the opposite direction. When a voltage is applied, Φ_{DSB}, seen by an electron flowing from the negatively biased grain towards the positively biased grain, is increased by qV. Therefore, the total current density across the barrier is given by:

$$J(V) = A^{*}T^{2}\exp\left(\frac{-(\Phi_{DSB} + \epsilon_\xi)}{kT}\right) \cdot (1 - \exp\left(\frac{-qV}{kT}\right)). \tag{2.27}$$

In addition, the potential barrier height is a function of the applied voltage. The voltage-dependent potential barrier height ($\Phi_{DSB}(V)$) under the assumption of only one bulk donor state is given by:

$$\Phi_{DSB}(V) = \frac{(Q_i^2 - 2qN_D V \varepsilon_r \varepsilon_0)^2}{8qN_D \varepsilon_r \varepsilon_0 Q_i^2}. \tag{2.28}$$

This description alone cannot rationalize the experimentally observed *I-V* characteristic of varistor grain boundaries. The extremely high nonlinear behavior arises from a so called “Fermi-level pinning” effect at low voltages within the leakage current regime. The interface charge Q_i is not independent from the potential barrier height and hence, from the applied voltage. The captured charge Q_i is determined by the density of states (DOS) $N_i(E)$ and the position of the Fermi-level at the interface (ξ_i):

$$Q_i = q\int_{\xi_i^n}^{\infty} dE\ N_i(E)\, f(E), \tag{2.29}$$

with $f(E)$ being the Fermi-level distribution and ξ_i^n the Fermi-level of the neutral interface. The Fermi-level distribution $f(E)$ is given by:

$$f(E) = \frac{1}{1 + e^{(E-\xi_i)/kT}}. \tag{2.30}$$

The position of the interfacial defect states $N_i(E)$ with respect to the valence band maximum is fixed. When a voltage is applied, the barrier height is changed according to equation 2.28 and $N_i(E)$ shifts relatively to ξ_i, as it can be seen from equations 2.29 and 2.30. If empty defect states exist above the Fermi-level, the shift of $N_i(E)$ with decreasing barrier will lead to additional charge captured at the interface. Hence, Q_i is a function of $\Phi_{DSB}(V)$ and a lowering in Φ_{DSB} can be partially compensated by an increase in Q_i. This mechanism is referred to as Fermi-level pinning. Only when $N_i(E)$ is completely filled, a further increase in voltage will then lead to a rapid decay of Φ_{DSB}.

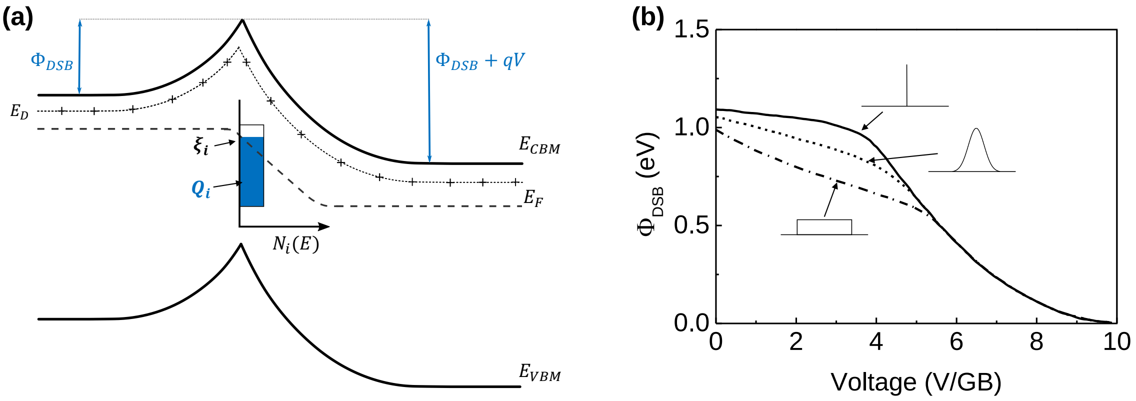

Figure 2-12: (a) Energy band diagram of a double Schottky barrier under the application of an external voltage. One single bulk donor state and a rectangular distribution of $N_i(E)$ is considered. The amount of Q_i depends on the relative position of ξ_i and $N_i(E)$, which is fixed to E_{VBM}. (b) Potential barrier height as a function of applied electric field (redrawn after Blatter and Greuter[136]).

The efficiency of the pinning mechanism strongly depends on the amount of empty defect states as well as on their distribution. Blatter and Greuter have calculated the voltage-dependent potential barrier height for different distributions of $N_i(E)$, namely a single interface level, a Gaussian distribution as well as a rectangular shape (Figure 2-12 (b)).[136] Regardless of the different DOS, a rapid decay of Φ_{DSB} can be observed when $N_i(E)$ is completely filled. The most effective pinning is observed for one individual energy level of $N_i(E)$ while a rectangular distribution features the weakest pinning. In reality, additional donor-like states in the bulk and a more complex $N_i(E)$ would be expected to have additional influence on the real interface behavior. Still, the simplified model is already capable of providing a profound explanation for the transport properties of varistor grain boundaries for the leakage current regime at low voltages. Furthermore, it can explain the observed temperature dependence of the leakage current.

To rationalize the extremely high nonlinearities observed when the breakdown voltage (V_B) is reached, an additional mechanism for a more rapid barrier lowering needs to be considered. Mahan *et al.* were the first to propose the involvement of minority charge carriers (holes) to explain the large nonlinearities observed at high electric fields.[160] Besides a different transport process involved, Pike seized the idea of hole generation by impact ionization in a subsequent model.[163] Under the application of a large electric field, electrons are accelerated into the positively biased grain, where they can generate holes by impact ionization if they acquire high enough energy. This process is referred to as "*impact ionization*". Holes created by impact ionization diffuse back to the interface where they can compensate the negative interface charge and by this lower the potential barrier height. According to equation 2.27, a decrease in potential barrier height will exponentially increase the current. Hence, the hole generation increases and an "avalanche" process starts, which can result in extremely high nonlinearities. Evidence for the hole contribution to the breakdown behavior of varistor ceramics was given by electroluminescence measurements which are a direct proof of electron- hole recombination.[164]

2.3.3. Piezotronic modulation of double Schottky barriers

As piezoelectric polarization charges can modulate the electronic band structure of metal-ZnO Schottky contacts, a similar mechanism can be expected for varistor-like DSBs. This chapter will introduce the current understanding of the piezotronic modulation of DSBs in ZnO-based varistor systems.

The first observation of a stress-dependent modulation of conductivity in ZnO-based varistor ceramics was given by Wong and Bundy in 1976.[23] The application of a uniaxial mechanical stress revealed an increase in leakage current by orders of magnitude and a profound decrease in α values. The change in electrical properties was shown to be partially reversible. The observations by Wong and Bundy were confirmed by various authors.[26, 165, 166] Gupta *et al.*[165] attributed the change in electrical conductivity to a stress-induced change in potential barrier height. Emtage[24] and Doshchanov[167] first discussed a possible interaction between piezoelectric polarization charges and the charge distribution at the GBs of piezoelectric semiconductors as origin of the barrier height modification. Verghese and Clarke[25] summarized the interaction of piezoelectric polarization charge and potential barrier height within their article on the piezoelectric contributions to the electrical behavior of ZnO varistors. They assumed, that the interfacial sheet charge density Q_i is modified by piezoelectric polarization charge Q_P upon the application of a mechanical stress. By solving the Poisson equation under the consideration of Q_P, equation 2.23 is modified to:

$$\Phi_{DSB} = \frac{(Q_i + Q_p)^2}{8q\varepsilon_r\varepsilon_0 N_D}. \tag{2.31}$$

Under the assumption of an infinitesimally thin GB, the piezoelectric polarization charge is composed of the contributions from the left and right grain:

$$Q_P = \boldsymbol{n}(\sigma^l_{jk} d^l_{ijk} - \sigma^r_{jk} d^r_{ijk}), \tag{2.32}$$

with $\boldsymbol{n}$ being the grain boundary normal vector. Depending on the relative orientation of the two adjacent grains, a net positive or a net negative Q_P is generated under e.g. a uniaxial compressive stress as depicted in Figure 2-13. The generation of a positive Q_P will compensate the negative Q_i and therefore reduce the barrier height, while a negative Q_P will increase the overall Q_i and hence increase the potential barrier height. At least qualitatively, this mechanism was experimentally proven by Raidl *et al.*[27] in measuring individual GBs of low-voltage multilayer varistors.

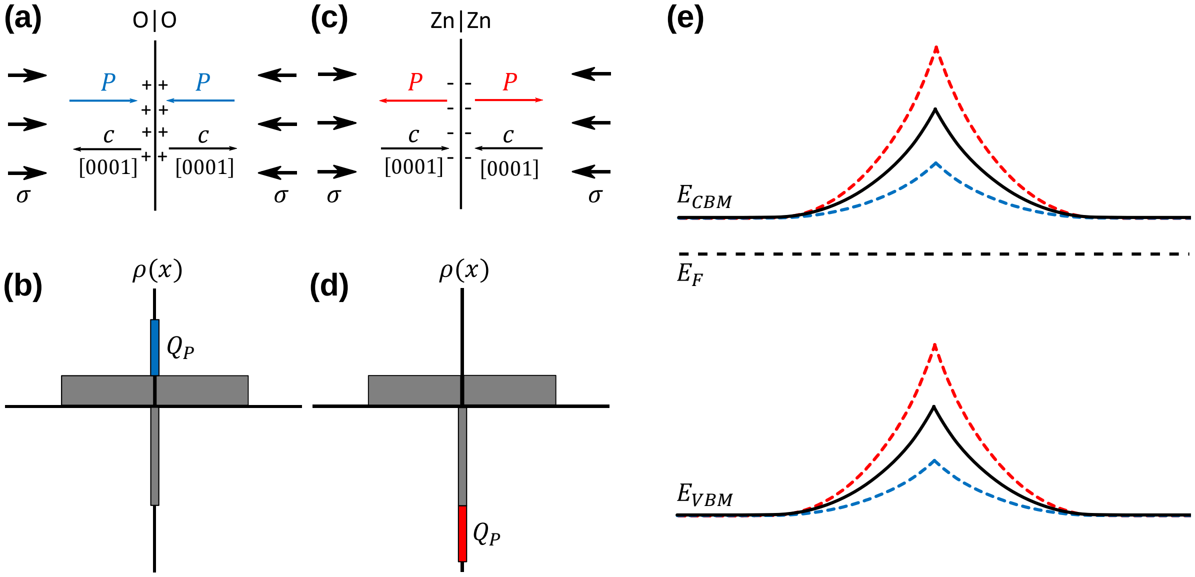

Figure 2-13: Charge distribution under the application of uniaxial compressive stress perpendicular to an O|O- and Zn|Zn-interface. For the O|O-interface, positive piezoelectric charges are generated (a), while for the Zn|Zn-interface, negative piezoelectric charges are generated (c). The corresponding charge distributions are depicted within (b) and (d). The simplified potential barrier height under the influence of piezoelectric polarization charges after the model of Verghese and Clarke[25] is shown in (e), with a decreasing potential barrier for positive piezoelectric charges and an increasing potential barrier for negative piezoelectric charges.

Baraki *et al.*[168] extended the simplified model from Verghese and Clarke by considering the voltage dependence as well as a possible Fermi-level pinning effect as described by Blatter and Greuter. By considering a piezoelectric contribution, they extended equation 2.28 to:

$$\Phi_{DSB}(V) = \frac{((Q_i + Q_P)^2 - 2qN_D V \varepsilon_r \varepsilon_0)^2}{8qN_D \varepsilon_r \varepsilon_0 (Q_i + Q_P)^2}. \tag{2.33}$$

From stress and temperature-dependent *I*-*V* measurements on polycrystalline varistor ceramics, they concluded an equivalent influence of voltage and mechanical stress on Φ_{DSB}. For low electrical fields, they observed an insensitivity of Φ_{DSB} to slowly increasing mechanical load. Only when the mechanical stress exceeded a specific value, the generated Q_P directly leads to a change in Φ_{DSB}. The necessary mechanical stress to modify Φ_{DSB} could be decreased by increasing a simultaneously applied electric field. Therefore, they suggested, that empty defect states above the Fermi-level can partially compensate an initial reduction in Φ_{DSB} for the generation of positive piezoelectric charges. This mechanism is analogous to the Fermi-level pinning effect described within the previous chapter. By assuming a DOS of a Gaussian shape, they were able to fit the experimental observations with model calculations. Figure 2-14 illustrates the interaction of the DOS and stress-induced Q_P.

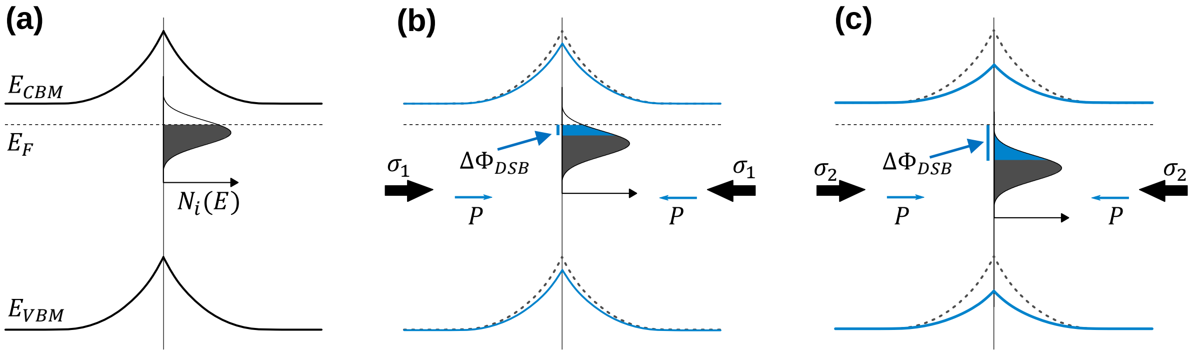

Figure 2-14: Schematic band diagram of a DSB and its modification with piezoelectric polarization after the model of Baraki *et al.*[168]. (a) Initial potential barrier without the application of mechanical stress. The interfacial defect state density ($N_i(E)$) is assumed to have a Gaussian shape and exhibits empty defect states above the Fermi-level (E_F). (b) Under the application of uniaxial compressive stress (σ_1), positive piezoelectric charges tend to reduce the potential barrier height. The reduction of Φ_{DSB} moves $N_i(E)$ relative to E_F, therby empty defect states are filled which partially compensates the reduction of Φ_{DSB}. (c) For high mechanical stresses (σ_2), $N_i(E)$ is completely filled and a further increase in stress results in a direct reduction of Φ_{DSB}.

Most experimental studies on the modulation of Φ_{DSB} by piezoelectric charges were performed on polycrystalline samples where percolating effect are known to play a major role. In addition, it was shown, that mechanical stress has a profound influence on percolation on polycrystalline varistor ceramics.[25, 168] Hence, percolating effects and the influence of stress in percolation in polycrystalline varistor ceramics will be shortly summarized in the following section.

2.3.4. Percolating effects in polycrystalline material

Polycrystalline varistor ceramics can be seen as a 3-D network of grains and grain boundaries where the grains are electrically conductive and the grain boundaries feature electrostatic potential barriers. It was found, that the overall varistor response of the 3-D network to the application of an electric field differs from the response of individual boundaries.[169] The mean breakdown voltage as well as the coefficient of nonlinearity in the ceramic are lower than that of an isolated grain. Emtage[169] attributed the formation of percolating pathways due to variations in grain size to the observed reduction in breakdown voltage for polycrystalline ceramics. Current localization has been visualized by electroluminescence measurements and thermal imaging.[134, 170, 171] It was furthermore shown, that the existence of different types of grain boundaries can reduce the mean breakdown voltage and coefficient of nonlinearity.[172-174] Variations in grain boundary properties were proven to exist by various microcontact studies.[161, 162, 175, 176] Nan and Clarke[177] nicely modeled the influence of increasing variations in grain size and grain boundary potential barrier height on the electrical properties of polycrystalline varistors. With an increasing standard deviation of a Gaussian distribution in potential barrier heights, a decrease in nonlinearity and breakdown voltage as well as an increase in leakage current was observed.

The stochastic model was later utilized to describe the influence of mechanical stress on the electrical properties of a polycrystalline varistor ceramic.[25] Due to the random relative grain orientation in a polycrystal, the stress-induced piezoelectric polarization charge, which is given by the total projection of the polarization vectors in the two adjacent grains, will vary from grain boundary to grain boundary. Hence, the change in potential barrier height will also vary among different grain boundaries. Verghese and Clarke could show theoretically, that, due to the piezoelectric modification, the standard deviation in potential barrier height distribution increases with increasing mechanical stress. An increasing standard deviation of barrier heights causes percolation, leading to a decrease in nonlinearity and breakdown voltage as well as an increase in leakage current as it was observed in experimental studies.[23, 165, 166] Further evidence for an interplay between mechanical stress and percolation in mechanically stressed varistor ceramics was given by stress- and temperature-dependent conductivity measurements as conducted by Baraki *et al.*.[168] Even in stress-free condition, they observed a nonlinear trend with variation in temperature from which it was concluded, that at least two processes contribute to the overall conductivity through the polycrystalline sample. Similar nonlinearities were already observed before.[178] The assumption of a small percolating pathway with lower activation energy (~ 0.4 eV) within the majority of the material with higher activation energy (~1 eV) could rationalize the observed temperature dependence.[168] Under the application of a uniaxial compressive stress, the observed nonlinearity increased, indicating, that the percolating effects are enhanced. This demonstrates, that a few pathways show superior sensitivity to mechanical stress in comparison to the majority of the material. With a pure increase in standard deviation of potential barrier height distribution as supposed by Verghese and Clarke[25], the experimental results could not be fitted, since the highly conductive pathway was underrepresented. Raidl *et al.*[171] studied the volume efficiency of a polycrystalline varistor ceramic under the application of mechanical stress. With increasing stress, they observed a decrease in volume efficiency, i.e. higher degree of localization, in the pre-breakdown regime. On the other hand, in the vicinity of the breakdown voltage, a higher volume fraction took part in current transport.

2.3.5. Previous bicrystal studies

A major part of this work is to investigate the potential of individual varistor-like ZnO-ZnO interfaces for piezotronic applications. One promising concept to gain control over the chemical and structural properties of single interfaces is the preparation of bicrystals. Hence, in this chapter previous studies on the fabrication of varistor-like bicrystal interfaces are reviewed.

In 1980 Schwing and Hoffmann[179] reported on the fabrication of a macroscopic varistor model based on ZnO bicrystals with an intermediate layer of metal oxides. They inserted a thin foil composed of a mixture of Bi_2O_3, MnO_2, and Co_3O_4 as well as a ceramic binder, in between two ZnO single crystals before a subsequent sintering step under slight uniaxial compression. *I-V* measurements revealed a breakdown voltage of 3.5 V and a coefficient of nonlinearity in the range between 8 and 11, demonstrating the possibility to artificially mimic grain boundaries of polycrystalline varistor ceramics. Probably due to the large thickness of the inserted foil (40 µm) the fabricated bicrystals had a remnant intermediate layer of about 15-20 µm, which is in significant difference to typical grain boundaries in polycrystalline varistor ceramics. In a later publication, they were able to increase the coefficient of nonlinearity while decreasing the thickness of the remnant intermediate layer.[180] Also Cheng *et al.*[181-183] observed electrical properties similar to that of typical varistor ceramics despite the presence of a large remnant intermediate layer.

Ikuhara *et* al. tried to apply detailed transmission electron microscopy (TEM) studies to shed light on the microscopic origin of defect state formation at varistor boundaries, as summarized in a comprehensive review article.[149] Therefore, well defined interfaces without the presence of an intermediate dopant layer were inevitable. By replacing the thick foil, as utilized by Schwing and Hoffmann[179], with a thin metallic layer (~ 5 nm) to incorporate the dopants prior to diffusion bonding, a clean interface could be achieved. With the deposition of only a thin dopant layer, mainly small values for the coefficients of nonlinearity could be realized.

Lee and Maier[151] studied the influence of inversion boundary polarity ((O)|(O) or (Zn)|(Zn)) on the electrical properties of ZnO-ZnO interfaces. By sputter deposition of a metallic dopant layer (∼ 50 nm) on the surfaces of ZnO single crystals before a diffusion bonding step, they were able to prepare interfaces with precise control over the relative grain orientation. Interfaces with (O)|(O) polarity featured significantly higher varistor action compared to (Zn)|(Zn) boundaries. Peak values for the coefficient of nonlinearity of around 40 were achieved, which is comparable to values observed in polycrystalline varistor ceramics. Similar values could be reported for interfaces where Bi was replaced by Pr doping.[184]

3. Concept and aim of this work

The piezotronic effect, hence, the coupling of piezoelectric and semiconducting properties to tune the charge transport across electrostatic potential barriers is proposed as mechanism for the development of innovative multifunctional electronic devices like strain sensors, optical sensors, strain triggered transistors or energy harvesters.[2] A large number of publications proposes piezotronic devices based on metal-ZnO nanowire Schottky contacts, nicely demonstrating the capability of the piezotronic effect for the development of innovative electronic devices. However, the application of ZnO nanostructures in most studies goes along with experimental difficulties leading to open questions regarding the physical interpretation of experimental data on the mechanically tuned conductivity across Schottky contacts. The experimental drawbacks of the nanostructure studies are listed below:

1. Schottky contacts are often applied on both polar surfaces of the nanostructures.[185]
2. Schottky contacts ore often not only applied on the polar surfaces but also on the non-polar sides of the nanostructures.[33]
3. Bending of the nanostructures under the application of a high mechanical load leads to a complex distribution of the piezoelectric potential.[186]

In the first part of this work, the above-mentioned experimental difficulties are avoided by utilizing individual Schottky contacts on either the Zn- or O-terminated surface of a bulk ZnO single crystal, while on the corresponding opposite side ohmic back contacts are fabricated. With this experimental approach, the overall electrical properties are dominated by the individual Schottky contacts. Furthermore, a homogeneous stress distribution within the bulk ZnO single crystal allows to determine the precise amount of piezoelectric polarization charges, which interact with the Schottky contact. Therefore, the experimental approach enables a direct verification of the experimental data by theoretical models. The obtained results are discussed in the first part of this work within chapter 5.1.

A second relevant question which shall be addressed within this work was raised by Alexe *et al.*[59] in 2008. The typically high intrinsic n-type conductivity of ZnO is believed to screen the stress-induced piezoelectric potential. Especially for piezotronic energy harvesters, the screening effect would significantly reduce the device performance. One mechanism to retain the piezoelectric potential, despite of the high intrinsic conductivity of ZnO, is the formation of a highly resistive space charge region in the vicinity of a Schottky contact.[187] To shed light on the influence of a highly resistive space charge layer on the attainable piezoelectric potential in ZnO as well as on the screening mechanism in general, direct piezoelectric measurements are performed on bulk ZnO single crystals with two ohmic contacts or one Schottky contact, respectively. In addition, the piezoelectric measurements are conducted over a wide temperature range to gradually tune the free charge carrier density also for the crystal without resistive space charge region. By varying the loading frequency, further information on the time dependent screening mechanisms can be drawn. The results will be discussed in chapter 5.2 of this work.

In the third part of this work, individual varistor-type ZnO-ZnO interfaces shall be prepared and tested for their performance in piezotronic applications. Similar to the interaction between piezoelectric polarization charges and the electrostatic potential at metal-ZnO Schottky contacts, potential barriers at grain boundaries of polycrystalline varistor ceramics can be tuned by stress-induced piezoelectric charges.[168] However, due to the random relative grain orientation within a polycrystalline varistor ceramic, percolating pathways determine the stress sensitivity of piezotronic devices based on varistor ceramics which prevents device design with precise control over electrical and structural parameter. The fabrication of ZnO bicrystals by epitaxial solid-state transformation with precise control over the structural (polarization vector orientation) and chemical (potential barrier formation) parameter, allows to systematically study the interaction between positive or negative piezoelectric charges and the potential barrier height at varistor-type ZnO-ZnO interfaces. The investigations on the piezotronic modulation of potential barriers at individual ZnO bicrystal interfaces will be presented in chapter 5.3.

In the final part of this work, single crystal – polycrystal structures with varying amount of remaining polycrystalline material in between two well oriented single crystals are prepared and tested for their piezotronic performance. Like the preparation of individual ZnO bicrystal interfaces, single crystal – polycrystal structures are prepared by epitaxial solid-state transformation of a polycrystalline layer in between two ZnO single crystals. Different amount of remaining polycrystalline material in between the single crystals can be achieved by interrupting the epitaxial solid-state transformation at various stages of the required high temperature treatment. Therefore, the studies on structures with interrupted epitaxial solid-state transformation allow to reveal the influence of the high temperature treatment on the stress sensitivity of piezotronic ZnO bicrystals. Furthermore, single crystal – polycrystal structures close the gap between piezotronic devices based on polycrystalline varistor ceramics and piezotronic devices based on individual ZnO-ZnO interfaces. The results on the piezotronic modulation of single crystal – polycrystal structures will be discussed in chapter 5.4.

Simultaneous investigations of the above-mentioned approaches including studies on metal-ZnO Schottky contacts as well as individual ZnO-ZnO interfaces allow a direct comparison of the two concepts with respect to their performance in piezotronic applications. Advantages and disadvantages of the different concepts should be identified, guiding and possibly broadening future research activities in the field of piezotronics.

4. Experimental

4.1. Preparation of metal-ZnO contacts

The investigation on the piezotronic modulation of potential barriers at ZnO – interfaces required the preparation of different metal-based electrical contacts to ZnO single crystals. Rectifying Schottky contacts were prepared on the two polar surfaces of bulk ZnO single crystals to study the interaction of positive and negative piezoelectric charges on the Schottky barrier height. Therefore, this type of contact can be seen as active element in a piezotronic device. The preparation process of the applied Ag – based Schottky contacts is described in chapter 4.1.1. On the other hand, ohmic contacts were utilized as back electrodes to sense the piezotronic modulation of other active elements in the prepared piezotronic devices. The experimental preparation process of ohmic contacts to ZnO will be summarized in chapter 4.1.2.

4.1.1. Ag – based Schottky contacts on ZnO

In order to prepare rectifying Schottky contacts on bulk ZnO single crystals, metallic Ag – electrodes were deposited on either the Zn- or O- terminated surface of a $5 \times 5 \times 5\ mm^3$ single crystal. All 6 surfaces of the ZnO single crystals (Alineason Materials Technology GmbH, Frankfurt, Germany) were mechano-chemically polished by the manufacturer. Prior to contact formation, ZnO single crystals were cleaned with acetone, ethanol, and de-ionized water in an ultrasonic bath for 5 min. Metallic Ag electrodes with a thickness of about 150 nm were provided via sputter deposition (Emitech K950X, Quorum Technologies Ltd, Laughton, UK). As already discussed in chapter 2.2.3, reliable fabrication of Schottky contacts to ZnO highly depends on extrinsic factors such as surface defect density, morphology, and chemical interactions between the metal and ZnO. All these extrinsic factors could not be precisely controlled with reasonable effort during this work. If the deposition of metallic Ag did not produce Schottky contacts with satisfying rectification behavior, an additional annealing step was conducted which is known to improve the rectifying behavior.[188] For samples utilized to study the piezotronic modulation of Ag-based Schottky contacts (chapter 5.1), an additional annealing step in air was performed at 400 °C for 2 h after sputter deposition of metallic Ag. The Schottky contact applied in the piezoelectric measurement (chapter 5.2) was based on metallic Ag.

4.1.2. Ohmic contacts on ZnO

Ohmic back contacts to ZnO single crystals with Schottky contact on either the Zn- or O-terminated surface were provided by Al/Au electrodes on the corresponding opposite side of the single crystal. Al/Au electrodes were also prepared by sputter deposition (Q300TD, Quorum Technologies Ltd, Laughton, UK). Ohmic electrodes used as contacts on the outer surfaces of the ZnO bicrystals as well as on the single crystal – polycrystal structures were also based on Al/Au.

Indium tin oxide (ITO) electrodes were used as ohmic contact on both polar surfaces of a ZnO single crystal during the study of the piezoelectric properties of a ZnO single crystal without the existence of a depletion layer (chapter 5.2). ITO electrodes were provided by sputter deposition at 400 °C in collaboration with A. Klein (Surface Science, TU-Darmstadt, Darmstadt, Germany).

4.2. Electrical characterization of metal-ZnO contacts

Current – voltage (*I-V*) and impedance measurements were used to study the electrical properties of the prepared metal-ZnO contacts. To investigate the electrical properties as a function of applied mechanical stress, *I-V* and impedance measurements could be performed inside a screw-driven load frame, as in detail described in chapter 4.2.1. To reveal a possible correlation between free charge carrier density and compensation mechanisms of the piezoelectric potential, temperature-dependent impedance measurements were performed inside a cryostat and temperature chamber, respectively (chapter 4.2.2). The experimental procedure to measure the temperature and frequency-dependent piezoelectric performance of ZnO is described in chapter 4.2.3.

4.2.1. Stress-dependent electrical characterization

Stress-dependent electrical characterization was performed inside a screw-driven load frame (Zwick Z010, Zwick GmbH & Co KG, Ulm, Germany). All measurements were conducted in the so-called d_{31} arrangement with the load being applied perpendicular to the c-axis of the crystal, while electrical measurements were performed parallel to the c-axis. Figure 4-1 schematically depicts the applied measurement arrangement. The d_{31} arrangement was chosen to avoid a direct application of mechanical stress onto the electrodes and with this unwanted changes in the contact resistivity, e.g. due to mechanical deformation of the metal electrode itself. Mechanical stress was increased to the desired stress level and held constant during the electrical measurements. The application of a low mechanical load of 5 MPa was used to contact the sample and will be treated as the stress-free state throughout this work.

I-V measurements were recorded in a range between -1 V and 1 V using a source measurement unit (Keithley 2450, Keithley Instruments Inc, Cleveland, USA). For each *I-V* curve, 201 measurement points were recorded by linearly increasing the voltage from -1 V to +1 V in steps of 0.01 V. Impedance spectra were recorded with an impedance analyzer (Alpha-A impedance analyzer, Novocontrol GmbH & Co KG, Montabaur, Germany) in a frequency range between 1 Hz and 1 MHz. The amplitude of the probing signal was set to $V_{rms} = 0.015\,V$ to ensure, that the impedance spectra are not measured under forward biasing of the Schottky contact. For equivalent circuit analysis of the impedance spectra, impedance spectrum analysis software (RelaxIS 3, rhd instruments, Marburg, Germany) was used.

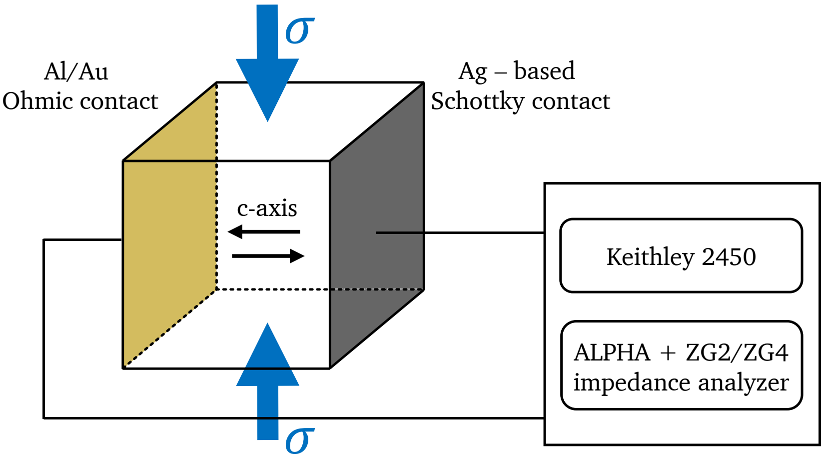

Figure 4-1: Schematic representation of the so-called d_{31} arrangement used to measure stress-dependent *I-V* and impedance data of bulk ZnO single crystals with Schottky contacts on the Zn- or O-terminated surface. Mechanical stress is applied perpendicular to the c-axis, while the electrical properties are measured parallel to the c-axis.

4.2.2. Temperature-dependent impedance measurements

Temperature-dependent impedance spectra between -120 °C and 20 °C of the ZnO single crystal with ITO electrodes on both polar surfaces were measured using a broadband impedance spectrometer with integrated temperature controller (Quatro Cryosystem with Alpha-A impedance analyzer, Novocontrol GmbH & Co KG, Montabaur, Germany). Impedance spectra were recorded in a frequency range between 1 Hz and 10 MHz and a probe signal amplitude of $V_{rms} = 0.015\,V$.

Temperature-dependent impedance spectra of the ZnO single crystal with Schottky contact were measured within a screw-driven load frame (5967, Instron GmbH, Darmstadt, Germany) equipped with a temperature chamber (TK 26.600.LN2, Fresenberger GmbH, Wipperfürth, Germany). During the measurement, only a small preload of 5 MPa was applied, which is seen as the stress-free state. Impedance spectra were recorded between -100 °C and 20 °C in a frequency range of 0.01 Hz to 10 MHz and a probe signal amplitude of $V_{rms} = 0.015\ V$.

4.2.3. Temperature-dependent direct piezoelectric measurement

All temperature and frequency-dependent piezoelectric measurements were conducted in collaboration with F.H. Schader and K.G. Webber (Friedrich-Alexander-Universität Erlangen-Nürnberg, Erlangen, Germany). Direct piezoelectric measurements were performed inside a screw-driven uniaxial load frame (5967, Instron GmbH, Darmstadt, Germany) equipped with a temperature chamber (TK 26.600.LN2, Fresenberger GmbH, Wipperfürth, Germany) as well as a piezoelectric stack actuator (P-025.80, PI Ceramic GmbH, Lederhose, Germany). The measurement system is schematically depicted in Figure 4-2 and was constructed by F.H. Schader. A detailed description is given within his PhD thesis.[189] The measurement principle is based on a modified version of the measurement circuit originally developed by Sawyer and Tower.[190] In the modified Sawyer-Tower setup, the sample is connected in series to a reference capacitor (C_{Ref}). Due to the direct piezoelectric effect, the application of a sinusoidal mechanical stress to a piezoelectric sample produces a proportional voltage or polarization response. For perfectly insulating samples, the stress-induced change in piezoelectric polarization charge equals the charge captured on C_{Ref}. Therefrom, the piezoelectric coefficient d_{33} and d_{31} can be calculated from the obtained polarization and stress amplitudes by applying equation 2.2.

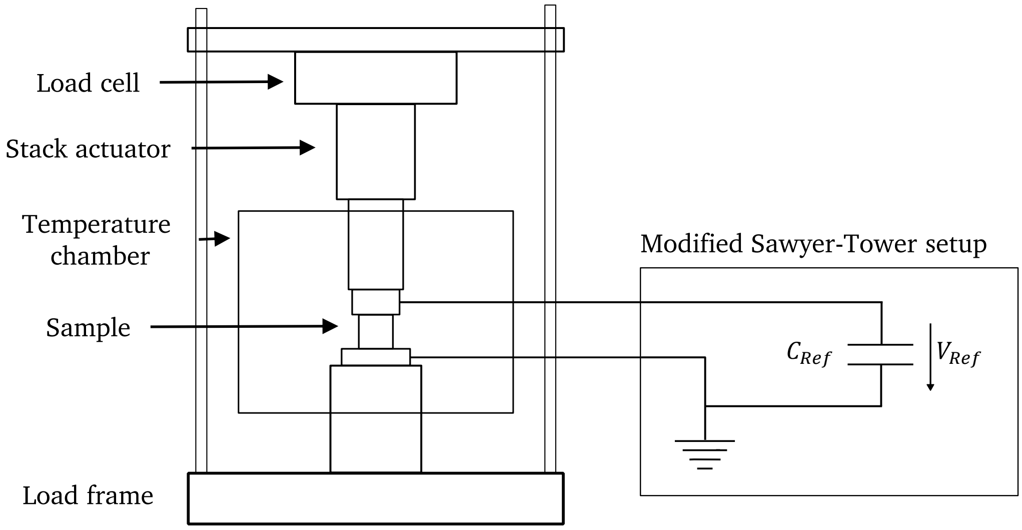

Figure 4-2: Schematic representation of the experimental setup used for temperature and frequency-dependent measurements of the piezoelectric properties in the d_{33} orientation of ZnO single crystals.

In this work, the piezoelectric stack actuator loaded the sample with a sinusoidal waveform with an amplitude of ± 2 MPa and frequencies between 1 Hz and 160 Hz. A preload of 20 MPa compressive stress was retained by the screw-driven load frame throughout the measurements to ensure good contact to the sample. The resulting polarization charge was measured with the above described modified Sawyer-Tower setup using a reference capacitor with $C_{Ref} = 4.6 \mu F$. The attached temperature chamber allowed measurements within a temperature range between -140 °C and 20 °C.

4.3. Epitaxial solid-state transformation towards ZnO bicrystals

Epitaxial solid-state transformation was facilitated to prepare ZnO bicrystals as well as single crystal – polycrystal structures with varying amount of remaining polycrystalline material in between two well oriented single crystals. A schematic of the fabrication procedure can be found in Figure 4-3. In the first step, a thin polycrystalline sacrificial layer is placed in between two ZnO single crystals. The polycrystalline sacrificial layer was prepared by a conventional mixed oxide route with the composition being that of a typical varistor ceramic. The chemical composition is chosen to introduce dopants and thereby induce electrostatic potential barriers at the ZnO-ZnO interfaces. A similar process has been previously postulated by Marks *et al.*[191] to create sapphire bicrystals with controlled misorientation. After assembling the single crystal – polycrystal – single crystal stack, diffusion bonding under a slight mechanical load provided well bonded interfaces between the single crystal and the polycrystalline layer. A subsequent high temperature treatment promotes epitaxial growth of the single crystals into the polycrystalline sacrificial layer. For sufficiently long annealing times, the two interfaces impinge and create an individual bicrystal interface with the orientation being defined by the initial orientation of the single crystals prior to the diffusion bonding step. Due to different growth rates in the O- and Zn-direction of the ZnO crystal, different annealing times were required to create individual bicrystal interfaces with changed polarity. By reducing the time for epitaxial growth, single crystal – polycrystal – single crystal structures with varying amount of remaining polycrystalline material in between two well oriented ZnO single crystals could be prepared. In the following, the experimental steps required to create individual bicrystal interfaces with control over the structural and chemical parameter by epitaxial solid-state transformation of a polycrystalline sacrificial layer will be presented. In a first step, the polycrystalline sacrificial layer with defined chemical composition is prepared by conventional mixed oxide route (chapter 4.3.1). In chapter 4.3.2, the experimental approach of assembling the single crystal – polycrystal – single crystal stack in the desired orientation will be explained. The diffusion bonding as well as the epitaxial solid-state transformation process will be described in detail in chapter 4.3.3 and chapter 4.3.4.

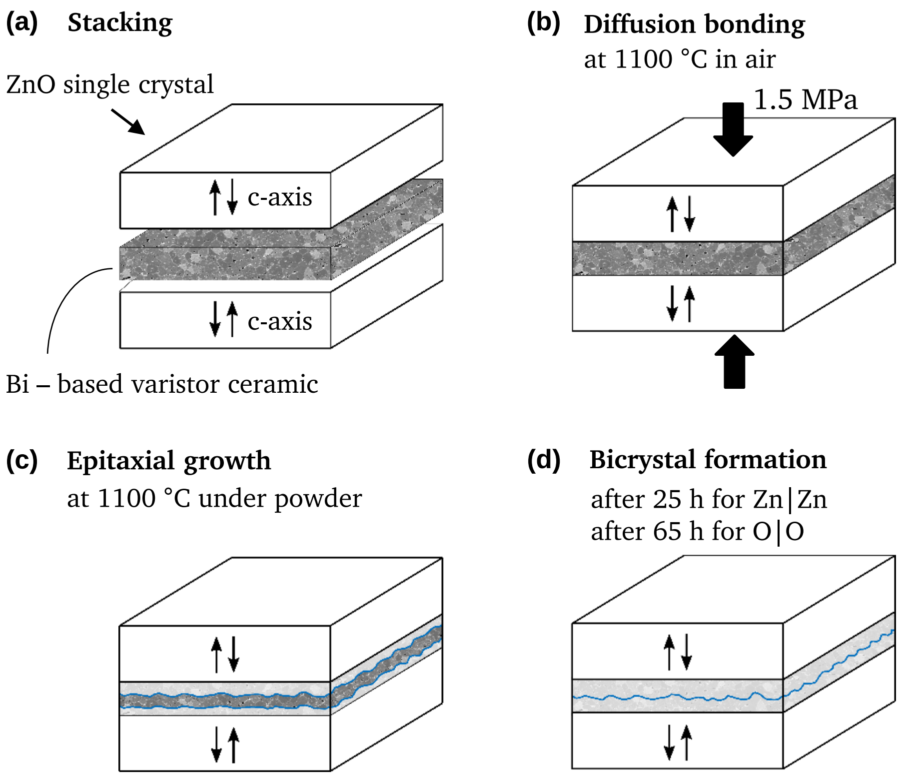

Figure 4-3: Schematic representation of the epitaxial solid-state transformation process. (a) Stacking of the polycrystalline sacrificial layer in between two single crystals with desired c-axis orientation. (b) Diffusion bonding of the single crystal – polycrystal – single crystal stack under a slight mechanical load of 1.5 MPa in air. (c) High temperature treatment at 1100 °C promotes epitaxial growth of the single crystals into the polycrystalline sacrificial layer. (d) Bicrystal formation after sufficiently long temperature treatment of 25 h for Zn|Zn- and 65 h for O|O-interfaces, respectively.

4.3.1. Preparation of polycrystalline sacrificial layer

The preparation process of the polycrystalline sacrificial layer required the following steps. Powder with the desired chemical composition was prepared by conventional solid-state reaction process. Green bodies were prepared by uniaxial and cold isostatic pressing. A following sintering step transferred the green body into a bulk polycrystalline varistor ceramics. Thin plates with the dimensions $6 \times 6 \times 0.1\ mm^3$ were machined out of the bulk ceramic. Both large surfaces of the plates were carefully polished to ensure good contact between the polycrystalline layer and the ZnO single crystals, prior to the diffusion bonding step. Figure 4-4 features a flow chart of the overall preparation process, which will be explained in detail in the following sections.

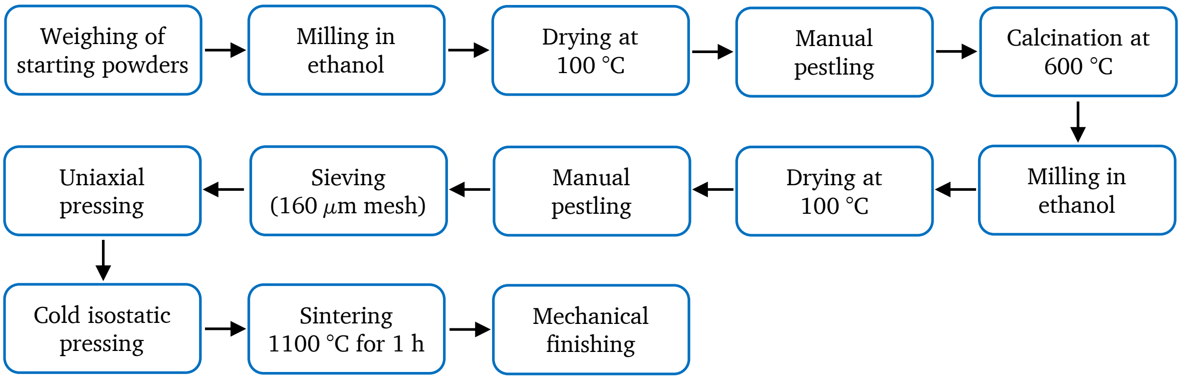

Figure 4-4: Flow chart of the preparation process for the polycrystalline sacrificial layers with varistor composition.

Powder processing

Starting powders (Alfa Aesar GmbH, Karlsruhe, Germany) were weighed in the following composition (all values given in mol%) 97.27 ZnO; 0.6 Bi_2O_3; 0.63 Co_3O_4; 0.55 $Mn(C_5H_7O_2)_2$; 0.35 Cr_2O_3; 0.6 NiO. All powders had a purity of over 99.5 %. Batches of 30 g were filled in custom made nylon milling containers together with zirconia milling balls (Mühlheimer GmbH, Bärnau, Germany) and ethanol as milling medium. Milling in a planetary ball mill (Pulverisette 5, Fritsch GmbH, Idar-Oberstein, Germany) for 20 h at 250 rpm ensured mixing and grinding of the starting powders. Drying in a ventilated furnace (Memmert GmbH + Co KG, Schwabach, Germany) was conducted for around 48 h at 100 °C in order to evaporate the ethanol. After grinding in an agate mortar, the powders were filled in alumina crucibles and sealed with a lid before a calcination step was conducted at 600 °C for 5 h using a box furnace (L9/KM, Nabertherm GmbH, Lilienthal, Germany). The heating and cooling rates were set to ± 2 K/min during the calcination step. After an additional milling and drying step as well as grinding in an agate mortar, the powders were sieved through a polymer sieve with a mesh size of 160 μm (Linker Industrie-Technik GmbH, Kassel, Germany).

Sample preparation

In order to prepare polycrystalline varistor ceramics, the prepared powder with the above-mentioned composition was uniaxially pressed into disc-shaped pellets using a steel die with an inner diameter of 15 mm. For each sample, approximately 1 g of powder was filled into the die and uniaxially compressed with 6 kN in a uniaxial hydraulic press (RC106, ENERPAC, Menomonee Falls, USA). Afterwards, the samples were vacuum sealed in latex tubes and subsequent cold isostatic pressing in an oil bath (KIP 100 E, Paul-Otto Weber GmbH, Remshalden, Germany) at 300 MPa for 90 s was applied to further increase the green body density. Green bodies were afterwards placed on a powder bed on an alumina plate. The powder bed had the same chemical composition as the green bodies. In addition, the samples were covered with the same powder, to prevent excessive evaporation of volatile constituents during the sintering process. Sintering was performed in a box furnace (L16/14, Nabertherm GmbH, Lilienthal, Germany) at 1100 °C with an isothermal sintering time of 2 h and heating and cooling rates of ± 5 K/min.

Square plates with an edge length of 6 mm were cut from the round pellets using a precision diamond wire saw (Model 4240, well Diamantdrahtsägen GmbH, Mannheim, Germany). Subsequently, the platelets were ground with a surface grinder (Typ ZB 42T, Ziersch & Baltrusch, Ilmenau, Germany) to a thickness of around 150 μm from both sides. To ensure good contact between the polycrystalline sacrificial layer and ZnO single crystals, the two surfaces of the platelets were carefully polished (Phoenix 4000, Jean-Wirtz GmbH & Co KG, Düsseldorf, Germany) using diamond paste with decreasing diamond size (15 μm, 6 μm, 3 μm, 1 μm, and 0.25 μm) and lubricant (DP Paste, DP-Lubricant Blue, STRUERS GmbH, Willich, Germany). During polishing, the thickness of the polycrystalline layers was continuously monitored and the length of the individual polishing steps was adjusted to give a final thickness of around 100 μm after the final polishing step.

4.3.2. Assembly of the single crystal – polycrystal – single crystal stack

Two side epi-polished ZnO single crystals with dimensions of $5 \times 5 \times 0.5\ mm^3$ were purchased from a manufacturer (MaTeck GmbH, Jülich, Germany). The orientation of the c-axis within the single crystalline substrates was marked. One polycrystalline sacrificial layer with the dimensions of $6 \times 6 \times 0.1\ mm^3$ was placed in between two ZnO single crystals with the c-axis of both crystals either pointing towards or away from the polycrystalline material (see Figure 4-3 (a)). The edge length of the polycrystalline layer was chosen to be slightly larger than that of the single crystals to ensure contact across the whole area even if small inaccuracies during the placement of the stack occur. To apply a small load during diffusion bonding, the stacks were placed between two alumina stamps with thin silicon carbide (SiC) platelets, separating ZnO from alumina. The SiC platelets were necessary to prevent chemical reactions between the ZnO single crystals and alumina stamps. It was found, that an oxidization step of the SiC surfaces prior to diffusion bonding also reduces chemical interactions between the ZnO single crystals and SiC plates. Surface oxidation of SiC was performed at 1100 °C for at least 5 h in ambient atmosphere inside a box furnace. During assembling, great care was taken to remove any particles from the surfaces of the single crystals as well as from the polycrystalline layer. A detailed schematic of the sample assembling sequence can be found in Figure 4-5.

4.3.3. Diffusion bonding

Diffusion bonding was performed inside a screw-driven load frame (Zwick Z010, Zwick GmbH & Co KG, Ulm, Germany), equipped with a tube furnace (LK/SHC 1500-85-150-1-V-Sonder, HTM Reetz GmbH, Berlin, Germany). A schematic of the experimental setup is depicted in Figure 4-5. For bonding, the temperature was increased to 1100 °C with a heating rate of 5 K/min. After a dwell time of 2 h, the temperature was again reduced to room temperature with a cooling rate of 5 K/min. During the entire bonding process, a small load of 1.5 MPa was provided by the load frame to ensure good contact between the single crystals and the polycrystalline sacrificial layer. Furthermore, the operation in load control mode is especially important during the heating stage, since the load frame needs to compensate for thermal expansion of the sample as well as all parts of the frame itself, which are positioned within the furnace.

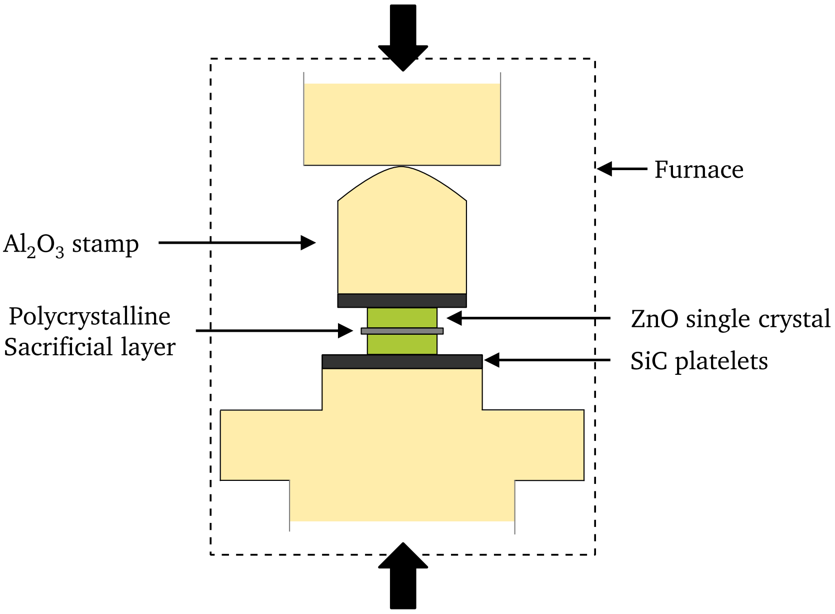

Figure 4-5: Schematic of the experimental setup for the diffusion bonding step during the bicrystal preparation process by epitaxial solid-state transformation.

4.3.4. Epitaxial solid-state transformation

After diffusion bonding, the single crystal – polycrystal – single crystal stacks were annealed at 1100 °C to promote epitaxial growth of the single crystals into the polycrystalline layer. The stacks were placed on an alumina lid in a powder bed with powder of the same chemical composition as the polycrystalline sacrificial layer. Furthermore, the platelets were covered with additional powder to prevent exaggerated evaporation of volatile constituents from the polycrystalline sacrificial layer during high temperature treatment. To promote epitaxial growth, the samples were covered by an alumina crucible and heated to 1100 °C inside a box furnace (L16/14, Nabertherm GmbH, Lilienthal, Germany). Heating and cooling rate was 5 K/min for every sample. Due to the anisotropic growth rate of ZnO in its different crystal directions, the dwell time at 1100 °C had to be adjusted depending on the desired polarity of the bicrystal interface. For the Zn|Zn-interface an isothermal annealing time of 25 h resulted in the formation of an individual interface, while for the O|O-interface a time of 65 h was necessary. By interrupting high temperature treatment at various times of epitaxial growth, single crystal – polycrystal structures with varying amount of remaining polycrystalline material were created. All structures with interrupted epitaxial growth had the single crystals oriented with the O-terminated surface in contact with the polycrystalline sacrificial layer. Annealing at 1100 °C was performed for 2, 20, 40, and 60 h. The preparation of the single crystal – polycrystal structures was conducted by Maximilian Gehringer as part of his bachelor thesis which was supervised within the scope of this doctoral thesis.[192]

4.4. Structural and electrical characterization of ZnO bicrystals and single crystal – polycrystal structures

In this chapter, the experimental procedure of the structural and electrical characterization of the ZnO bicrystal interfaces as well as the single crystal – polycrystal structures will be presented. For the bicrystalline sample scanning electron microscopy (SEM) and transmission electron microscopy (TEM) investigations were performed to reveal the structure as well as chemical composition of the individual bicrystal interface (chapter 4.4.1). Microstructural analysis was conducted on single crystal – polycrystal structures to reveal the thickness of, as well as, the grain size within the remaining polycrystalline layer (chapter 4.4.2). The experimental procedure of the electrical characterization of ZnO bicrystals and single crystal – polycrystal structures will be presented in chapter 4.4.3.

4.4.1. Structural characterization of bicrystal interfaces

All here presented SEM and TEM studies of individual bicrystal interfaces were conducted by Maximilian Trapp (doctoral student, Geo-Materials-Science, TU Darmstadt, Darmstadt, Germany). For SEM investigations, cross sections of $1.5 \times 1 \times 1\ mm^3$ were cut out of the center of the bicrystal. Polishing of one of the surfaces perpendicular to the interface was performed using a polishing system (Allied MultiPrep, Allied High Tech Products Inc, Rancho Dominguez, USA) with diamond lapping films of decreasing grain size starting from 15 μm down to 0.1 μm. The polished surface was chemically etched with hydrochloric acid solution (5% HCl/H_2O) for

8 s in order to increase the contrast between the ZnO-ZnO interface and the bulk material. SEM images were recorded on a Schottky field emission scanning electron microscope (JEOL JSM 7600F, JEOL, Tokyo, Japan).

For TEM investigation, thin foils of the bicrystal cross sections were machined out of the sample by grinding and polishing using the Allied MultiPrep system. The resulting foils were mounted on molybdenum TEM grids (100 mesh, Plano, Wetzlar, Germany). Subsequent argon ion beam milling (DuoMill 600, Gatan, Pleasanton, USA) was conducted until perforation occurred and electron transparency was ensured in the interface region. TEM investigation was performed on a field emission electron microscope (JEOL JEM 2100F, JEOL, Tokyo, Japan) and a C_S corrected scanning TEM (JEOL JEM ARM 200F, JEOL, Tokyo, Japan) which was equipped with two EDS detectors (TEM 250 SDD, Oxford instruments, Abingdon, England and JED 2300T, JEOL, Tokyo, Japan).

4.4.2. Structural characterization of single crystal – polycrystal structures

For microstructural analysis, cross sections of the single crystal – polycrystal structures were prepared. The samples were cut in the center of the sample and the resulting cross sections were polished using diamond paste down to a grain size of 0.25 μm Details on the polishing procedure can be found in chapter 4.3.1. Subsequent chemical etching in hydrochloric acid solution (5% HCl/H_2O) for 8 s revealed the microstructure of the remaining polycrystalline material. SEM images were recorded across the whole cross-sectional interface of the samples using a high-resolution scanning electron microscope (XL 30 FEG, Philips, Mawah, USA).

The grain size within the remaining polycrystalline layer was determined using an image processing software (ImageJ, National Institute of Health, Bethesda, USA) by determining the sectional area of at least 200 grains for each structure.

4.4.3. Electrical characterization

Electrical contacts were provided by depositing Al/Au electrodes onto the outer surfaces of the ZnO bicrystals and single crystal – polycrystal structures as described in chapter 4.1.2. To perform stress-dependent electrical characterization, the load frame (Zwick Z010, Zwick GmbH & Co KG, Ulm, Germany) was equipped with tungsten carbide electrodes. In contrast to the stress-dependent measurements on metal-based Schottky contacts to bulk ZnO single crystals (see chapter 4.2.1), stress-dependent characterization of the bicrystals and single crystal – polycrystal structures was performed in the so-called d_{33} arrangement as schematically depicted in Figure 4-6.

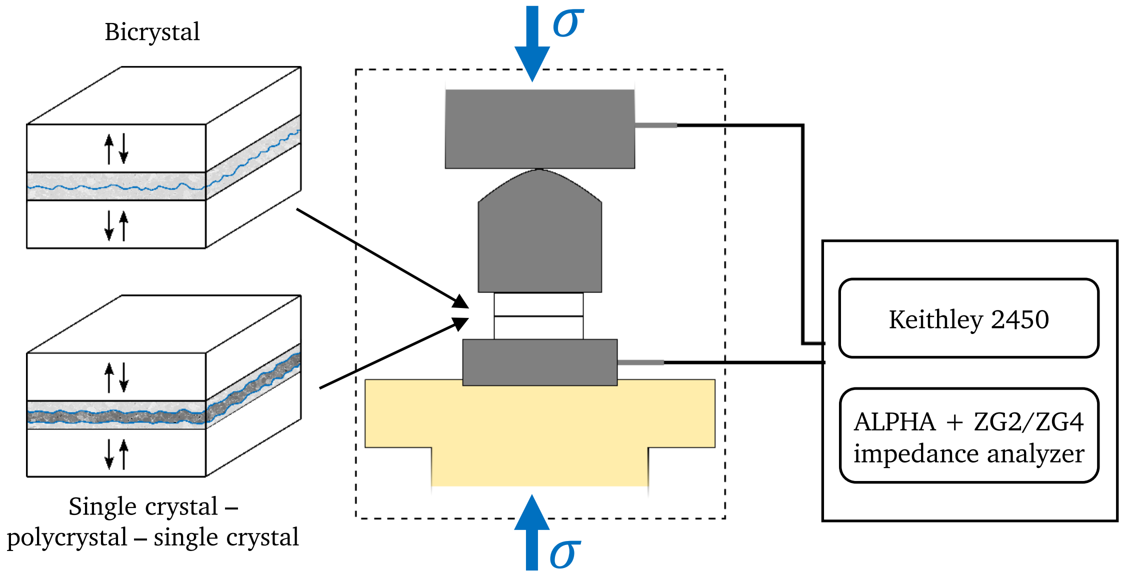

Figure 4-6: Schematic representation of the measurement setup used for stress-dependent electrical characterization of ZnO bicrystals as well as singe crystal – polycrystal structures. The stress is applied parallel to the c-axis, hence, in d_{33} arrangement.

For *I-V* measurements, the load frame was connected to a source measurement unit (Keithley 2450, Keithley Instruments Inc, Cleveland, USA). Stress-dependent *I-V* measurements were recorded under increasing uniaxial compressive stress between 5 and 250 MPa in steps of 45 and 50 MPa, respectively. For electrical measurements on bicrystalline samples, the voltage was increased from 0.1 V to 5 V with logarithmically increasing the step width between individual measurement points. In addition, the maximum current output was limited to 100 mA in order to prevent electrical degradation of the electrostatic potential barrier during *I-V* measurements. For single crystal – polycrystal structures, the same parameters were used but due to the higher overall electrical resistance, the maximum voltage was increased from 5 V to 10 V.

By replacing the source measurement unit with an impedance analyzer (Alpha-A impedance analyzer, Novocontrol GmbH & Co KG, Montabaur, Germany), impedance spectra were recorded in a frequency range between 0.5 Hz and 1 MHz, in the case of bicrystalline samples. For single crystal – polycrystal structures, the frequency range was extended in the lower range to 0.01 Hz to account for the higher overall electrical resistance of the samples, which reduces the frequency range where the sample is measured in dc condition. The amplitude of the probe signal was set to $V_{rms} = 0.015\ V$ to ensure, that the impedance spectra are not measured in the breakdown region of the *I-V* curve. Impedance spectra under the application of uniaxial compressive stress were recorded in the same stress range as applied for the stress-dependent

I-V measurements. To determine the effective potential barrier height, stress- and temperature-dependent impedance spectra were recorded. The temperature was increased from room temperature to 124 °C in steps of around 20 °C using the tube furnace (LK/SHC 1500-85-150-1-V-Sonder, HTM Reetz GmbH, Berlin, Germany) attached to the load frame. At each step, the temperature was stabilized for 30 min and the sample temperature was determined with a thermocouple placed within the lower tungsten carbide stamp. Besides recording impedance spectra at constant levels of stress, continuous conductivity measurement could be performed by linearly increasing and decreasing the applied uniaxial compressive stress while the conductance of the sample was continuously measured with the impedance analyzer at a frequency of 50 Hz.

5. Results and discussion

5.1. Piezotronic effect of metal-ZnO single crystal contact

To elucidate the influence of piezoelectric polarization charge on the potential barrier height of Schottky contacts to bulk ZnO single crystals, Ag-based Schottky contacts were deposited on either the Zn- or O-terminated surface of a 5x5x5 mm^3 ZnO single crystal. In contrast to ZnO nanostructures, the use of bulk crystals allows for a well-defined stress distribution and may confirm and extend existing studies, which were mainly conducted on nanostructure devices. In the first part of this section (chapter 5.1.1), the prepared Schottky contacts are characterized in the stress-free state. In chapter 5.1.2, the modification of Schottky barrier properties under the influence of positive and negative polarization charges are presented. Finally, the experimental observations will be compared to theoretical models in chapter 5.1.3. Parts of the presented data in this chapter have been previously published in an article for the Journal of Applied Physics.[193]

5.1.1. Schottky barrier characterization in the stress-free state

To prove the successful preparation of rectifying Schottky contacts, current density – voltage (*J-V*) measurements were recorded in the stress-free state and are depicted in Figure 5-1.

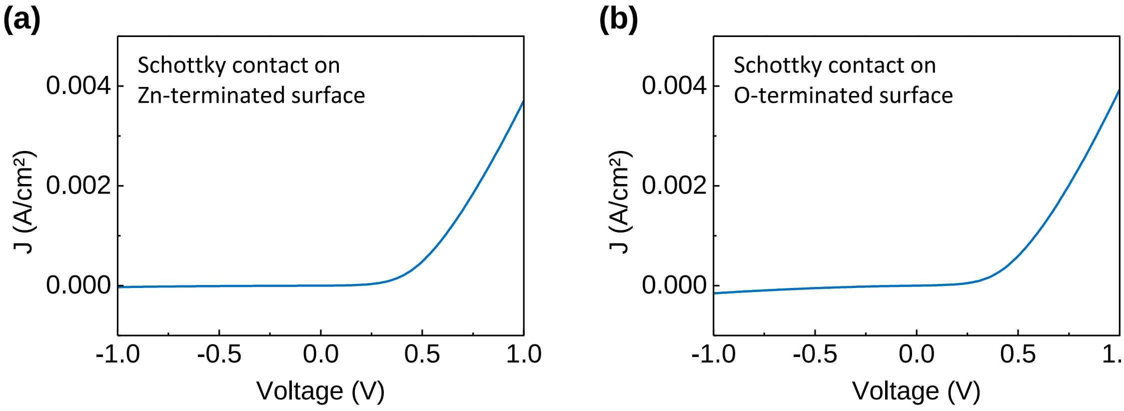

Figure 5-1: Linear representation of the stress-free *J-V* measurements of Ag-based Schottky contacts on the Zn-terminated (a) and O-terminated (b) surface of a 5x5x5 mm^3 ZnO single crystal.

Both contacts feature a rectifying behavior. Under forward biasing (positive V), a nonlinear increase in current density (*J*) can be observed. When the applied voltage is negative and the Schottky contact is operated under reverse biasing, only a comparably small current density flows through the device. Schottky diode parameters like the potential barrier height (Φ_{SB}) and the ideality factor (η) of the prepared contacts can be determined by further analyzing the *J-V* characteristics under forward biasing. As described in chapter 2.2.2, current transport across Schottky contacts can be facilitated by thermionic emission across the barrier, tunneling or field emission through the barrier as well as recombination in the space charge region and minority carrier injection. In this work, pure thermionic emission is assumed to determine the Schottky diode parameters. To perform the thermionic analysis of the forward biased Schottky contact, the semi-logarithmic plot of the *J-V* characteristics can be utilized (see Figure 5-2).

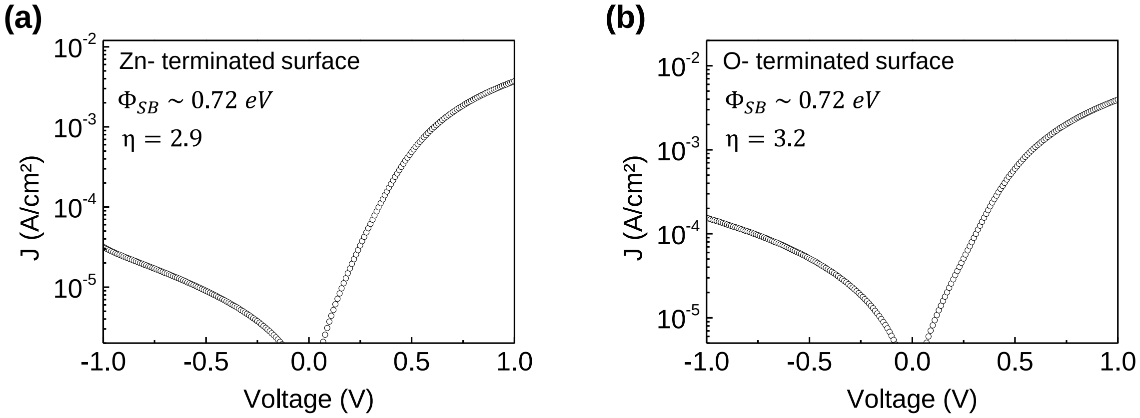

Figure 5-2: Semi-logarithmic representation of the *J-V* characteristics of the Schottky contacts on the Zn-terminated (a) and O-terminated (b) surface of a 5x5x5 mm^3 ZnO single crystal.

By fitting the linear part of the current density under forward biasing, the saturation current density (J_0) can be determined. From equation 2.14, the potential barrier height of both contacts is calculated. For the calculations, the theoretical Richardson constant ($A^* = 4\pi q m^* k^2 h^{-3}$) with the effective electron mass ($m^* = 0.27 m_0$) of ZnO ($A^* = 32\ Acm^{-2}K^{-2}$) is used.[194] For both contacts a potential barrier height of $\Phi_{SB} \sim 0.72\ eV$ is determined. The determined value of Φ_{SB} is in the range of previously reported potential barrier heights for Ag-based Schottky contacts to n-type ZnO which are in the range of 0.6 to 0.8 eV.[195] Allen and Durbin[104] attributed the narrow distribution of reported Φ_{SB} to a possible formation of near-surface oxygen vacancies. The defect level of oxygen vacancies is 0.7 eV below the conduction band minimum and may be responsible for a pinning of the Fermi-level. The here studied Ag contacts were annealed after the metal deposition, through which oxygen vacancies may be formed in a higher concentration. It should be noted, that the determined Φ_{SB}, from only the forward current response at room temperature may only be a rough approximation of the real value, especially for contacts with large spatial inhomogeneity.[196] Since the studied Schottky contacts have a large area (25 mm^2), a spatial variation in Φ_{SB} is expected. By plotting $d(V)/d(ln(J))$ vs J, the ideality factors for both contacts are determined.[197] The high values of the ideality factor $\eta = 2.9$ for the contact on the Zn-terminated surface and $\eta = 3.2$ for the contact on the O-terminated surface can be partially attributed to local Φ_{SB} variations. Additional transport mechanisms like tunneling or recombination currents which can contribute to the overall current density besides thermionic emission were also ascribed to cause high ideality factors.[198] The higher ideality factor for the contact deposited on the O-terminated surface can also explain the higher reverse current density compared to the contact on the Zn-terminated surface, even if they feature the same apparent Φ_{SB} after thermionic analysis.

Despite the fact, that the ideality factor of the obtained *J*-*V* curves significantly deviates from unity, the formation of a rectifying Schottky contact is evident from the measurements in the stress-free state. Therefore, the prepared contacts on the two polar surfaces of a bulk ZnO single crystal are suitable to study the mechanical modulation of the Schottky barrier height by positive or negative piezoelectric polarization charges.

5.1.2. Stress-dependent modulation of Schottky barrier height

To study the impact of piezoelectric polarization charge on Φ_{SB}, *J*-*V* measurements were performed under uniaxial compression inside a screw-driven load frame (see Figure 4.1). A uniaxial compressive stress of up to 70 MPa was applied on the basal plane of the ZnO single crystal (perpendicular to the c-axis), while the current was measured along the c-axis. By choosing this arrangement, a direct application of mechanical stress on the metal electrodes was prevented, eliminating unwanted effects on the electrical conductivity e.g. by mechanical deformation of the electrode material. In the chosen configuration, the piezoelectric coefficient d_{31} gives positive polarization charge on the Zn-terminated surface under uniaxial compression and negative piezoelectric charge on the O-terminated surface, respectively (see Figure 2-2 (c)). Therefore, a decreasing Φ_{SB} for the Schottky contact on the Zn-terminated surface and an increasing Φ_{SB} for the Schottky contact on the O-terminated surface is expected for increasing level of stress. Figure 5-3 shows the *J*-*V* measurements for both contacts under increasing uniaxial compressive stress.

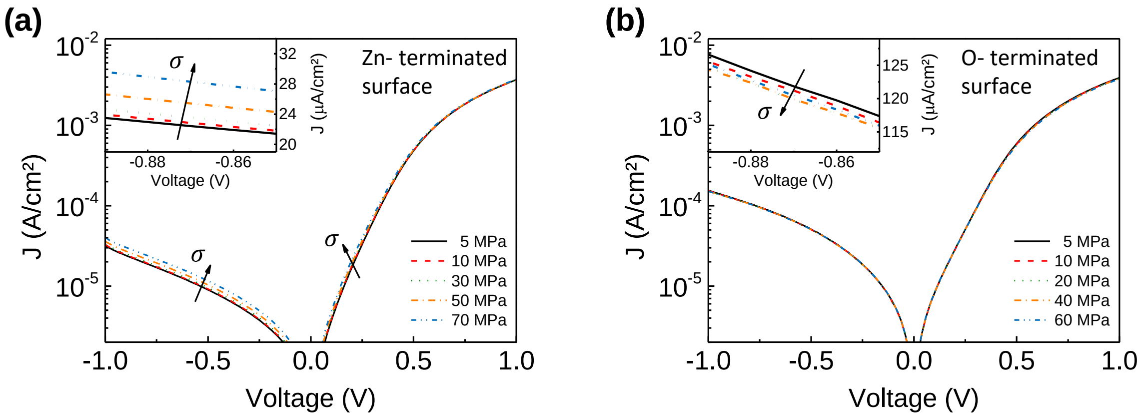

Figure 5-3: Stress-dependent *J-V* measurements of Schottky contacts on Zn-terminated surface (a) and O-terminated surface (b) of a bulk ZnO single crystal.

With increasing mechanical stress, a small increase in current density can be observed in reverse and forward biasing for the Schottky contact deposited on the Zn-terminated surface of the ZnO single crystal. On the other hand, the Schottky contact on the O-terminated surface features a moderate decrease of conductivity with increasing mechanical stress at least under reverse bias. The physical origin of the different magnitudes of observed conductivity change for the increasing and decreasing barrier is not clear. Barrier inhomogeneity may prevent a profound determination for increasing barriers. However, the fundamental concept of the piezotronic effect, a decrease in Φ_{SB} for positive piezoelectric charge and an increase in Φ_{SB} for negative piezoelectric charge can be confirmed.[36] The small decrease in current density measured on the O-polar surface verifies, that the increasing conductivity measured on the Zn-terminated surface is a consequence of the piezotronic interaction between stress-induced piezoelectric charges and Φ_{SB}. If other mechanisms, like the piezoresistive effect, would dominate the stress dependence, the Zn- and O-terminated surfaces would show the same characteristic and no dependence on the crystal polarity would be present.

To confirm the stress-dependent results obtained by *J-V* measurements, in-situ impedance measurements as a function of stress have been conducted for the Schottky contact on the Zn-terminated surface. By sweeping a small ac field over a wide frequency range, impedance spectroscopy is a powerful and easy tool to study electrical properties and current transport mechanisms of interfaces.[199-201] Figure 5-4 (a) features the obtained impedance spectra under increasing mechanical stress in the Nyquist representation and Figure 5-4 (b) depicts the real part of impedance ($Re(Z)$) as a function of frequency (ν).

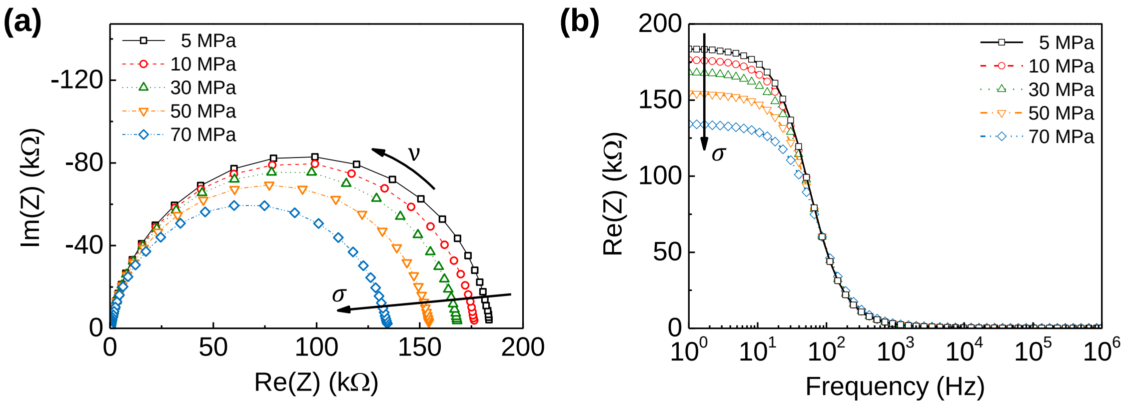

Figure 5-4: (a) Nyquist representation of the impedance spectra recorded of the Ag-based contact on the Zn-terminated surface under increasing uniaxial compressive stress in the d_{31} direction. (b)Stress-dependent real part of impedance as a function of frequency (ν) for the applied ac field.

With increasing mechanical stress, the low frequency component of $Re(Z)$ decreases. It is expected, that the low frequency response of $Re(Z)$ is dictated by the electrical properties of the Schottky contact and therefore, that the decrease in $Re(Z)$ at low frequencies is caused by the piezotronic lowering of Φ_{SB}. A similar impedance response can be observed at forward biased Schottky contacts, where an applied dc voltage reduces Φ_{SB} and a decrease in the low frequency $Re(Z)$ can be observed.[202] By performing an equivalent circuit analysis of the impedance data, electrical parameters of the Schottky contact can be extracted as a function of mechanical stress. An equivalent circuit composed of resistance (R) and capacitance (C) networks can be used to fit the experimental data. Typically, a Schottky junction is represented by a parallel connected RC element and a series resistance.[203, 204] Since the ohmic back contact may not be perfect and additional capacitive components could contribute to the overall impedance response, an RC element is added in series to the equivalent circuit. The utilized equivalent circuit is shown in Figure 5-5 (a). The first RC element represents the Ag-based Schottky contact with C_1, the depletion layer capacitance and R_1, the shunt resistance. The series resistance R_2 accounts for the resistance of the bulk ZnO single crystal. The second RC element quantifies the resistance of the ohmic contact (R_3) and a possible capacitive contribution from a depletion region in the vicinity of the Al/Au-based ohmic contact (C_3).

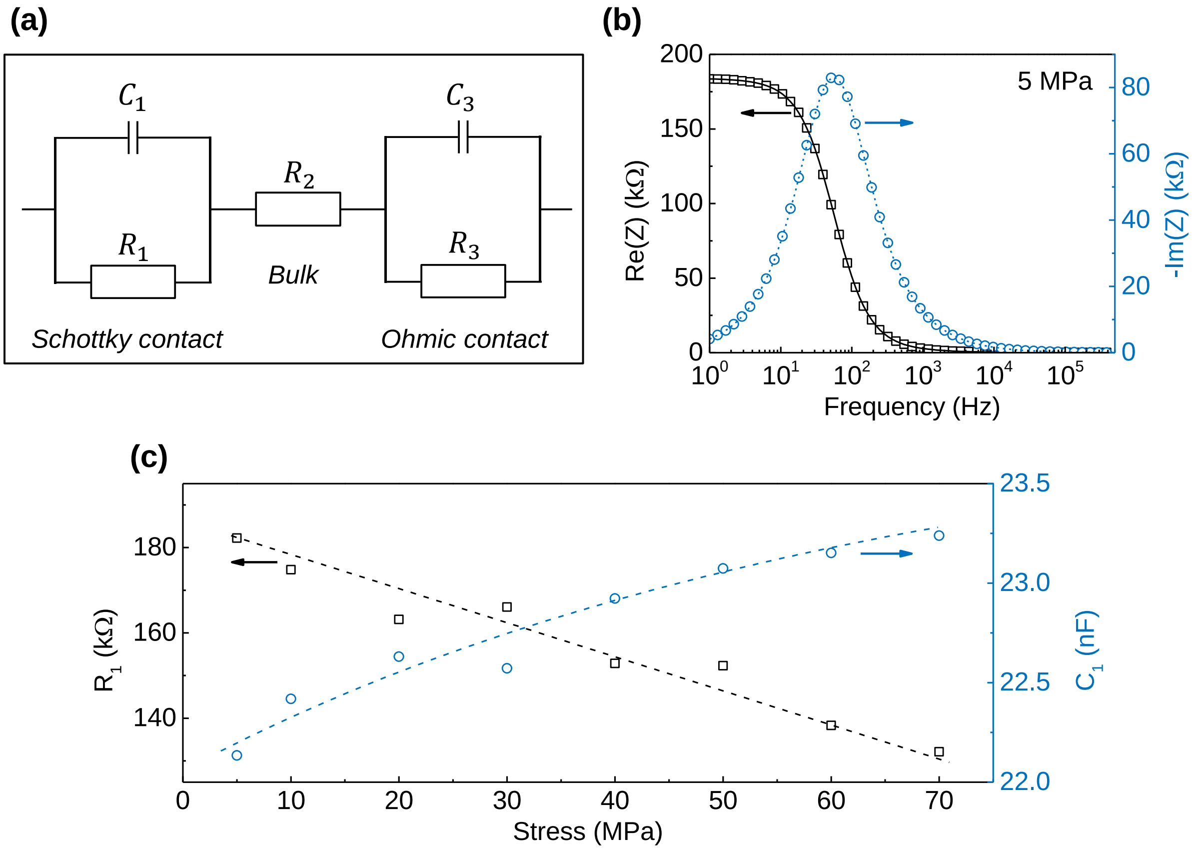

Figure 5-5: (a) Equivalent circuit to model the impedance response of the Schottky contact. (b) Spectroscopic plot of real ($Re(Z)$) and imaginary ($Im(Z)$) part of impedance for the measurement at 5 MPa. The lines represent the simulated response based on the equivalent circuit. (c) Extracted values of the shunt resistance and capacitance of the Schottky contact as a function of increasing uniaxial compressive stress.

The ac impedance of the overall circuit is given by:

$$Z(\nu) = Z'(\nu) - jZ''(\nu), \tag{5.1}$$

with Z' and Z'' being the magnitudes of the real and imaginary parts of the impedance and ν represents the frequency. For the equivalent circuit as depicted in Figure 5-5 (a), Z' and Z'' are given by:

$$Z'(\nu) = \frac{R_1}{1 + (\nu C_1 R_1)^2} + R_2 + \frac{R_3}{1 + (\nu C_3 R_3)^2}, \tag{5.2}$$

and

$$Z''(\nu) = \frac{\nu R_1^2 C_1}{1 + (\nu C_1 R_1)^2} + \frac{\nu R_3^2 C_3}{1 + (\nu C_3 R_3)^2}. \tag{5.3}$$

During the fitting procedure, the capacities C_1 and C_3 were replaced by constant phase elements (CPE) to account for deviations of the capacitance branch from ideal behavior. The impedance of a CPE is given by:

$$Z_{CPE} = \frac{1}{Q_{CPE}(j\nu)^{\alpha_{CPE}}}, \tag{5.4}$$

with Q_{CPE} the CPE parameter and α_{CPE} the CPE exponent. When $\alpha_{CPE} = 1$, the CPE represents an ideal capacitor and for $\alpha_{CPE} = 0$, the CPE represents an ideal resistor.

Equations 5.1 to 5.4 were used to fit the experimental data. Figure 5-5 (b) shows the spectroscopic plot of the real and imaginary impedance data (symbols) as well as the simulated response based on the equivalent circuit analysis (lines) for the measurement at 5 MPa. The simulation based on the fits represent the experimental measurement with good agreement. By following this procedure, the electrical data of the Schottky and ohmic contact as well as the bulk resistance could be extracted as a function of mechanical stress. The bulk resistance does not show a stress dependence with a constant value of R_2 between 66 and 72 Ω. The resistance of the ohmic contact (R_3) does also not feature profound variation with mechanical stress but shows higher fluctuations with R_3 varying between around 1500 and 2300 Ω. The CPE exponent (α_{CPE}) of the ohmic contact was in the range of 0.72, which deviates from pure resistive behavior but is also far from describing an ideal capacitor.

In contrast to the electrical parameter for the bulk and ohmic contact, the parameters attributed to the Schottky contact clearly show a dependence on the applied mechanical stress (see **Figure 5-5 (c)**). The resistance R_1 decreases by ~ 27 % from 182 kΩ at 5 MPa to 132 kΩ at 70 MPa. The decrease in R_1 by 27 % is in the same range as the reverse bias current increase in the *J*-*V* measurement as depicted in Figure 5-3 (a). The decrease in resistance of the Schottky contact is accompanied by a simultaneous increase in capacity (C_1). In difference to the ohmic contact, the CPE exponent (α) of the Schottky contact is above 0.93 for all applied mechanical stresses. Hence, an almost ideal capacitive behavior can be assumed for the C_1-branch of the Schottky contact. The capacitance of the depletion layer of a Schottky contact without the application of an additional dc voltage is given by:[92]

$$C = \sqrt{\frac{q\varepsilon_r\varepsilon_0 N_D}{2(\Phi_{SB} - \xi - kT/q)}}, \tag{5.5}$$

with ξ being the difference between E_F and the CBM. It is evident from equation 5.5, that a reduction in Φ_{SB} is accompanied by an increase in the depletion layer capacitance. It is difficult to determine the exact value of Φ_{SB} from only the capacitance of the depletion layer, since it highly depends on the donor density (N_D). From the bulk resistance (R_2) or the bulk resistivity (ρ_2), respectively, N_D could be approximated for the n-type ZnO bulk material by:

$$\rho = \frac{1}{qn\mu_n}, \tag{5.6}$$

with n the concentration and μ_n the mobility of electrons. In n-type ZnO the electron concentration can be assumed to be approximately the donor concentration ($n \approx N_D$). With the literature value of $\mu_n \approx 200\,cm^2V^{-1}s^{-1}$, this simple approximation gives $N_D = 10^{14}\,cm^{-3}$.[205] With the number for N_D, the obtained values of C_1 as depicted in Figure 5-5 (c) result in unrealistically small values for Φ_{SB}. This may be due to the fact, that in ZnO deep donor states can contribute to N_D in the depletion region or that N_D is not constant throughout the bulk material. Still, regardless of the absolute numbers, the proportionality of C on Φ_{SB} as described by equation 2.5 can be observed in the determined values of C_1. A linear decrease in Φ_{SB} would rationalize the observed course of the curve for C_1 depicted in Figure 5-5 (c).

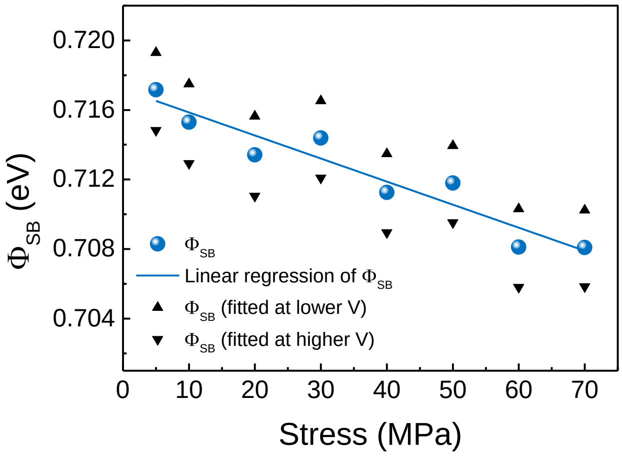

Figure 5-6: Experimentally determined reduction in potential barrier height as a function of applied mechanical stress. The potential barrier height was calculated from a linear fit between 0.2 V and 0.4 V to the forward *J-V* characteristic measured for the different stress level. In addition, corresponding values are given for fits conducted at lower (0.18-0.38 V) and higher (0.22-0.42 V) voltages.

To quantitatively describe the influence of mechanical stress on Φ_{SB}, the forward *J-V* characteristic of the Schottky contact on the Zn-terminated surface is further analyzed and Φ_{SB} is extracted as a function of stress (see Figure 5-6). With increasing mechanical stress, a clear decrease in potential barrier height can be determined from thermionic analysis. Depending on the deployed fitting range, the absolute values of Φ_{SB} show slight variations, but the overall trend is linear. From the linear regression, a moderate change in Φ_{SB} of about 9 meV can be achieved under the application of 70 MPa.

An increase in reverse and forward bias current, the decrease in shunt resistance as well as the increase in depletion capacitance strongly indicate a linear decrease in Φ_{SB}. Furthermore, the absence of a stress sensitivity for the bulk resistance and the resistance of the ohmic contact support the assumption, that the overall stress dependence is determined by the piezotronic modulation of the Schottky contact and not by the classical piezoresistive effect.
In the following chapter, the experimentally determined change in Φ_{SB} will be contrasted to theoretical models, which were introduced in chapter 2.2.5.

5.1.3. Comparison to theoretical models

In this chapter, the experimentally determined change in Φ_{SB} will be compared to the theoretical description of the piezotronic effect as proposed by Zhang *et al.*[36] as well as to the imperfect screening model as described by Stengel *et al.*[127] Both models describe the impact of stress-induced piezoelectric polarization charges on the initial potential barrier height (Φ_{SB}^{0}) of a Schottky contact. The models were introduced within chapter 2.2.5. A spatial separation between the piezoelectric charge and the screening charges within the metal electrode is required to change the electric field distribution at the contact and by this modifies Φ_{SB}. The difference between both models is, how the origin of the separation is assumed. Zhang *et al.* introduce a distribution of the piezoelectric charge over a finite distance (W_{Piezo}), whereas Stengel *et al.* assume a thin interfacial layer with defined thickness (δ_{Gap}) separating the charges. The different assumptions of the physical origin of the separation results in small dissimilarities between the two models. Therefore, a closer look has to be taken to equation 2.19 and 2.21. From equation 2.19, the change in potential barrier height ($\Delta\Phi_{SB}^{Zhang}$) after the model by Zhang *et al.* is given by:

$$\Delta\Phi_{SB}^{Zhang} = \frac{q^2 \rho_{Piezo} W_{Piezo}^2}{2\varepsilon_r \varepsilon_0}. \tag{5.7}$$

On the other hand, following the imperfect screening model as described by equation 2.12, $\Delta\Phi_{SB}^{IS}$ is given by:

$$\Delta\Phi_{SB}^{IS} = \frac{qQ_P\delta_{Int}}{\varepsilon_{Int}\varepsilon_0}. \tag{5.8}$$

As it can be seen from equation 5.7 and 5.8, $\Delta\Phi_{SB}$ linearly depends on ρ_{Piezo} and Q_P, respectively. The piezoelectric charge distribution ρ_{Piezo} is given in units of elementary charge per cubic meter ($1/m^3$), whereas Q_P is given as a sheet charge in (C/m^2). From classical piezoelectric theory as described by equation 2.2, the piezoelectric polarization charge P is also calculated to be a sheet charge in units of (C/m^2). Hence, $Q_P = P = d_{31}\sigma$ rationalizes the observed linear dependence of Φ_{SB} on the applied mechanical stress as it is observed in the experiment. To derive the piezoelectric charge distribution ρ_{Piezo} from $P = d_{31}\sigma$, P can be divided by q and W_{Piezo}. From this consideration and with $P = Q_P$, equation 5.7 changes to:

$$\Delta\Phi_{SB}^{Zhang} = \frac{qQ_P W_{Piezo}}{2\varepsilon_r\varepsilon_0}. \tag{5.9}$$

By comparing equation 5.8 and 5.9, it is evident, that both models linearly depend on $Q_P = d_{31}\sigma$. The distances W_{Piezo} and δ_{Int} both account for a spatial separation between the piezoelectric polarization charges (Q_P) and the screening charges in the metal electrode (Q_M). Differences in the models can be seen in the denominator of equations 5.8 and 5.9. Since the model from Zhang *et al.* assumes a spatial distribution of the piezoelectric charges, as depicted in Figure 2-8 (d), the solution of the Poisson equation results in a factor of 2 in the denominator during mathematical integration. The charge separation in the imperfect screening model is that of a plate capacitor which results in a constant field distribution, hence the factor of 2 is absent in $\Delta\Phi_{SB}^{IS}$. The electric field, which is responsible for the modulation of Φ_{SB}, depends on the permittivity of the material between the separated charges. In the model from Zhang *et al.* the piezoelectric charges are assumed to be distributed within the semiconducting ZnO, therefore, ε_r in equations 5.7 and 5.8 is likely to be approximated by the dielectric constant of ZnO, which is around 9. This assumption is analogous to the general electrostatic analysis of the Schottky barrier formation process.[92] A higher uncertainty arises for the dielectric constant (ε_{Int}) of the interfacial layer within the imperfect screening model. The model from Stengel *et al.* assumes the interfacial layer to be a vacuum layer, therefore $\varepsilon_{Int} = 1$.[127, 206, 207] This assumption would represent the case in which the piezoelectric charge has its maximum impact on Φ_{SB} for a given interfacial distance δ_{Int}. Other authors did not assume the layer to be a vacuum layer but used the permittivity of the semiconducting or ferroelectric material as ε_{Int}.[15, 16] This would reduce the stress sensitivity by a factor proportional to ε_{Int}.

In Figure 5-7, the two different models after equations 5.7 and 5.8 are compared to the experimentally determined change in potential barrier height for different assumptions of W_{Piezo} and δ_{Int}.

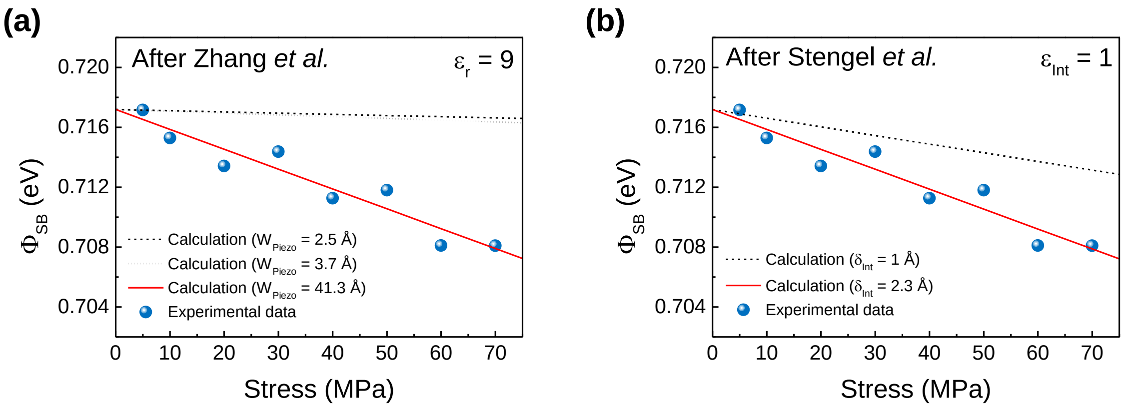

Figure 5-7: Experimental (blue dots) and calculated (lines) potential barrier height as a function of mechanical stress. In (a), the calculations are based on the model proposed by Zhang *et al.*[36] whereas the calculations in (b) are based on the imperfect screening model as described by Stengel *et al.*[127]

In Figure 5-7 (a), the experimental Φ_{SB} as a function of stress is compared to the theoretical model proposed by *Zhang et al*. To calculate the amount of piezoelectric polarization charge, the transverse piezoelectric coefficient of ZnO was assumed with $d_{31} = -5.12\ pC/N$.[61] As it can be seen from the dashed and dotted black lines, an assumed distribution of piezoelectric charges with a width W_{Piezo} of 2.5 and 3.7 Å as proposed in literature cannot rationalize the experimental findings.[36, 122] To achieve the observed change in Φ_{SB}, W_{Piezo} would have to increase to 41.3 Å. Such a high value is by a factor of 10 larger than proposed in literature.[36, 122] In contrast, the imperfect screening model (Figure 2-7 (b)) features a much higher stress sensitivity. This is mainly due to the assumption of the vacuum layer separating piezoelectric and metal screening charges and the concurrently lower permittivity value in the denominator of equation 5.8. By assuming δ_{Int} to be 2.3 Å, the experimental reduction in potential barrier height can be well described. The interface layer thickness of around 2 Å is in agreement with literature, where the thickness of the interfacial layer between metals and semiconductors is reported to be in the range of a few Angstroms.[92] It should be noted, that the main difference between both models arises from the assumption of ε_{Int}. If for both models the same value of $\varepsilon_{Int} = 1$ would be assumed, the model from Zhang would give almost the same results as the imperfect screening model for $W_{Piezo} = 3.7$ Å as given in literature.

5.1.4. Summary – Piezotronic effect at metal-ZnO Schottky contact

Stress-dependent J-V measurements across Schottky contacts on the Zn- and O-terminated surfaces of a bulk ZnO single crystal confirm the fundamental theory of the piezotronic effect. For the generation of positive piezoelectric polarization charges, an increase in conductivity is observed, while the generation of negative piezoelectric charges results in a decreased conductivity. The magnitude of barrier change for a decreasing potential barrier is experimentally determined to be ~9 meV at 70 MPa. As expected from theory, a linear correlation between potential barrier height and mechanical stress can be confirmed. By applying the imperfect screening model as described by Stengel *et al.*[127], the experimental observation can be rationalized. A comparison between model and experiment indicates a thickness for the interfacial layer of ~2 Å.

Regarding further development of piezotronic devices based on metal-semiconductor Schottky contacts, the following conclusion can be drawn. To increase the stress sensitivity, the distance between the piezoelectric charges and the screening charges within the metal is of utmost importance. The attainable change in potential barrier height is directly proportional to the gap thickness, therefore δ_{Gap} should be maximized e.g. by introducing an artificial dead-layer. On the other hand, the dead-layer needs to be thin enough to be transparent for electrons, making it difficult to profoundly increase the stress sensitivity of piezotronic devices based on metal-semiconductor Schottky contacts.

5.2. Piezoelectric measurements on ZnO single crystals

The performance of piezotronic devices is directly related to the number of stress-induced piezoelectric polarization charges. The piezoelectric properties of a material are defined by its crystal structure and bond character. In piezoelectric materials with high intrinsic conductivity like ZnO, free charge carriers can cancel the piezoelectric polarization. This screening mechanism was also discussed in the field of ZnO-based piezotronics, where the screening was held responsible for low stress sensitivities as well as high operating frequencies required for energy harvesting applications.[59, 130] To shed light on the screening mechanism and its influence on piezotronic applications, temperature- and frequency-dependent measurements of the piezoelectric coefficient were performed. Furthermore, the influence of different electrical contacts on the attainable piezoelectric coefficient will be examined. In the first part of this section (chapter 5.2.1), the temperature- and frequency-dependent piezoelectric response of a bulk ZnO single crystal with ohmic contacts is presented. Equivalent circuit analysis is applied to explain the experimental data. In chapter 5.2.2 one ohmic contact is replaced by a Schottky contact, to study the influence of a depletion layer on the attainable piezoelectric output and therefore on possible piezotronic applications. Parts of the presented data have been previously published in an article in Acta Materialia.[208]

5.2.1. Piezoelectric measurements on a ZnO single crystal with ohmic contacts

To prove the successful preparation of ohmic contacts and the absence of depletion regions, respectively, the *J*-*V* response was measured between -2 and 2 V. Figure 5-8 features the linear (a) and semi-logarithmic (b) representation of the *J*-*V* measurement:

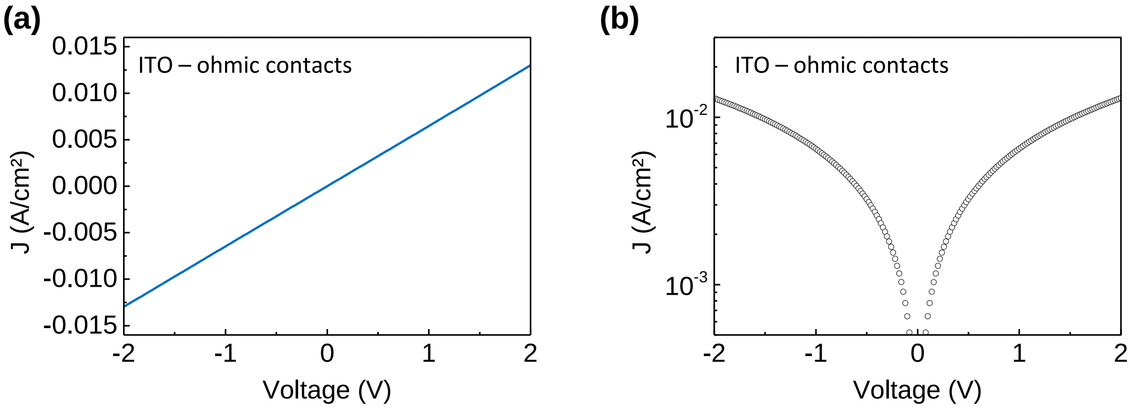

Figure 5-8: Linear (a) and semi-logarithmic (b) representation of *J*-*V* characteristic for the ZnO single crystal with ITO contacts. The linear response in (a) as well as the symmetric current response to a change in voltage polarity (b) indicates an ohmic behavior of the prepared contacts.

The linear current response of the ZnO single crystal with ITO electrodes as it can be seen in Figure 5-8 (a), indicates an ohmic character of the prepared contacts. A linear fit over the whole voltage range reveals an overall resistance of 617 Ω. Further, a Pearson correlation coefficient of 1 implies a perfect linear correlation between voltage and current. In addition, the current response is independent on the applied voltage polarity (see Figure 5-8 (b)). Hence, a successful formation of an ohmic contact between ITO and ZnO can be verified. Since the screening mechanism is believed to correlate with the free charge carrier density, which in turn is a function of temperature, temperature-dependent impedance measurements were performed between -120 °C and room temperature (20 °C). Figure 5-9 depicts the Bode representation of the real part of impedance as a function of temperature.

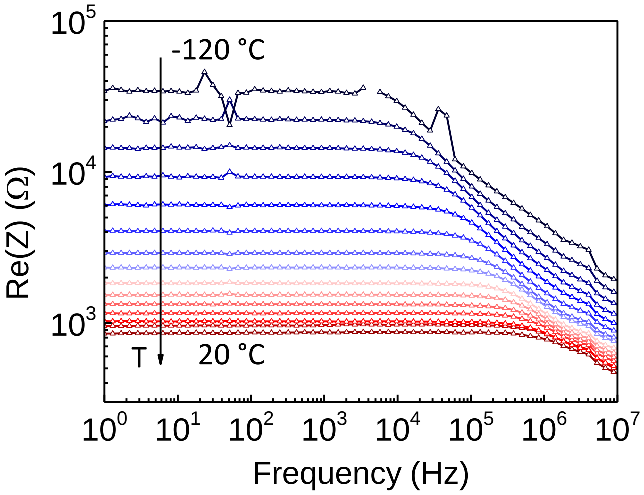

Figure 5-9: Bode representation of the real part of impedance for the ZnO single crystal with ohmic ITO contacts between -120 °C and 20 °C in steps of 10 °C.

The spectroscopic plot of the real part of impedance for the ZnO single crystal with ohmic contacts at room temperature shows a frequency-independent behavior over a large frequency range. The value of resistance in this low frequency regime is with around 850 Ω in the range of the determined value from the *J-V* measurement. Therefore, the process is attributed to the conduction process of the bulk ZnO. With decreasing temperature, the real part of resistance at low frequencies continuously increases from ~850 Ω at +20 °C to ~35 $k\Omega$ at -120 °C. In semiconductors, the temperature dependence of resistance is mainly determined by thermal activation of charge carriers.[209] Hence, the increasing resistance with decreasing temperature in ZnO can be attributed to a decreasing free charge carrier concentration. The temperature-dependent electrical conductivity ($\sigma_{el}(T)$) for an n-type semiconductor can be expressed as a function of free electron concentration (n_e) and electron mobility (μ_n):

$$\sigma_{el}(T) = q \cdot \mu_n(T) \cdot n_e(T)\,, \tag{5.10}$$

with n_e and μ_n being temperature-dependent values. From the temperature-dependent resistance values and $\mu_n(T)$ taken from literature[205], $n_e(T)$ can be calculated. Figure 5-10 depicts the determined resistance as well as the therefrom calculated free charge carrier concentration (n_e).

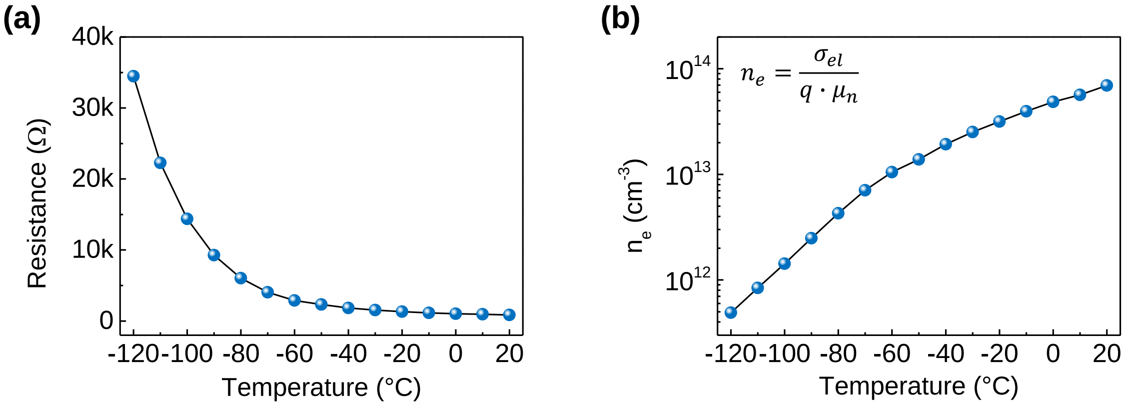

Figure 5-10: (a) Temperature-dependent low frequency resistance of the ZnO single crystal with ITO electrodes between -120 °C and 20 °C. (b) Free charge carrier concentration calculated from the low frequency resistance.

The temperature-dependent charge carrier concentration is calculated to decrease by more than two orders of magnitude from $7 \cdot 10^{13}\ cm^{-3}$ at 20 °C to about $5 \cdot 10^{11}\ cm^{-3}$ at -120 °C. The profound decrease in n_e with decreasing temperature should lead to a reduced screening of the piezoelectric charges and hence a better performance of the device in piezotronic applications. The correlation between temperature and piezotronic performance has already been discussed in literature.[130, 210, 211]

To study the impact of a reduced free charge carrier concentration on the attainable piezoelectric properties, a modified Sawyer-Tower setup was used to measure the piezoelectric coefficient of the ZnO single crystal with ohmic ITO contacts between -120 °C and 20 °C. In addition, the excitation frequency was varied between 1 Hz and 160 Hz to examine a possible frequency dependence of the screening effect. The results of the piezoelectric measurement are depicted in Figure 5-11.

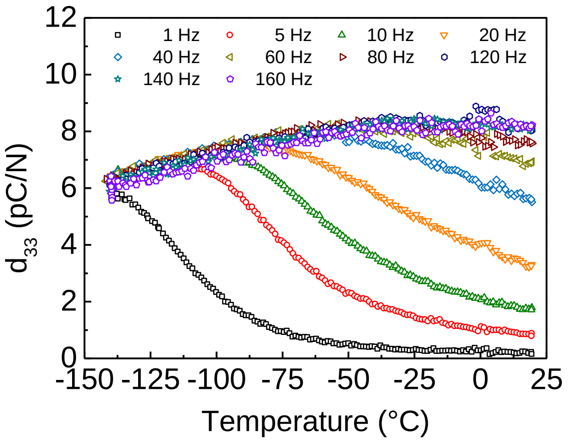

Figure 5-11: Experimentally determined temperature profiles of the piezoelectric coefficient (d_{33}) of a ZnO single crystal with ITO – ohmic contacts for different loading frequencies between 1 Hz and 160 Hz.

Two general trends are obtained from the d_{33} temperature profiles for different loading frequencies as depicted in Figure 5-11. By decreasing the temperature or increasing the loading frequency, the measured d_{33} can be increased. For low temperatures and high loading frequencies, this correlation does not hold, which will be explained within this section at a later stage. However, for low loading frequencies ($\leq$ 5 Hz) the piezoelectric coefficient is almost zero at room temperature. Only when the temperature is decreased, a significant d_{33} value can be measured. For the 1 Hz measurement, d_{33} starts to increase at a temperature of $\sim$-50 °C. At -140 °C a piezoelectric coefficient of almost 6 pC/N can be captured. Since, with decreasing temperature, the free charge carrier concentration within the ZnO is reduced (see Figure 5-10), the obtained increase in d_{33} is most likely being related to reduced screening of the piezoelectric polarization.

By increasing the loading frequency to 5 Hz, the temperature, at which d_{33} starts to increase can be shifted to higher temperatures. When the loading frequency is further increased, a piezoelectric signal can be already measured at room temperature. At 80 Hz, a piezoelectric coefficient of 7.6 pC/N can be captured at 20 °C. A further increase in loading frequency does not lead to a notable additional increase in d_{33}. In ferroelectric materials, a frequency dependence of the piezoelectric effect was mainly attributed to interactions between moving domain walls and defects.[212] Due to the fact, that ZnO does not possess a domain structure, this mechanism cannot rationalize the frequency-dependent piezoelectric response of ZnO single crystals. Therefore, a closer look has to be taken to the interaction between the temperature-dependent electrical properties of ZnO and the measurement procedure.

An equivalent circuit is proposed, from which the temperature- and frequency-dependent d_{33} response shall be calculated. Figure 5-12 represents the utilized equivalent circuit. The piezoelectric ZnO single crystal is modeled as a charge source, inducing an ac-current (I_{Piezo}), with the frequency of the mechanical excitation. The current splits up into a leakage current (I_L) flowing through the leakage path and a measurement current (I_M) flowing through the measurement branch. The stress-induced current flow I_{Piezo} should be proportional to the theoretical piezoelectric coefficient, which is defined by the crystal structure and bond character of ZnO. On the other hand, the measured d_{33} value is determined from the charge captured on the reference capacitor, which in turn is defined by I_M. The difference between I_M and I_{Piezo} is equal to the leakage current I_L, which accounts for internal charge compensation within the ZnO single crystal. For an ideal piezoelectric insulator, the resistance of the leakage path would be infinite and hence, the charge on the reference capacitor would equal the generated piezoelectric charge. This is not the case for a piezoelectric material with lower internal resistance. In this case, the charge captured on the reference capacitor is not equal to the generated piezoelectric charge but represents an effective piezoelectric charge corrected for internal losses. The effective piezoelectric coefficient can be calculated by taking the ratio between the measurement current, I_M, flowing through C_{Ref} and the generated current I_{Piezo}.

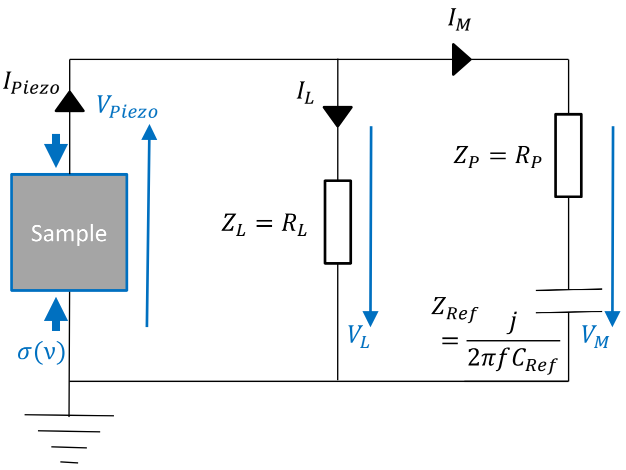

Figure 5-12: Equivalent circuit used to calculate the piezoelectric response. The ZnO single crystal can be modeled as source of current, which splits up between the leakage branch and the measurement branch according to the corresponding impedance values.

To simulate the effective piezoelectric coefficient, the complex current flow through the equivalent circuit is calculated. The ratio between I_L and I_M is defined by the impedance of the leakage path (Z_L) as well as the impedance of the measurement path (Z_M). Z_L is solely defined by the resistance of the bulk ZnO single crystal as shown in Figure 5-10 (a), which here will be referred to as R_L:

$$Z_L = R_L\,. \tag{5.11}$$

Z_M on the other hand, is composed of the impedance of the parasitic resistance ($Z_P = R_P$) and the impedance of the reference capacitor ($Z_{Ref} = (j\omega C_{Ref})^{-1}$), which are connected in series:

$$Z_M = \sqrt{Z_P^2 + Z_{Ref}^2} = \sqrt{R_P^2 + \left(\frac{1}{j\omega C_{Ref}}\right)^2}\,. \tag{5.12}$$

Since Z_L is directly proportional to R_L, which in turn is highly sensitive to temperature, the temperature-dependent behavior of the effective piezoelectric coefficient can be explained by the increasing impedance of the leakage path with decreasing temperature. The observed frequency dependence can be rationalized by the reference capacitance, since its impedance is a function of frequency. From equations 5.11 and 5.12 the temperature-dependent evolution of the effective piezoelectric coefficient can be simulated. R_L as a function of temperature is known from the temperature-dependent impedance measurements and the excitation frequency defines $\omega = 2\pi\nu$ and by this the evolution of Z_{Ref} as a function of frequency. The reference capacitance is defined by the setup ($C_{Ref} = 4.6\ \mu F$). The only unknown needed to calculate the full piezoelectric response is the value of the parasitic resistance (R_P). Therefore, different assumptions were made for R_P to simulate the overall piezoelectric response as a function of temperature and frequency. The results are depicted in Figure 5-13 (a)-(c).

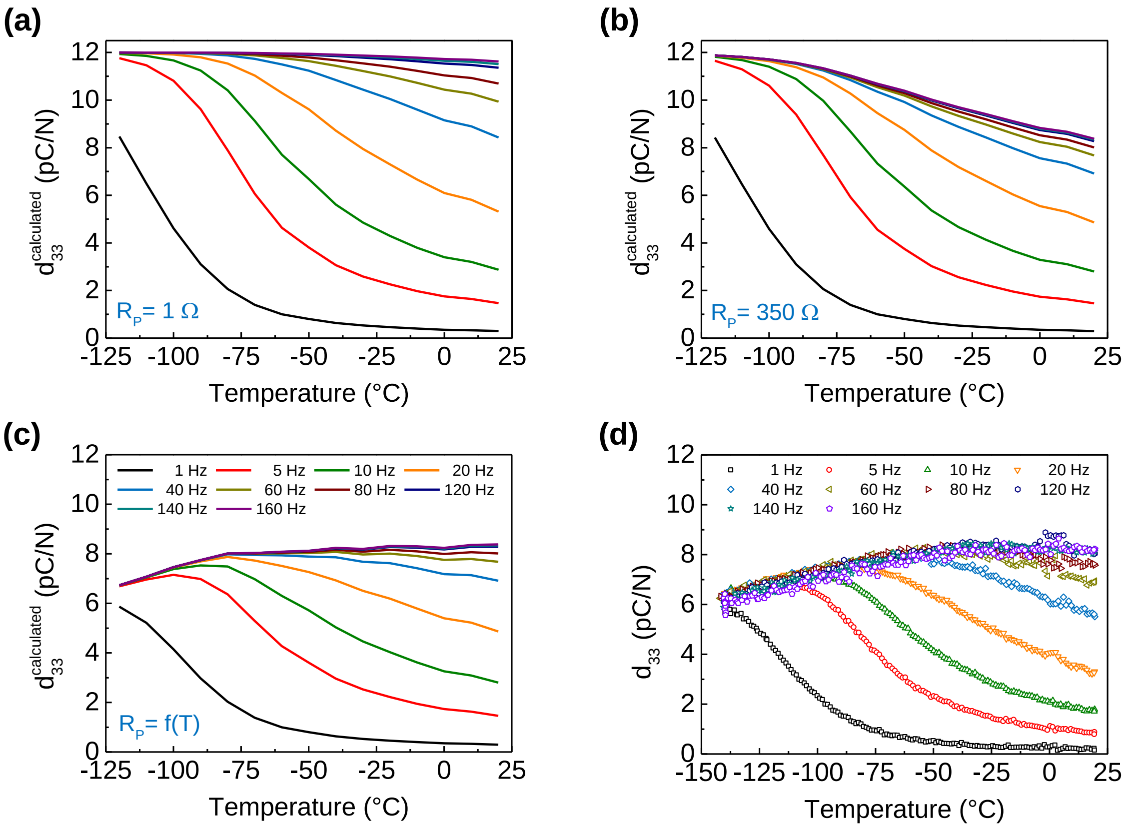

Figure 5-13: Temperature profiles of the calculated effective piezoelectric coefficient for different loading frequencies. Different assumptions were made for the parasitic resistance R_P, with (a) $R_P = 1\,\Omega$, (b) $R_P = 350\,\Omega$, and (c) R_P is a function of temperature, where R_P increases from 350 Ω at room temperature to 27000 Ω at -120 °C. For comparison, (d) again depicts the measured piezoelectric response.

In general, a parasitic resistance is introduced to account for the resistive contributions from connecting wires and its contacts between the sample and the measurement setup, or in this case, the reference capacitor. In an ideal system, R_P should be as low as possible. This case is simulated with a value of $R_P = 1\,\Omega$. The results of the calculation are depicted in Figure 5-13 (a). With $R_P = 1\,\Omega$, the calculation already features the main findings of the experimental data: (1) at low loading frequencies (≤ 5 Hz), almost no piezoelectric response is obtained at 20 °C, while d_{33} increases with decreasing temperature, and (2) with increasing loading frequency, d_{33} increases already at room temperature. These key findings can be explained by the temperature dependence of Z_L and the frequency dependence of Z_M, respectively. For example, at room temperature and 1 Hz loading frequency, $Z_M = 35\,k\Omega$ whereas $Z_L = 850\,\Omega$. Since $Z_L \ll Z_M$, the major part of the piezoelectric current flows as I_L through the leakage branch and is hence compensated within the sample. Almost no charge is captured on the reference capacitor and therefore, no effective piezoelectric coefficient is obtained. With decreasing temperature, Z_L increases to $34\,k\Omega$ while Z_M is not affected by temperature.

Therefore a noticeable amount of current flows towards the reference capacitor which is reflected in the increasing effective piezoelectric coefficient measured on the reference capacitor. Now, when the temperature is fixed at room temperature and only the loading frequency is increased, $Z_L = 850\,\Omega$ is frequency-independent while Z_M decreases from 35 $k\Omega$ at 1 Hz to 216 Ω at 160 Hz. Even with the impedance of the leakage path staying comparably small, the dramatic decrease in impedance of the measurement branch results in a profound measurement current flowing towards the reference capacitor and hence a measurable effective piezoelectric coefficient. However, certain features of the experimental data cannot be emulated with the low value of R_P. The first discrepancy occurs at room temperature and increasing frequency. The experimentally determined piezoelectric coefficient saturates for loading frequencies of 80 Hz and higher. The saturation of d_{33} can be accounted for by increasing the parasitic resistance, such that R_P dominates Z_M at higher loading frequencies. With the assumption of $Z_P = 350\,\Omega$, the experimentally observed saturation of d_{33} at room temperature can be simulated with good agreement (see Figure 5-13 (b) and (d)). The most obscure feature of the experimental data is the decreasing value of d_{33} for higher loading frequencies and decreasing temperature. This behavior is in contradiction to the general assumption of an increasing Z_L with decreasing temperature and a decreasing Z_M with increasing loading frequency and cannot be rationalized with a constant value of R_P. To reason a decreasing d_{33} with lowering temperature for the measurements at higher loading frequencies, R_P needs to be considered to increase with decreasing temperature. As stated before, at loading frequencies of 80 Hz or higher, Z_M is dominated by R_P, which explains the disappearing frequency dependence of d_{33}. Under the assumption that R_P increases with decreasing temperature, the current flow towards the reference capacitor is lowered, leading to a decreasing trend of d_{33}. With R_P increasing in an exponential fashion from $350\,\Omega$ at 20 °C to $R_P = 27\,k\Omega$ at -120 °C, the experimental data can be simulated with good agreement. Despite the fact that no physical origin of the temperature dependence of R_P can be given at the moment, the conducted simulations with different assumptions for R_P corroborate the key findings of the temperature- and frequency-dependent d_{33} measurements of piezoelectric ZnO single crystals.

From the increasing piezoelectric response with decreasing temperature it is evident, that a reduced free charge carrier concentration impedes the internal screening of the piezoelectric potential. Therefore, it is believed, that the reduced free charge carrier density in the vicinity of a Schottky contact, can allow a piezoelectric response at room temperature and low loading frequencies, even for highly conductive ZnO.

5.2.2. Piezoelectric measurements on a ZnO single crystal with Schottky contact

To study the influence of a highly resistive depletion layer on the attainable piezoelectric coefficient in ZnO, an Ag-based Schottky contact was deposited on the Zn-terminated surface of a bulk ZnO single crystal. Figure 5-14 depicts the linear (a) and semi-logarithmic (b) representation of the performed *J*-*V* measurement.

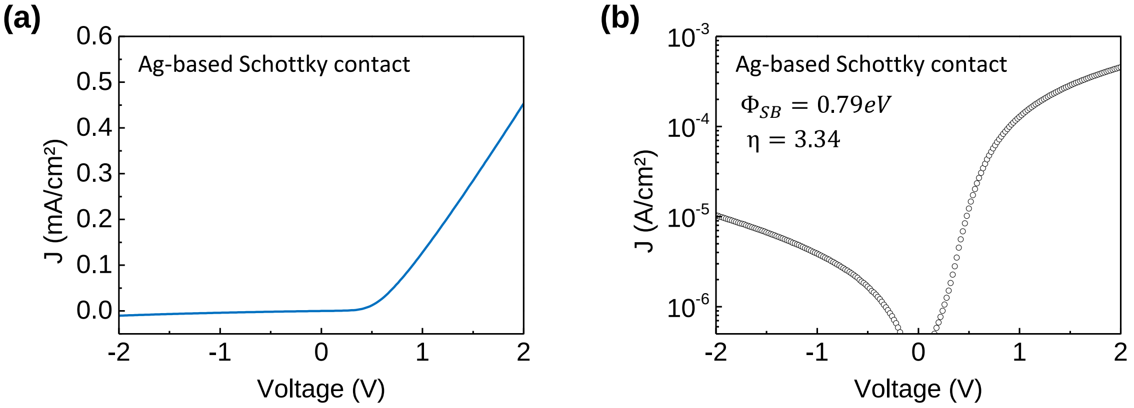

Figure 5-14: Linear (a) and semi-logarithmic (b) representation of *J*-*V* characteristic for the ZnO single crystal with an Ag-based Schottky contact on the Zn-terminated surface. The nonlinear *J*-*V* curve in (a) as well as the polarity dependence in (b) confirm the successful preparation of a rectifying Schottky contact.

The asymmetric current response as depicted in Figure 5-14 (a) and (b) confirms the successful preparation of a rectifying Schottky contact. The potential barrier height is determined from the linear part of the forward biased current density response. In addition, the ideality factor is calculated. The procedure was already described in chapter 5.1.1. A potential barrier height of $\Phi_{SB} = 0.79\ eV$ and the ideality factor of $\eta = 3.34$ are in agreement with the results determined for Ag-based Schottky contacts in chapter 5.1.1 and are in accordance with values reported in literature.[195] Therefore, it can be assumed that a Schottky barrier with concurrent formation of a depletion region is formed in the vicinity of the Ag-based electrode. Like for the ohmic contact, the piezoelectric response of the ZnO single crystal with Schottky contact shall be measured as a function of temperature. Hence, impedance measurements were performed with decreasing temperature to determine the change in resistance. Figure 5-15 features the Bode representation of the real part of impedance between -100 °C and room temperature (20 °C).

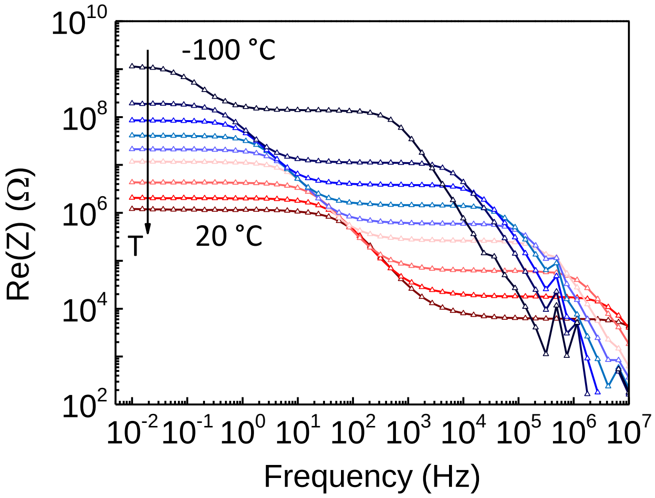

Figure 5-15: Bode representation of the real part of impedance for the ZnO single crystal with Schottky contact on the Zn-terminated surface between -100 °C and 20 °C in steps of 10 °C or 20 °C, respectively.

Compared to the impedance response of the ZnO single crystal with ITO electrodes, the impedance response of the ZnO single crystal with Schottky contact is more complex. At least two processes are visible in the spectroscopic representation of the real part of impedance (see Figure 5-15). The low frequency process may be attributed to the electrical transport properties of the Schottky contact, while the high frequency process may arise from the response of the bulk or the ohmic contact on the opposite side of the crystal. Still, the overall dc resistance seems to be dominated by the resistance of the Schottky contact. The resistance value of the low frequency plateau increases from $\sim 1\ M\Omega$ at 20 °C to more than $1\ G\Omega$ when the temperature is reduced to -100 °C. Like observed for the crystal with ohmic contacts, the temperature induced increase in overall resistivity should profoundly increase the attainable piezoelectric charges. The piezoelectric response of the ZnO single crystal with Schottky contact was investigated as a function of temperature for different measurement frequencies. The procedure was similar to the d_{33} measurement conducted for the crystal with ohmic contacts. In addition, the transversal piezoelectric coefficient (d_{31}) was also measured for the crystal with Schottky contact on the Zn-terminated surface. Figure 5-16 displays the piezoelectric response in d_{33} (a) as well as d_{31} (b) arrangement.

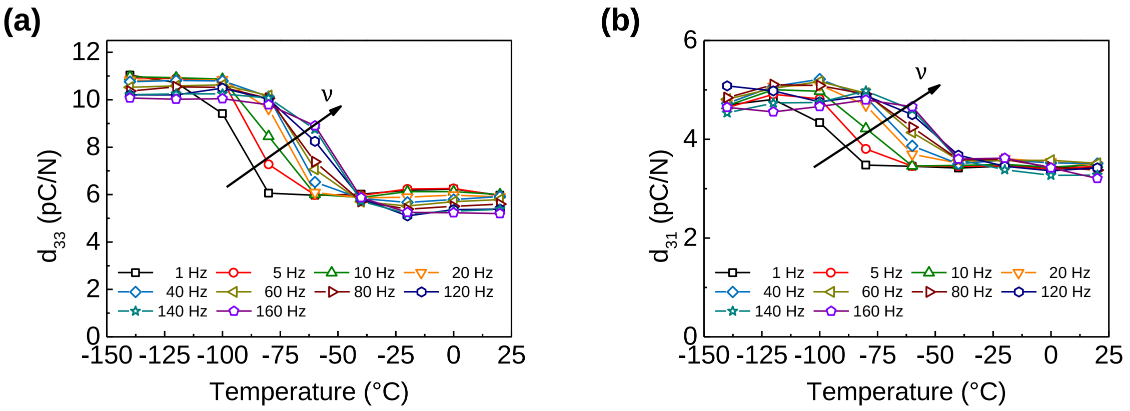

Figure 5-16: Experimentally determined longitudinal (a) and transversal (b) piezoelectric coefficient, d_{33} and d_{31} of the ZnO single crystal with Schottky contact on the Zn-terminated surface as a function of temperature for different loading frequencies.

Figure 5-16 (a) features the temperature profiles of the effective piezoelectric coefficient measured in longitudinal arrangement (d_{33}) for the ZnO single crystal with Schottky contact. Even at room temperature (20 °C) a piezoelectric response of almost half the theoretical value can be detected already for low loading frequencies. In comparison to the response of the crystal with ohmic contacts the piezoelectric output of the ZnO with Schottky contact at low frequencies is significantly higher. This can be rationalized by the higher overall resistance of the sample due to the formation of a depletion layer in the vicinity of the Schottky contact. By a reduction in leakage current, the charge flowing towards the reference capacitor can be significantly increased. With decreasing temperature, the overall resistance can be further increased as demonstrated by temperature-dependent impedance measurements (see Figure 5-15). Therefore, the effective piezoelectric coefficient which can be measured increases with decreasing temperature. At -140 °C and 1 Hz loading frequency, a piezoelectric coefficient of around 11 pC/N can be determined. By increasing the loading frequency, the temperature at which d_{33} starts to increase can be shifted to higher values. The increasing piezoelectric response with decreasing temperature and the frequency-dependent shift in temperature where d_{33} starts to increase is in accordance with the behavior of the ZnO crystal with ohmic contacts. Hence, the same physical mechanisms as described in chapter 5.2.1 may apply. However, significant distinctions between the ZnO crystals with ohmic and Schottky contact arise. For the sample with Schottky contact, no profound frequency dependence is observed at room temperature. On the other hand, the ZnO crystal with ohmic contacts features a profound increase in d_{33} at room temperature with increasing loading frequency. This increase could be well rationalized by the frequency-dependent impedance of the measurement branch.

In the case of the ohmic contact, the whole sample could be represented by one purely resistive component within the equivalent circuit. This may not be a reasonable assumption for the sample with Schottky contact. Due to the formation of a potential barrier and depletion layer, significant capacitive contributions arise and therefore would need to be considered within an equivalent circuit applicable to calculate the overall piezoelectric response (see Figure 5-5). Additional capacitive contribution would add further frequency-dependent impedance components to the sample and may account for the insensitivity toward excitation frequency by compensating the frequency dependence of the reference capacitor. This highly complicates a possible simulation of the piezoelectric response with the need to make additional assumption. Therefore, no calculations are presented for the ZnO single crystal with Schottky contact.

To check the validity of the d_{33} measurement, an additional measurement was performed in d_{31} arrangement. Since the theoretical value of d_{31} is almost half the d_{33} value, this ratio should reflect itself in the measurement. The corresponding temperature profiles of the effective piezoelectric coefficient measured in transversal arrangement (d_{31}) for the ZnO single crystal with Schottky contact are depicted in Figure 5-16 (b). At room temperature, a d_{31} value of around 3 pC/N is obtained which is about half the theoretical value. With decreasing temperature, the d_{31} value increases to around 5 pC/N. Compared to the d_{33} measurement, the temperature- and frequency-dependent evolution of d_{31} features the same behavior. Again, an increase in piezoelectric response with decreasing temperature can be observed. Also, a shift in temperature at which d_{31} starts to increase can be rendered with increasing the loading frequency. Hence the d_{31} measurement confirms the results obtained in d_{33} arrangement.

To visualize the influence of the highly resistive depletion layer on the attainable piezoelectric output of ZnO single crystals, the voltage drop of the ZnO single crystal with Schottky contact is compared to that of the ZnO single crystal with ohmic ITO electrodes at an excitation frequency of 1 Hz and at room temperature (Figure 5-17). The ZnO single crystal with ohmic ITO contacts does not generate a voltage output which can be captured in the reference capacitor. In contrast, for the ZnO single crystal with ohmic ITO electrodes the voltage signal captured on C_{Ref} follows the applied load profile with a phase difference of 180°. Regarding possible applications in the field of energy harvesting, it is nicely demonstrated, that the formation of a highly resistive depletion layer can prevent the piezoelectric potential from screening mechanisms due to free charge carriers. Thereby the operational temperature can be shifted to room temperature and lower loading frequencies. The ability to harvest energy at low loading frequencies is of particular importance since most of the potential ambient power sources are "low-level" vibrations.[213, 214]

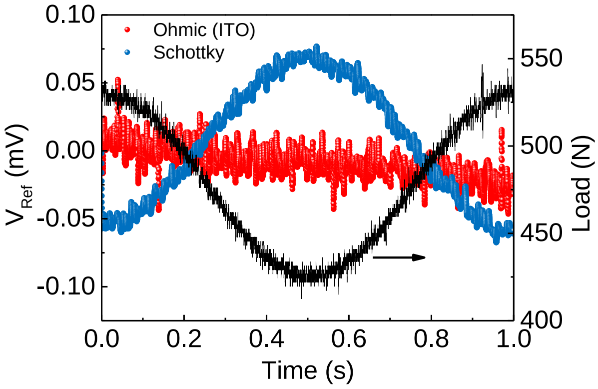

Figure 5-17: Comparison of the voltage drop on the reference capacitor for the ZnO single crystals with ITO and Schottky contact at room temperature and an excitation frequency of 1 Hz.

5.2.3. Summary – Piezoelectric measurements

The influence of free charge carrier concentration on the attainable piezoelectric charge was studied using ZnO single crystals with either an ohmic or a rectifying Schottky contact. It is found, that the formation of a highly resistive depletion layer in the vicinity of the Schottky contact can significantly enhance the attainable piezoelectric coefficient. Regarding piezotronic and energy harvesting applications, the existence of a depletion region can shift the operational temperature to room temperature. Furthermore, the excitation frequency can be reduced, broadening the operational range of energy harvesters based on piezotronic devices. A simple analytical model was used to underpin the temperature- and frequency-dependent behavior of the piezoelectric response. A complex interaction between internal charge compensation and the impedance response of the readout circuit is found. The findings in this chapter are of importance for energy harvesting applications based on ZnO, a field which gained huge interest during the last decade.[215-217] Since dynamic interaction between electrode properties and piezoelectric response are crucial for the device performance the above elucidated physical mechanisms may help to improve future devices.

5.3. Piezotronic effect of ZnO bicrystals

Like piezoelectric polarization charges can tune the electrical transport properties across metal-ZnO Schottky contacts, in polycrystalline ZnO varistor ceramics, mechanical stress can modulate the height of potential barriers at the grain boundaries of the ceramic. For piezotronic devices based on Schottky contacts, the attainable change in potential barrier height is rather small, with reports being in the range of milli-electron volts at room temperature and comparably high mechanical strain.[37, 130, 218] As described in chapter 5.1, the moderate change in Schottky barrier height can be primarily attributed to the small spatial separation between piezoelectric charges and screening charges within the metal electrode. Therefore, doped ZnO-ZnO interfaces as they are present at the grain boundaries of polycrystalline varistor ceramics may represent a viable system for next generation piezotronic devices. In polycrystalline varistor ceramics, the conductivity could already be changed by orders of magnitude under the application of mechanical stress.[26, 165, 219] Due to the polycrystalline nature of the varistor ceramic, a multitude of randomly orientated grains and grain boundaries are connected in series and parallel, preventing device design with precise control over electrical properties. Therefore, piezotronic devices based on polycrystalline varistor ceramics often require high operating voltages. In this chapter, an approach will be presented, where the chemistry of a varistor grain boundary is inserted into an individual ZnO bicrystal interface with control over the polarization vector orientation. By optimal polarization vector alignment, stress-induced piezoelectric polarization charges at the interface can be maximized. In the first part of this section (chapter 5.3.1) a preparation process based on epitaxial solid-state transformation will be presented, resulting in individual varistor type bicrystal interfaces with either head-to-head or tail-to-tail orientation of the polarization axis. In chapter 5.3.2, the application of mechanical stress affords either a reduction or an increase in potential barrier height, depending on the interface orientation. Furthermore, the stress sensitivity of the piezotronic effect in ZnO bicrystals will be evaluated and compared to that of metal-ZnO Schottky contacts. Parts of the here presented data have been previously published as an article in Advanced Materials.[220]

5.3.1. Preparation of ZnO bicrystal interfaces by epitaxial solid-state transformation

To prepare individual bicrystal interfaces, epitaxial solid-state transformation of a polycrystalline sacrificial layer in between two well oriented ZnO single crystals was applied (see Figure 4-3).[191] The orientation of the single crystals was chosen, such that under the application of a mechanical compressive stress, the ensuing polarization vectors are either in head-to-head orientation (O|O-interface) or tail-to-tail orientation (Zn|Zn-interface). A schematic of the orientation relationship can be found in Figure 2-13 (a) and (c).

Structural characterization

After a two-step temperature treatment consisting of a diffusion bonding step and high temperature annealing, individual bicrystal interfaces can be observed (see Figure 5-18 (a)). During the high temperature annealing step, grain growth as well as epitaxial growth of the ZnO single crystal into the polycrystalline sacrificial layer occurs. Due to the different growth rates of the ZnO single crystals in different direction, the time of the high temperature treatment was adjusted. Growth rate in the Zn-direction is much faster compared to the O-direction.[221] Hence, annealing time of 65 h at 1100 °C for the O|O-interface and 25 h at 1100 °C for the Zn|Zn-interface revealed the desired bicrystal structure. The prepared bicrystal structures feature a single interface over a large area but in some parts, individual grains or small amounts of remaining polycrystalline material are still present (see Figure A-1). However, the overall electrical properties should be dominated by the individual bicrystal interface. If a potential barrier is assumed to be present at every ZnO-ZnO interface or grain boundary, the current will flow through the areas with lowest number of potential barriers connected in series. Transmission electron microscopy (TEM) studies of the O|O – interface were conducted to see whether the interface is free from any intergranular layer as reported for previous preparation techniques of varistor type bicrystals.[181] From the bright field TEM images as shown in Figure 5-18 (b), the bicrystal interface prepared by epitaxial solid-state transformation is free from an intergranular phase. Furthermore, it is proven, that the defined crystallographic orientation of the single crystals is maintained during epitaxial growth into the polycrystalline sacrificial layer (see insets in Figure 5-18 (c)). A small twist and tilt angle of below 1° was determined as misfit between the two adjacent single crystals. The small misfit is compensated by misfit dislocations introduced at the boundary. The strain fields generated by misfit dislocations can be seen from the contrast variations present in Figure 5-18 (c). In addition, high-angle annular dark field (HAADF) images were taken at the grain boundary. Since in HAADF images, only incoherently scattered electrons are used to form the image, the intensity is highly proportional to the square of the atomic number (Z^2). Even with the less-than-ideal resolution, bright spots can be detected in the center of the image where the interface is known to be positioned. Since bismuth is the only element in the used composition with a higher atomic number than zinc, the higher contrast at the interface highly indicates that bismuth is localized at the interface. The findings can be verified by energy-dispersive X-ray spectroscopy (EDS) analysis, performed in the scanning TEM (see Figure A-2). Only at the interface, bismuth is detected, while the bismuth peak is absent in the bulk material. Other dopants like Cr, Mn, Co and Ni are present at the boundary as well as within the bulk material. The findings are in agreement with literature, where large sized ions like Bi and Pr are known to be favorably present at the grain boundaries, while they are virtually insoluble in the ZnO lattice.[222] [223]

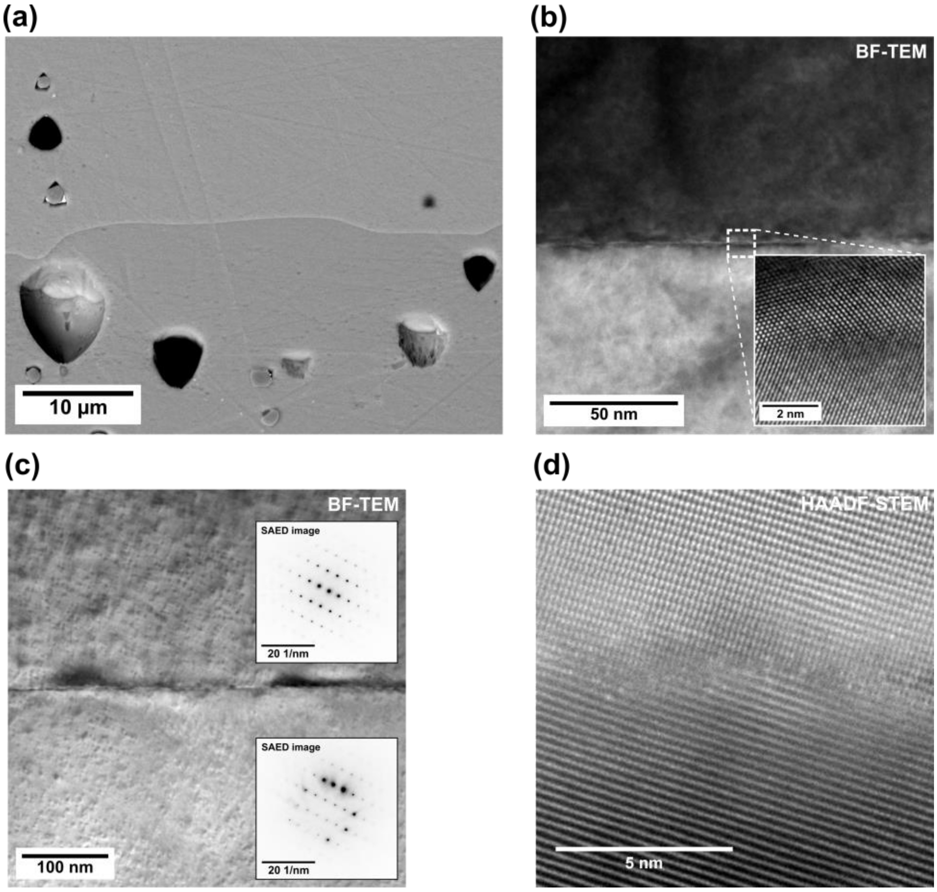

Figure 5-18: Structural analysis of O|O bicrystal interface prepared by epitaxial solid-state transformation. (a) Scanning electron microscopy (SEM) image of the individual bicrystal interface obtained in backscatter electron (BSE) mode. (b) Bright field TEM image of the interface, proving the absence of an intergranular layer. (c) Bright field TEM image of the interface in two-beam condition. The two insets depict selected area electron diffraction images (SAED), from which a twist/tilt misfit of around 1° can be determined. (d) High-angular annular dark-field imaging (HAADF)-STEM image of the bicrystal interface, with the bright spots indicating the presence of bismuth atoms at the boundary.

Electrical characterization

The purpose of the epitaxial growth of single crystals into a polycrystalline sacrificial layer of a typical ZnO varistor composition was to create individual ZnO-ZnO interfaces which mimic the electrical properties of single grain boundaries of a varistor ceramic. The chemical composition at the ensuing interface as discussed in the previous section should result in the formation of an electrostatic potential barrier with highly nonlinear current-voltage characteristic. To prove the successful formation of the potential barrier, *I-V* curves of the prepared bicrystals were recorded. The results of the *I-V* measurements in stress-free condition are depicted in Figure 5-19.

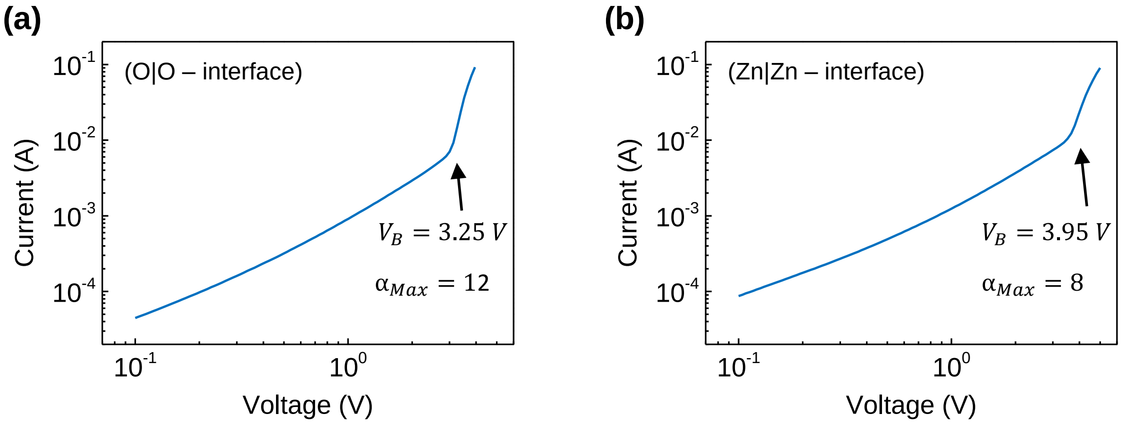

Figure 5-19: Current-voltage characteristics of the bicrystals with O|O – interface (a) and Zn|Zn – interface (b). Both bicrystals feature breakdown voltages (V_B), typical for individual grain boundaries of polycrystalline varistor ceramics.

I-V measurements confirm the successful preparation of varistor-type potential barriers at the bicrystal interfaces. Both interfaces feature a distinct breakdown voltage where a change from leakage current regime into the conductive state can be observed. This behavior is a fingerprint for the presence of a varistor-like double Schottky barrier as introduced in chapter 2.3. The breakdown voltage for the O|O – interface is with 3.25 V slightly lower than the breakdown voltage of the Zn|Zn – interface, which has a value of 3.95 V. Nevertheless, both are well in the range of reported breakdown voltages for single grain boundaries in polycrystalline varistor ceramics as measured by e.g. microprobe techniques.[162, 176] In this work, the breakdown voltage was determined as the voltage at which the coefficient of nonlinearity reveals its maximum (α_{Max}). The coefficient of nonlinearity was calculated with equation 2.25. The calculated value of α_{Max} for the O|O – interface is with a value of 12 higher compared to $\alpha_{Max} = 8$ for the Zn|Zn – interface. To further confirm, that the nonlinear current-voltage response is a consequence of the potential barrier formation due to the unique chemical composition at the interface, the *I-V* response of the bicrystals prepared by epitaxial growth is compared to the *I-V* response of an undoped ZnO bicrystal. The undoped bicrystal was prepared by diffusion bonding for 10 h in air under a slight mechanical load of 1.5 MPa. In comparison to the doped bicrystals prepared by epitaxial solid-state transformation, the undoped bicrystal does not feature any nonlinear *I-V* behavior, as depicted in Figure 5-20. Therefore, it can be concluded, that no electrostatic potential barrier is formed at the interface, which is in agreement to previous reports.[147] Furthermore, the leakage current at small applied electric fields is significantly higher in the case of the undoped bicrystal, again indicating the absence of an electrostatic potential barrier in contrast to the doped interfaces. At high electric fields, the potential barrier present at the doped interfaces of the bicrystals prepared by epitaxial solid state transformation is completely reduced and the conductivity should primarily be determined by the conductivity of the ZnO grains. In this part of the *I-V* curve, the conductivity of the doped bicrystals prepared by epitaxial growth is even higher compared to the undoped bicrystal. The higher conductivity may be attributed to the influence of the prolonged high temperature treatment on the conductivity of the ZnO single crystals.[88] The comparison with the undoped bicrystal strongly indicates, that the nonlinear current voltage response of the bicrystals prepared by epitaxial growth is a consequence of the chemical composition at the ensuing interface.

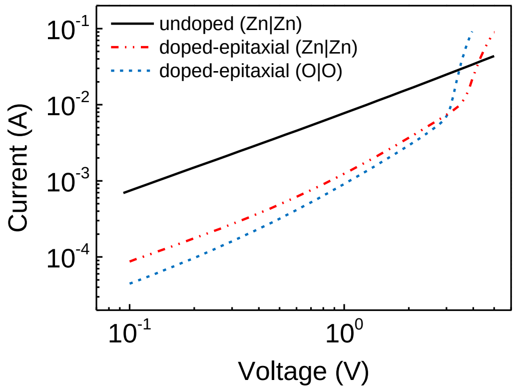

Figure 5-20: Current-voltage characteristics of the doped bicrystal prepared by epitaxial solid-state transformation and an undoped ZnO bicrystal prepared by diffusion bonding.

To confirm the results obtained by *I-V* characterization, impedance measurements were performed for the bicrystals prepared by epitaxial solid-state transformation in the stress-free state. Figure 5-21 shows the Nyquist as well as spectroscopic plots of the real and imaginary part of impedance. For both interfaces only one process can be observed which is most probably being related to the potential barrier at the interfaces.

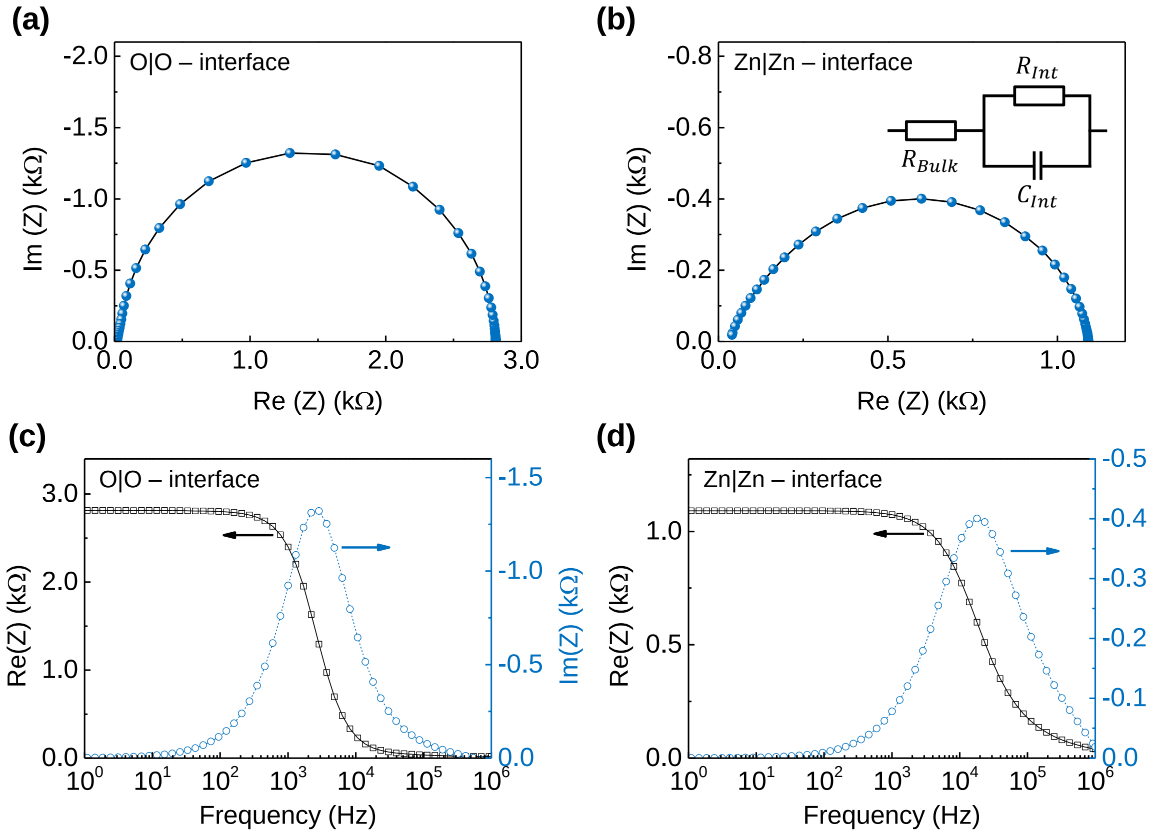

Figure 5-21: (a) Nyquist representation of the impedance measurement on the O|O – interface. (b) Nyquist representation of the impedance measurement on the Zn|Zn – interface. (c) Real and imaginary part of impedance for the O|O – interface as a function of frequency. (d) Real and imaginary part of impedance for the Zn|Zn – interface as a function of frequency.

The impedance data of both interfaces could be fitted with an RC element connected to a serial resistance (see inset in Figure 5-21 (b)). The serial resistance represents the resistivity of the singe crystalline material (R_{Bulk}) and the RC element represents the resistance of the interface (R_{Int}) and the capacity of the interface (C_{Int}). During the fitting procedure, the capacity C_{Int} was replaced by a constant phase element (CPE) to account for deviation of C_{Int} from ideal behavior. A more detailed discussion on the concept of the CPE was already given in chapter 5.1.2. From fitting, the bulk resistance for the O|O – and Zn|Zn – interfaces are determined to be 27 Ω and 50 Ω, respectively. The values of R_{Bulk} are in the same range as the resistance values determined from *I-V* measurement at voltages larger than the breakdown voltage of the potential barrier. For the interface resistance, which can be approximately determined from the DC value of the real part of impedance, R_{Int} equals 2785 Ω for the O|O – interface and 1040 Ω for the Zn|Zn – interface. The difference in R_{Int} for interfaces with changed polarity is in accordance with the higher leakage current determined for the Zn|Zn –

interface as compared to the O|O – interface (see Figure 5-20). The values of the interface capacitance are with around 30 nF and 50 nF for the O|O – and Zn|Zn – interface in the range of capacitance values reported for grain boundaries of electroceramics.[200] The results of impedance measurements strongly support the conclusion drawn from *I-V* measurements.

From structural and electrical analysis, it can be concluded that the bicrystal interfaces prepared by epitaxial solid-state transformation are in line with the electrical behavior of individual grain boundaries in polycrystalline varistor ceramics. Hence, the prepared structures are ideal systems to systematically study the influence of stress-induced piezoelectric polarization on the electrostatic potential barrier at ZnO-ZnO interfaces. The changed polarity of the interface allows to individually study the influence of positive or negative polarization charges on varistor-type electrostatic potential barriers. In the following chapter, the piezotronic modulation of conductivity across the prepared bicrystal interfaces will be discussed in detail.

5.3.2. Piezotronic modulation of conductivity across ZnO bicrystal interfaces

To study the piezotronic modulation of varistor-type ZnO bicrystal interfaces, *I-V* measurements were performed under increasing uniaxial compressive stress. Due to the direct piezoelectric effect as described by equation 2.2, the application of a mechanical stress in the c-direction of the ZnO crystals generates piezoelectric polarization charges at the bicrystal interface. For the O|O – interface, positive piezoelectric charges are generated, while for the Zn|Zn – interface, negative piezoelectric charges are expected. According to equation 2.31, positive piezoelectric charges should reduce an existing potential barrier and negative piezoelectric charges should increase an existing potential barrier. Figure 5-22 features the stress-dependent *I-V* measurements for the bicrystals with different interface polarity.

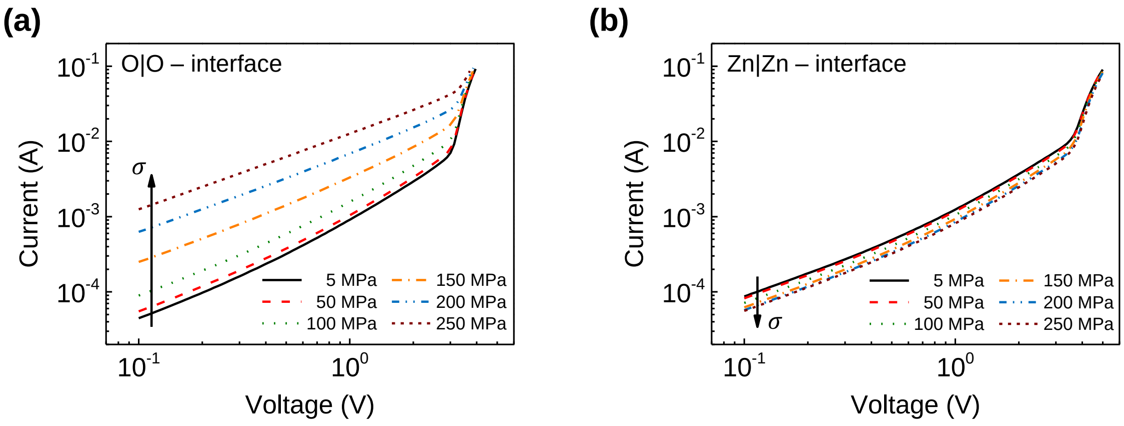

Figure 5-22: (a) Current-voltage response of the bicrystal with O|O – interface under increasing uniaxial compressive stress. (b) Current-voltage response of the bicrystal with Zn|Zn – interface under increasing uniaxial compressive stress.

As expected, for the O|O – interface and positive piezoelectric charges, an increase in electrical conductivity can be observed with increasing mechanical stress. Hence, a decrease in potential barrier height can be assumed. On the other hand, for the Zn|Zn – interface, where negative piezoelectric polarization charges are generated under compressive stress, a decrease in conductivity can be observed. The decreasing conductivity can be attributed to an increasing electrostatic potential barrier. The stress sensitivity for the different polarities are significantly different. The different stress sensitivities may be attributed to the intrinsic nature of the Fermi-level pinning phenomena which was already described for the interaction of Φ_{DSB} and applied electric field (see chapter 2.3.2) as well as mechanical stress (see chapter 2.3.3). A detailed discussion on the implications of the Fermi-level pinning on the piezotronic effect of ZnO bicrystal interfaces will follow at a later stage within this section. An unexpected feature of the stress-dependent I-V measurements is, that the breakdown voltage, V_B, is not dependent on the applied mechanical load. From the theoretical description of the charge transport across varistor-type interfaces (see chapter 2.3.2), a shift of V_B to lower voltages would be expected for a decreasing potential barrier height. The insensitivity of V_B on mechanical stress can be explained by a percolating effect across the barrier. If parts of the interface are not firmly affected by piezoelectric charge, these areas will have a constant value of V_B and therefore define the macroscopic pinning of V_B to its initial value. Areas which may be not affected by stress can be parts, where still some polycrystalline material is present between the two outer electrodes.

The fact, that by changing the interface polarity, the direction of the conductivity change can be altered is already a strong indication, that the observed effect is related to the piezotronic interaction between piezoelectric charge and electrostatic potential at the interface. Nevertheless, the reversibility of the conductivity change has to be ascertained by a second measurement in stress-free state to exclude that other mechanisms dominate the observed conductivity change.

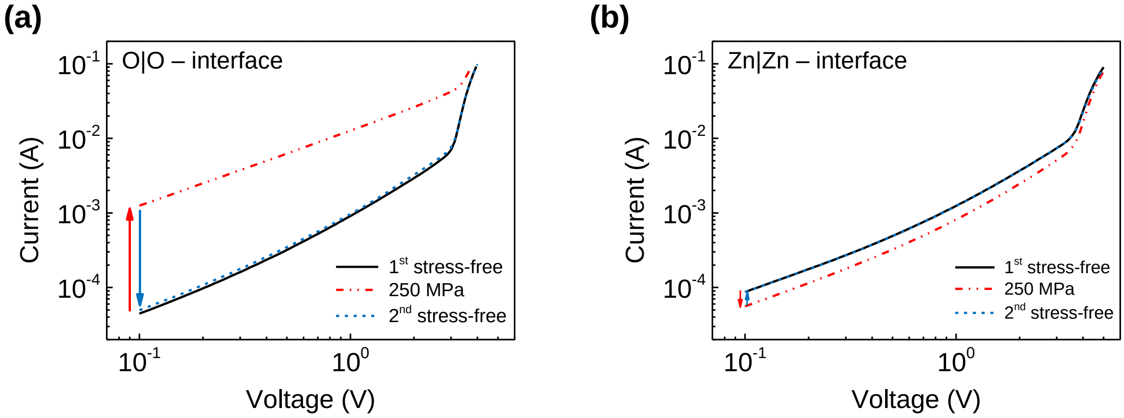

Figure 5-23: Reversibility check of the bicrystals with different polarity (a) O|O – interface and (b) Zn|Zn – interface. After stepwise increasing the stress to 250 MPa, an additional measurement is performed in the stress-free state.

As can be seen from Figure 5-23 (a) and (b), the changes in electrical conductivity are to a large extent reversible. When removing the mechanical stress, the *I-V* behavior is almost identical to the virgin curve. For the O|O – interface, only a small increase in leakage current is detectable, which may be attributed to a slight electrical degradation of the potential barrier during *I-V* measurements.[224] The reversibility together with the polarity dependence demonstrate, that the observed conductivity change is related to the interaction between stress-induced piezoelectric charge and the electronic band structure at the interface of the bicrystal.

To further quantify the piezotronic modulation of Φ_{DSB}, stress-dependent impedance measurements were performed for the bicrystals with changed polarity. From impedance data, equivalent circuit analysis can be applied to extract resistive and capacitive components of the prepared structure, as it was done for the stress-dependent modulation of a Schottky contact in chapter 5.1.2. The results obtained on the O|O – interface are depicted in Figure 5-24, while Figure 5-25 shows the results obtained on the Zn|Zn – interface.

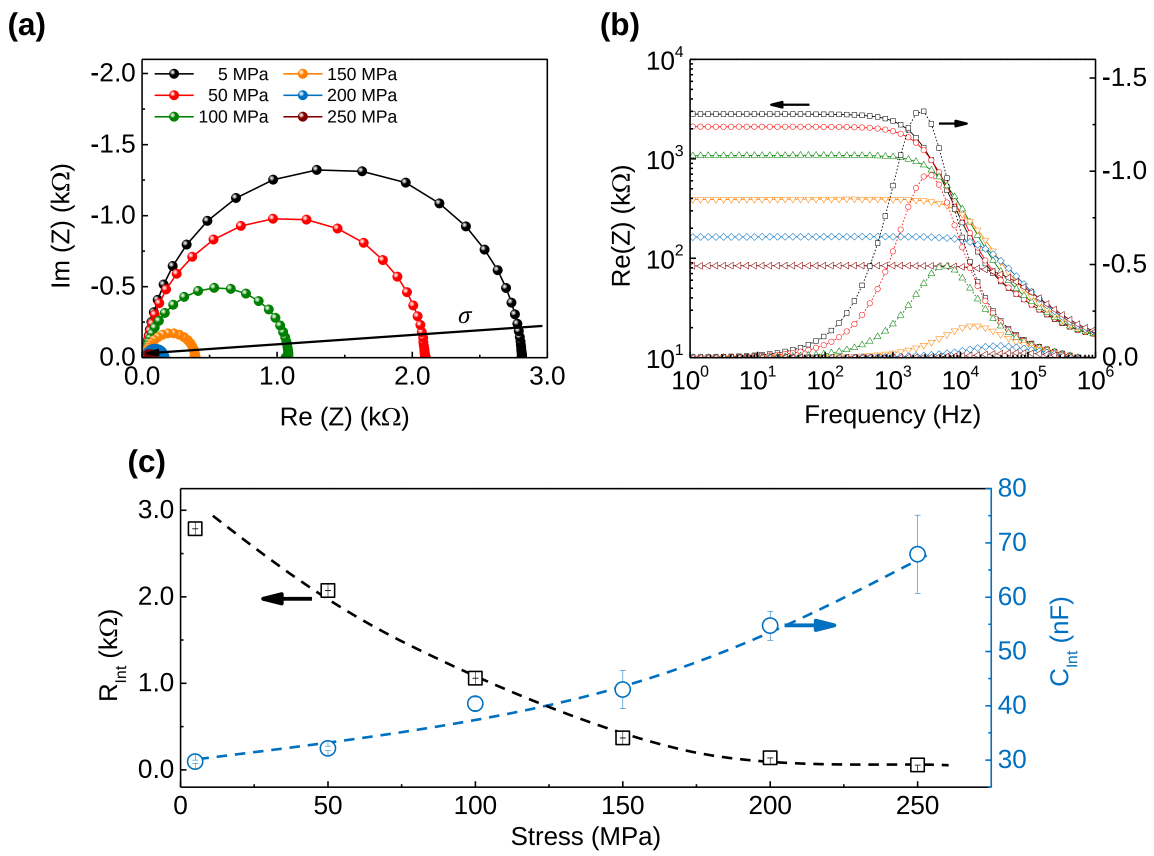

Figure 5-24: Stress-dependent impedance measurement of the bicrystal with O|O – interface. (a) Nyquist representation, (b) Spectroscopic plot of real and imaginary part of impedance, and (c) Extracted values of interface resistance and capacitance as a function of increasing uniaxial compressive stress.

In consistence with the stress-dependent *I-V* measurements, a decrease in DC resistance can be seen in the Nyquist and spectroscopic plot of the stress-dependent impedance data for the O|O – interface. The expected decrease in potential barrier height due to the generation of positive piezoelectric charges reflects itself in the decrease of the DC resistance. To extract the interface resistance (R_{Int}) and capacitance (C_{Int}), an analysis based on the equivalent circuit depicted in Figure 5-21 (a) can be applied. The results are shown in Figure 5-24 (c). The interface resistance decreases from 2785 *Ω* at 5 MPa to 56 *Ω* at an applied mechanical load of 250 MPa. With slight deviation, the general trend of R_{Int} with increasing mechanical stress agrees well with the stress-dependent resistance values of the leakage current regime (at 0.1 V) obtained by *I-V* measurements (Figure 5-22 (a)). Since the interface resistance at 250 MPa is already in the range of the bulk resistance, an almost complete reduction of the electrostatic potential barrier can be assumed already.

The decreasing interface resistance is accompanied by an increase in interface capacitance. The interface capacitance increases from 30 nF at 5 MPa to 68 nF at an applied mechanical load of

250 MPa. For all measurements, the CPE exponent (α_{CPE}) was above 0.95, indicating almost ideal capacitive behavior. The capacitance of a charged grain boundary in an n-type semiconductor and with this, the capacitance of a double Schottky barrier at a doped ZnO-ZnO interface is given by:[225-227]

$$C = \frac{\varepsilon_r \varepsilon_0}{2W_D} = \sqrt{\frac{q\varepsilon_r \varepsilon_0 N_D}{8\Phi_{DSB}}}. \tag{5.13}$$

From **equation 5.13**, the observed increase in capacitance with increasing mechanical stress can be rationalized. Stress-induced positive piezoelectric charges compensate negative interface charges. Since the negative interface charge has to be the same as the positively charged donor states within the depletion region (W_D), a reduction in interface charge has to be accompanied with a reduction in W_D. Hence, the capacitance of the interface (C_{Int}) increases.

According to equation 5.13 and therefrom, equation 5.14, the double Schottky barrier height and the depletion width are correlated by:

$$\Phi_{DSB} = \frac{qN_D W_D^2}{2\varepsilon_r \varepsilon_0}. \tag{5.14}$$

Therefore, the observed increase in C_{Int} confirms the expected decrease in potential barrier height due to the generation of positive piezoelectric polarization charges.

In contrast to R_{Int} and C_{Int}, the resistance connected in series which can be attributed to the bulk resistance has a value of 27 Ω and is constant within a range of $\pm$ 2 Ω when the mechanical stress is increased up to 250 MPa. Therefore, it can be concluded, that the conductivity change is solely driven by the piezotronic modulation of the electrostatic potential barrier at the bicrystal interface.

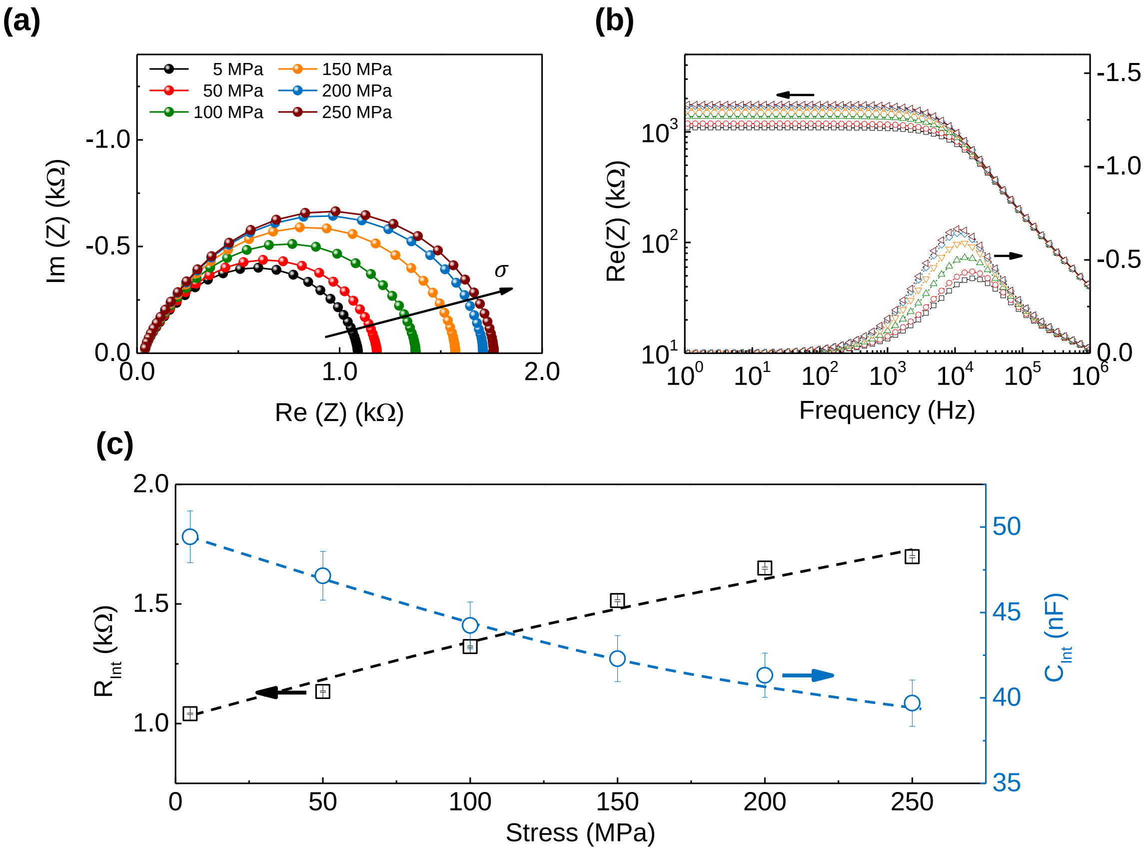

Figure 5-25: Stress-dependent impedance measurement of the bicrystal with Zn|Zn – interface. (a) Nyquist representation, (b) Spectroscopic plot of real and imaginary part of impedance, and (c) Extracted values of interface resistance and capacitance as a function of increasing uniaxial compressive stress.

Compared to the decreasing DC resistance seen for the O|O – interface, the impedance data obtained for the Zn|Zn – interface shows an increase in DC resistance with increasing mechanical load. The increase in DC resistance is a clear indication of an increasing potential barrier due to the generation of negative piezoelectric polarization charges. As already seen from *I-V* measurements (Figure 5-22), the absolute changes are smaller compared to the O|O – interface. Equivalent circuit analysis reveals an increase of R_{Int} from 1040 Ω at 5 MPa to 1700 Ω at an applied mechanical field of 250 MPa. Similar to the O|O – interface, the change in interface resistance determined from impedance measurements, is in good agreement with the resistance values in the leakage current regime (at 0.1 V) obtained by stress-dependent *I-V* measurements. Simultaneously, the interface capacitance (C_{Int}) decreases from 49 nF at 5 MPa to 40 nF at 250 MPa. The CPE exponent (α_{CPE}) for the Zn|Zn – interface is with a value around 0.85 slightly lower compared to the O|O – interface. From equation 5.13, it is evident, that the decrease in interface capacitance is caused by an increase in the width of the depletion region (W_D). Stress-induced negative polarization charges have to be compensated by an increasing donor concentration within W_D. This is primarily realized by an increase in W_D itself, as described by equation 5.14.

The bulk resistance is determined to be 51 Ω at 5 MPa, with a slight increase to 65 Ω at a mechanical load of 250 MPa. Compared to the increase in interface resistance, the change in bulk resistance is small and probably related to slight inaccuracies of the fitting procedure. Hence, the increase in overall resistance can again be attributed to an piezotronic interaction between piezoelectric polarization charges and the electrostatic potential barrier at the bicrystal interface. The opposite trend of R_{Int} as well as C_{Int} for the O|O – and Zn|Zn – interface and hence for positive and negative piezoelectric polarization charges confirms the fundamental theory of the piezotronic effect as already described for the grain boundaries of polycrystalline varistor ceramics (equation 2.31).

However, the piezotronic effect seems to be more pronounced for the barrier lowering case at the O|O – interface as compared to the increasing potential barrier at the Zn|Zn – interface. To explain the different impact of positive and negative piezoelectric charge on the electrostatic potential barrier height, the Fermi-level pinning mechanism as explained in chapter 2.3.2 and 3.3.3 needs to be accounted for. If, in the stress-free state, empty defect states exist above the Fermi-level, an initial reduction in Φ_{DSB} will be compensated by an increase in negative interface charge Q_I. This mechanism is referred to as Fermi-level pinning and is in detail explained by equations 2.26 to 2.28 as well as by Figure 2-12 and 2-14. Only when all empty defect states are filled, will the stress-induced positive piezoelectric charges unambiguously decrease the potential barrier height. In principle, the same mechanism accounts for an increasing potential barrier due to the generation of negative piezoelectric polarization charges. In this case, not empty defect states above the Fermi-level will be filled, but filled defect states below the Fermi-level well be emptied. The decreasing value of Q_I will partially compensate the stress-induced piezoelectric polarization charge and by this attenuate the observed increase in potential barrier height. Now, the difference in stress sensitivity for positive and negative piezoelectric charges can be explained by the distribution of defect states at the interface ($N_i(E)$). It can be assumed, that the density of empty defect states above the Fermi-level is lower compared to the number of filled states below the Fermi-level. Hence, in the case of an increasing potential barrier, the pinning mechanism is more pronounced, since a higher number of piezoelectric polarization charge can be compensated by emptying filled interface states. In the case of positive piezoelectric charges and a decreasing potential barrier, defect states above the Fermi-level seem to be filled rather soon, therefore a pronounced stress dependence of the current can be observed for the O|O – interface. Besides the absolute amount of defect states below or above the Fermi-level, also the shape of the density of states defines the effectiveness of the pinning mechanism (compare Figure 2-12 b). Therefore, the large number of filled defect states below the Fermi-level cannot perfectly counterbalance the barrier increase due to negative piezoelectric polarization charges and a small, but steady increase in barrier resistance can be observed (see Figure 5-25 (c)).

To further understand the interaction between mechanical stress and potential barrier height, the effective potential barrier height as a function of stress needs to be determined. Therefore, temperature-dependent conductivity measurements were performed for different values of uniaxial compressive stress. The measurements were performed on a second bicrystal with O|O – interface and similar electrical properties (see Figure A-3).

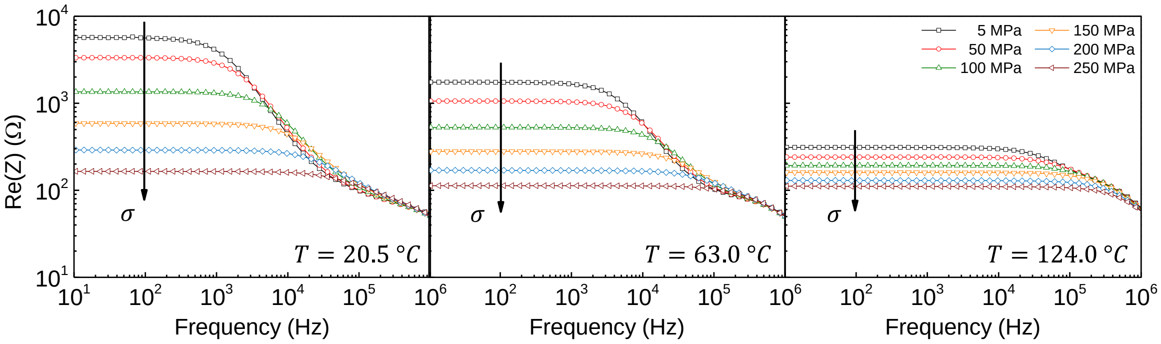

Figure 5-26: Spectroscopic plot of real part of impedance as a function of applied uniaxial compressive stress measured at different temperatures (increasing from left to right).

As can be seen from Figure 5-26, the second bicrystal with O|O – interface features the same stress-dependent behavior of the real part of impedance as the bicrystal represented in Figure 5-24. The DC resistance of the second bicrystal under stress-free condition is with 5692 Ω slightly higher, but with increasing mechanical stress, the resistance decreases in the same fashion down to 165 Ω at 250 MPa. Therefore, it can be assumed, that the structural and electrical properties of the second bicrystal are comparable to the one studied before. By increasing the temperature, the values of DC resistance for all levels of uniaxial stress decrease which can be attributed to an increased thermal excitation of majority charge carriers across the electrostatic potential barrier. The change in resistance due to an increase in temperature is more pronounced for the stress-free state compared to higher values of uniaxial compressive stress. The change in temperature dependence with increasing mechanical stress can be related to the decrease in potential barrier height and therefore to different activation energies across the barrier. To calculate the potential barrier height from stress- and temperature-dependent impedance measurement, pure thermionic emission can be considered:[228]

$$G = G_0 \exp\left(-\frac{E_A}{kT}\right), \tag{5.15}$$

with $G = 1/R_{Int}$ being the conductance measured across the barrier. By plotting the logarithm $\ln(G)$ versus the inverse temperature $1/T$, the activation energy E_A across the electrostatic potential barrier can be calculated from a linear fit, a procedure widely used in literature.[178, 229, 230] In this work, the conductance was calculated from the resistance value at 10 Hz, which is the dc value, as can be seen from Figure 5-26. The obtained Arrhenius plots are depicted in Figure 5-27 (a).

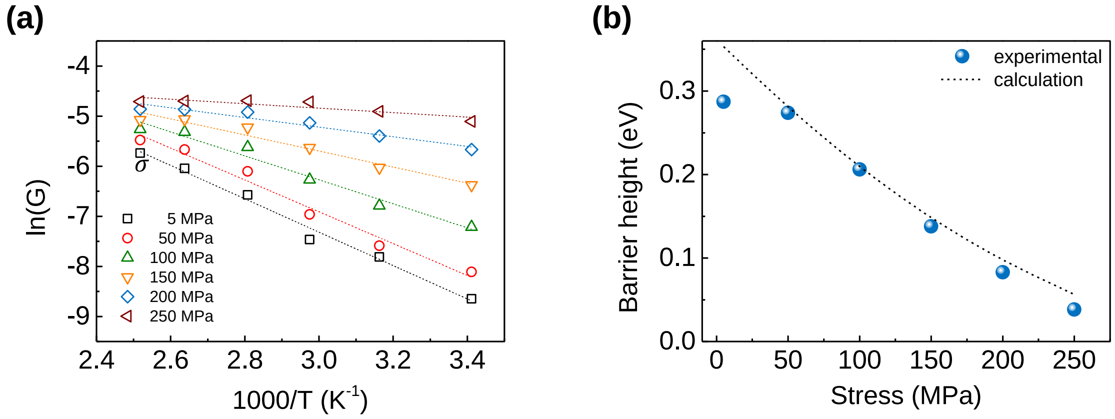

Figure 5-27: (a) Arrhenius type plot of the conductance G determined from temperature- and stress-dependent impedance measurements. (b) Comparison of experimental barrier height from Arrhenius evaluation (blue dots) and calculated barrier height after Verghese and Clarke.[25]

From a linear fit for the data represented in the Arrhenius plot, the activation energy for every stress state can be determined. In first approximation, the activation energy can be seen as the potential barrier height when purely thermionic emission of charge carriers across the potential barrier is assumed. Figure 5-27 (b) depicts the determined potential barrier height as a function of applied mechanical stress. At 5 MPa a potential barrier height of 0.29 eV can be determined which decreases by 0.25 eV down to 0.04 eV at 250 MPa. Compared to typically discussed values of potential barrier heights at the grain boundaries of polycrystalline varistor ceramics, a barrier height of 0.29 eV in stress-free state is comparably small. This may be attributed to the prolonged temperature treatment, which is known to be detrimental for the potential barrier height due to a loss in interfacial defect state density.[154, 231] However, under the application of mechanical stress, the potential barrier is almost completely eliminated. To rationalize the observed change in potential barrier height, equation 2.31 can be applied. From the direct piezoelectric effect as described by equation 2.2 and the present sample configuration, the amount of stress-induced charge is given by $Q_P = 2d_{33}\sigma_{33}$. Under the assumption of a donor density of $N_d = 2.5 \times 10^{18}\ cm^{-3}$ and a negative interface charge density of $Q_I = 6 \times 10^{12}\ cm^{-2}$ in the stress-free state, the experimental results can be well described. In literature, similar values are given for Q_I and N_d.[136] Nevertheless, it should be mentioned, that the value of Q_I used for the calculation is slightly lower und the applied value of N_d is slightly higher than values given for typical polycrystalline varistor ceramics. This may be attributed to the atypical temperature treatment needed to promote epitaxial growth. The calculation is represented by the dashed black line in Figure 5-27 (b). The calculation based on equation 2.31 neglects the Fermi-level pinning mechanism by empty defect states. Therefore, the good correlation between the experimental data and calculation for stress values of 50 MPa and higher indicates that after 50 MPa the interfacial defect states are completely filled. This seems to be not the case for the stress-free state where a small deviation between the calculated and experimentally determined potential barrier height can be seen. The smaller experimental barrier height implies a by around $0.5 \times 10^{12}\ cm^{-2}$ lower value for Q_I compared to the value used in the calculation. Due to the stress-induced lowering in potential barrier height, these states move below the Fermi-level and are occupied by free electrons, stabilizing the potential barrier height between 5 and 50 MPa and by this being responsible for the experimentally observed behavior. Under the application of 250 MPa, the potential barrier height is decreased by 0.25 eV which corresponds to a decrease by 86 % of its initial value. Compared to existing studies on the piezotronic performance of metal-ZnO Schottky contact, the observed stress sensitivity of the bicrystal interfaces is considerably higher. This is also evident from the studies in this work, when the results of the piezotronic bicrystal are compared to the piezotronic modulation of Schottky contacts to bulk ZnO single crystals (chapter 5.1). On the other hand, in contrast to piezotronic systems based on polycrystalline varistor ceramics, the device can be operated at very low voltages. In *I-V* measurements, the highest stress sensitivity can be seen at 0.1 V and in impedance measurements, the high stress sensitivities are reported for an ac field of 0.015 V. To further demonstrate the stress sensitivity and applicability of individual bicrystal interfaces for piezotronic applications, conductivity measurements were performed while linearly increasing the applied mechanical stress. The measurement was performed on the O|O – interface which was studied first. A probe signal frequency of 50 Hz was chosen since it is high enough to ensure a good time resolution between each measurement point, while it is low enough to make sure, that the determined conductivity value is still in the dc range (see Figure 5-24 (b)).

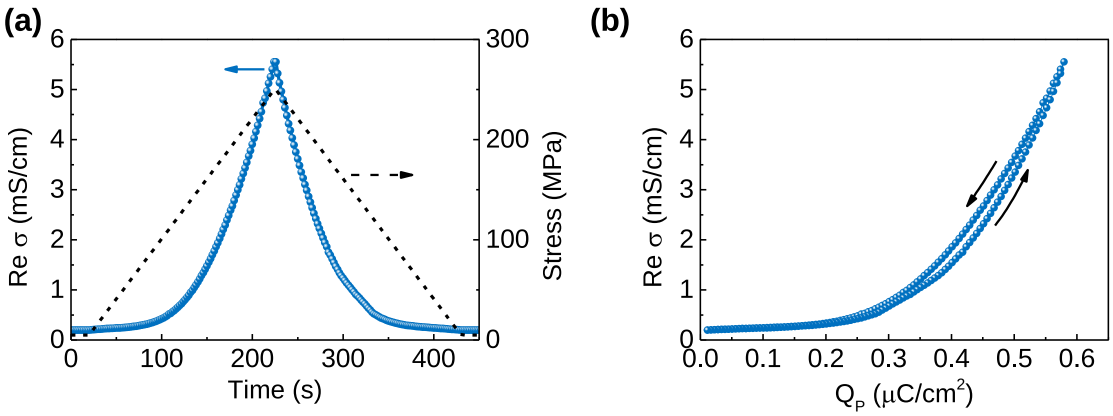

Figure 5-28: (a) Conductivity-time measurement of the bicrystal with O|O – interface under linearly increasing and decreasing mechanical stress from 5 MPa up to a value of 250 MPa and back to 5 MPa in a triangular shape. (b) Conductivity as a function of stress-induced piezoelectric polarization (Q_P).

As can be seen from Figure 5-28, the measured conductivity follows the applied mechanical stress. The amount of piezoelectric polarization charge (Q_P) linearly depends on the applied mechanical stress. With increasing Q_P, the measured conductivity increases in an exponential fashion, which is well in agreement with the theoretical predictions from equations 2.31 and 5.14. In Figure 5-28 (b), a small hysteresis between loading and unloading is apparent, which is not evident from the theoretical description as used before. Time-dependent screening and compensation mechanisms could be responsible for the observed hysteresis. To shed light on possible screening mechanisms, additional conductivity-time measurements were conducted with different loading profiles as depicted in Figure 5-29. After removing the mechanical stress from 100 MPa, the conductivity is constant (see Figure 5-29 (b)). In contrast, when the mechanical stress is increased to 150 MPa and held constant at that value, the measured conductivity decays by about 10 % within the read-out time of 60 s. This decay may be attributed to charge redistribution or screening mechanisms. However, the small hysteresis in Figure 5-28 (b) and the small decay of only 10 % present in Figure 5-29 (c), demonstrate, that screening mechanisms do not have a profound influence on the piezotronic modulation of electrostatic potential barriers in varistor-type bicrystal interfaces. From piezoelectric measurements on ZnO single crystals with existing depletion region, it is known that the reduced charge carrier density in the depleted region prevents screening of the piezoelectric potential, as was discussed within chapter 5.2. In the vicinity of varistor-type double Schottky barriers a symmetric depletion region into both adjacent grains is induced, possibly preventing stress-induced piezoelectric polarization charges from being screened by free charge carriers.

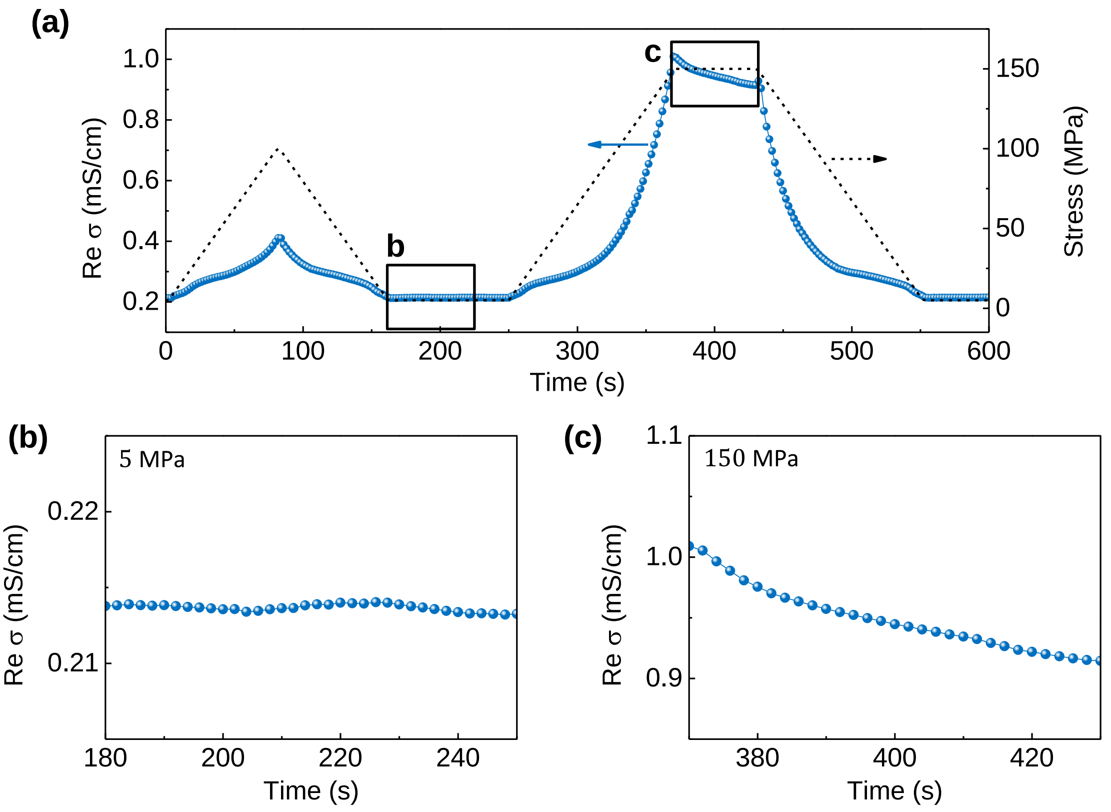

Figure 5-29: (a) Conductivity-time measurement of the bicrystal with O|O – interface with different stress profiles. (b) Conductivity-time measurement in stress-free (5 MPa) state. (c) Conductivity-time measurement at 150 MPa.

5.3.3. Summary – Piezotronic effect of ZnO bicrystals

Epitaxial solid-state transformation of a polycrystalline sacrificial layer in between two well oriented single crystals is found to be a new promising concept to prepare individual semiconductor-semiconductor interfaces for piezotronic applications. The chemistry of the sacrificial layer gives control over the chemical composition and by this the defect density of the ensuing interface. Consequently, an electrostatic potential barrier forms at the bicrystal interface which can be tailored by stress-induced piezoelectric charge. Furthermore, a precise adjustment of the piezoelectric polarization vectors either in head-to-head or tail-to-tail orientation can be achieved by defining the orientation of the single crystals prior to temperature induced epitaxial solid-state transformation. The orientational degree of freedom maximizes the amount of stress-induced polarization charge and allows to define the sign of Q_P being positive or negative, respectively. By the generation of piezoelectric charge, the charge transport across the electrostatic potential barrier can be modified. *I-V* and impedance measurements confirm the fundamental concept of the piezotronic effect. In particular, a decrease in barrier height for positive piezoelectric charge and an increase in barrier height for negative piezoelectric charge is noted. The different stress sensitivities for a decreasing and an increasing potential barrier can be well rationalized by the implications of the Fermi-level pinning mechanism for the piezotronic interaction between piezoelectric charge and electrostatic potential. For the barrier lowering case, Arrhenius evaluation of temperature-dependent impedance measurements reveals an extremely high barrier change of 86 %. From 0.29 eV in the stress-free state, the barrier can almost be entirely decreased by 0.25 eV down to a value of 0.04 eV at 250 MPa. Compared to the piezotronic modulation of metal-ZnO Schottky contacts, the attainable stress sensitivity observed on doped bicrystal interfaces is dramatically enhanced. At this stage, the stress sensitivity seems only to be limited by the initial potential barrier height. Due to the harsh temperature treatment, the initial potential barrier height is rather small. If the preparation process could be adjusted such, that the high temperature treatment is avoided, a further increase in achievable conductivity change can be expected. Nevertheless, the reversibility of the conductivity change as well as the low operating voltages indicate a high applicability of doped semiconductor-semiconductor interfaces in a multitude of future piezotronic devices.

5.4. Piezotronic effect of single crystal – polycrystal structures

Electrostatic potential barriers at doped ZnO-ZnO interfaces can be modified by stress-induced piezoelectric polarization charges. The change in potential barrier height is utilized to mechanically tune the electrical conductivity. The general concept was demonstrated for an interplay of a multitude of grain boundaries in a polycrystalline varistor ceramic as well as for individual bicrystal interfaces as in detail described in chapter 5.1.[168, 220] In a polycrystalline ceramic, high stress sensitivities can be achieved, but high operating voltages are necessary due to the large number of potential barriers connected in series and parallel. On the other hand, for bicrystal interfaces, the operation voltage could be significantly reduced but the harsh temperature treatment during epitaxial solid-state transformation is detrimental for the formation of the initial potential barrier height. The low initial potential barrier height is believed to limit the stress sensitivity of bicrystals prepared by epitaxial solid-state transformation. In this chapter, the interplay between the high temperature treatment during epitaxial growth and the attainable stress sensitivity of single crystal – polycrystal structures with varying amount of remaining polycrystalline material will be studied, thereby closing the gap between piezotronic devices based on polycrystalline varistor ceramics and individual bicrystal interfaces. In the first part of this section (chapter 5.4.1), the microstructure and electrical characteristics in the stress-free state as a function of time for epitaxial growth of the single crystals into the polycrystal will be discussed. In chapter 5.4.2, the stress sensitivity of the prepared structures is evaluated. Parts of the here presented data have been previously published as an article in the Journal of the American Ceramic Society.[232]

5.4.1. Preparation of single crystal – polycrystal structures

To prepare single crystal – polycrystal structures with varying amount of remaining polycrystalline material in between two well oriented single crystals, the same epitaxial solid-state transformation process as applied for the preparation of individual bicrystal interfaces can be utilized (see chapter 5.1). The thickness of the remaining polycrystalline layer is adjusted by choosing different times for high temperature treatment. In this study, high temperature treatments were performed for 2, 20, 40, and 60 h, which should lead to a decreasing thickness of the polycrystalline layer. Since the number of grain boundaries, and therefore, the number of electrostatic potential barriers of the prepared structures determine the overall electrical properties, a detailed microstructural analysis was conducted and will be discussed within the next part of this chapter.

Microstructural characterization

With increasing time of the high temperature treatment, epitaxial growth of the single crystals into the polycrystalline layer as well as grain growth within the polycrystalline layer is expected. To systematically study the microstructure, SEM images were recorded across the whole cross sectional interface of each sample. Figure 5-30 features images recorded at the edge as well in the center of each structure. From SEM images, it is evident that epitaxial growth is more advanced in the center of the structures compared to the edges. Even for 60 h of high temperature treatment, polycrystalline material is still present, especially at the edges of the samples.

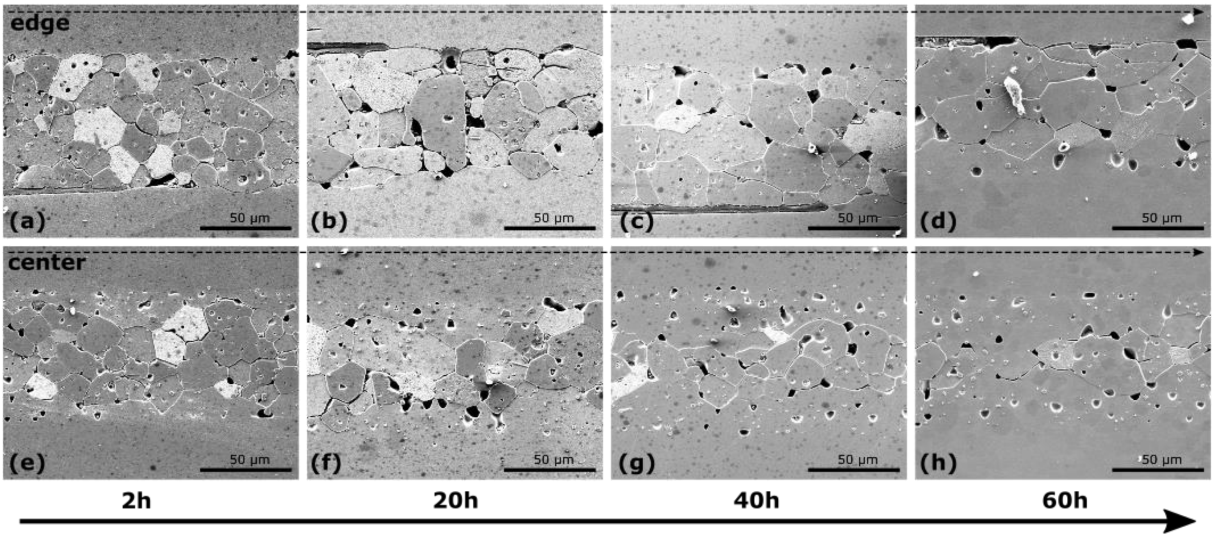

Figure 5-30: Cross sectional SEM images of the prepared single crystal – polycrystal structures with increasing time for epitaxial growth from left to right (2, 20, 40, and 60 h) Images (a) to (d) were recorded at the edge of the structures while images (e) to (h) were taken in the center of the structures.

The thickness of the remaining polycrystalline material was measured at least at 65 positions across the whole interface of each sample. As can be seen from the micrographs in Figure 5-30, the growth front is not perfectly linear, but a meandering interface between the single crystals and the remaining polycrystalline material evolves. For reasonable comparison between the samples, the average thickness of the remaining polycrystalline material was calculated as it is depicted in Figure 5-31 (a). In addition, the average of the smallest and largest value in each image was calculated (open triangles), representing an estimate for the variation between maximum and minimum growth. With increasing time for epitaxial growth, the thickness of the remaining polycrystalline layer decreases from about 60 μm for the 2 h annealed sample down to 32 μm after 60 h of annealing. Figure 5-31 (b) shows the distance of epitaxial growth for both crystals in one structure normalized to the initial thickness of the polycrystalline layer. An almost linear increase in epitaxial growth with time can be seen. Due to the meandering interface, there are huge fluctuations between measurements at different positions which reflects itself in the large difference between the average values for maximum and minimum growth.

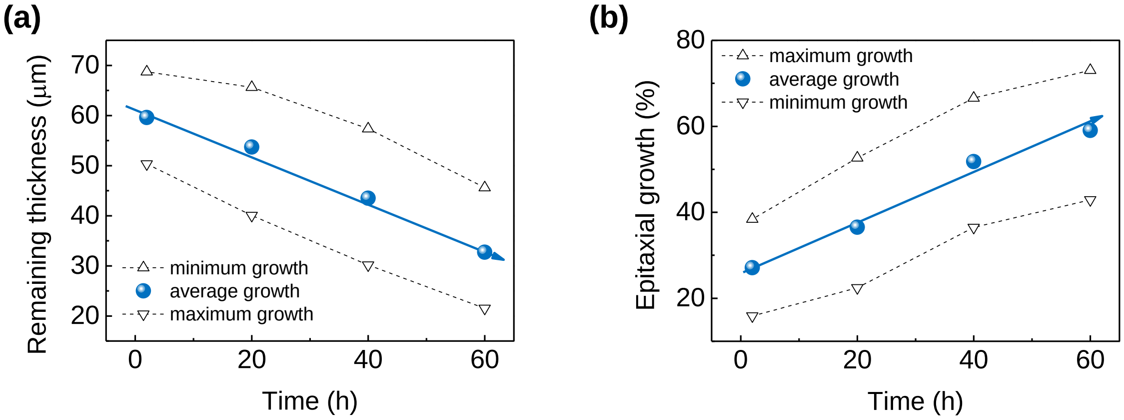

Figure 5-31: (a) Remaining average thickness of the polycrystalline layer as a function of increasing time for epitaxial growth (blue circles). Open triangles indicate the determined maximum and minimum values of each picture averaged across the whole interface. (b) Relative epitaxial growth normalized on the initial thickness of the polycrystalline sacrificial layer.

Besides epitaxial growth, the prolonged high temperature treatment also promotes grain growth within the polycrystalline material. The average grain size determined from the grain cross sectional area of at least 200 grains across the entire width of the remaining polycrystalline layer is depicted in Figure 5-31 (a). The average grain size increases from 21 μm for the 2 h annealed sample to about 26 μm for the structure which was annealed for 20 h. With further increasing time of the high temperature treatment the grain size only increases slightly to 28 μm after 60 h of annealing. It has to be noted, that the variation in grain size for the individual annealing times is significant. This can be seen from the error bars in Figure 5-32 (a), which reflect the standard deviation of the determined grain size distributions. The slight increase in grain size together with the decreasing thickness of the remaining polycrystalline layer reduces the average number of grains and with this the average number of grain boundaries between the two single crystals and outer electrodes, respectively (see Figure 5-32 (b)).

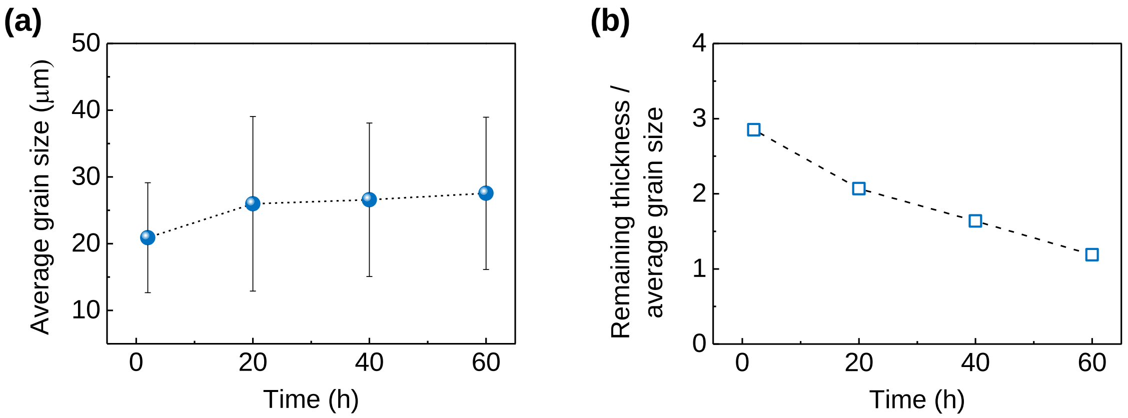

Figure 5-32: (a) Average grain size within the remaining polycrystalline layer of the prepared structures with increasing time of high temperature treatment. (b) Average number of grains between the two single crystals with increasing time of high temperature treatment.

The number of grain boundaries between the two outer electrodes and with this, the number of electrostatic potential barriers should have a profound influence on the electrical properties of the prepared structures. Therefore, the structural analysis needs to be considered when interpreting the electrical measurements in the following section. However, the average values presented in this section should be treated with care when directly correlating the determined values with electrical properties. For polycrystalline varistor ceramics, current localization due to variations in microstructure is known to highly influence the electrical response of the ceramics (see chapter 2.3.4). As can be seen from the meandering interface in Figure 5-30 and the large standard deviation of the determined grain size distribution as depicted in Figure 5-32 (a), the prepared single crystal – polycrystal structures reveal a distinct microstructural inhomogeneity. Therefore, considerable current localization can be expected. Still, the average values of e.g. the remaining thickness of the polycrystalline layer nicely illustrates the expected correlation between epitaxial growth and time of the conducted high temperature treatment.

Electrical characterization

With increasing time of epitaxial growth, two mechanisms are believed to influence the electric properties in the stress-free state. In the first place, the number of potential barriers connected in series determines the breakdown voltage. This correlation is known from polycrystalline varistor ceramics, where the number of grain boundaries can be used to adjust the breakdown voltage of varistor devices in surge arrestor applications.[133] [233] To study the influence of a reduced average number of potential barriers between the two outer electrodes as it was determined from microstructural analysis, *I-V* measurements were performed in the stress-free state, which are depicted in Figure 5-33 (a).

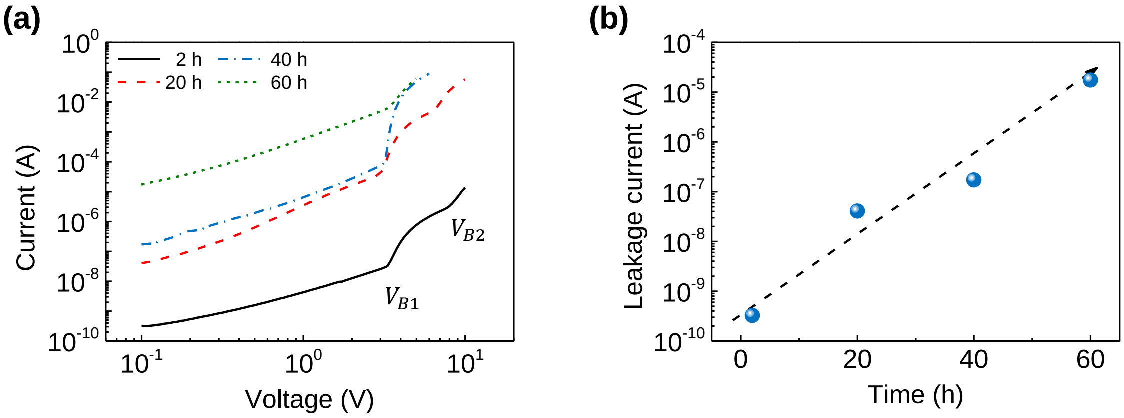

Figure 5-33: (a) Current-voltage characteristics in the stress-free state of the single crystal – polycrystal structures after 2, 20, 40, and 60 h of epitaxial growth. (b) Leakage current determined at 0.1 V as a function of time for epitaxial growth.

The leakage current determined at 0.1 V is shown in Figure 5-33 (b) and features a severe increase with increasing time of the high temperature treatment. From around $3.2 \cdot 10^{-10}$ A for the 2 h annealed structure, the leakage current increases by almost five orders of magnitude to around $1.7 \cdot 10^{-5}$ A for the 60 h annealed sample. In the observed voltage and current range, all structures feature a characteristic breakdown voltage between 3.4 and 3.8 V, which is typical for individual varistor-type potential barriers. Like in chapter 5.3.1, the breakdown voltages were determined at the point, where the coefficient of nonlinearity (α) reveals its maximum. Compared to the longer annealed samples, the structures annealed for 2 and 20 h feature an additional breakdown voltage at 9.1 and 7.2 V, respectively. The values for V_B of 7.2 and 9.1 V indicate the transitions of pathways from the leakage current regime to the conductive state where more than one potential barrier is connected in series. For the structures annealed for 40 or 60 h, the current transport seems to be conducted through pathways dominated by only one active electrostatic potential barrier. The structures annealed for 2 or 20 h have a more complex current response. The more complex behavior of the shorter annealed structures results from the higher average number of grain boundaries between the two electrodes. At higher voltages additional conducting pathways seem to contribute to the overall current transport.

However, the dramatic increase in leakage current by almost five orders of magnitude cannot only be explained by the decreasing average number of potential barriers between the two outer electrodes. In the leakage current regime, the current linearly depends on the applied voltage ($\alpha = 1$). Hence, the leakage current should also linearly depend on the number of potential barriers which are connected in series, if all potential barriers feature the same potential barrier height. By decreasing the average number of potential barriers between the two electrodes from e.g. 4 to 1, a four-fold increase in leakage current should be expected. Therefore, the decreasing thickness of the remaining polycrystalline layer cannot rationalize the severe increase in leakage current as depicted in Figure 5-33 (b), if the potential barrier height at each interface is expected to remain constant with ongoing high temperature treatment. The exponential increase in leakage current may only be explained by a decreasing potential barrier height at the individual grain boundaries itself with increasing annealing time. Similar observations were made in polycrystalline varistor ceramics, where a varistor to conductor transition happens with increasing sintering time of the ceramic.[154] The varistor to conductor transition was attributed to a change in chemical composition at the grain boundaries due to Bi_2O_3 volatilization. To demonstrate the change in potential barrier height with ongoing high temperature treatment, temperature-dependent conductivity measurements were performed on samples with annealing times of 2 and 60 h, respectively. Therefrom, the activation energy across the electrostatic potential barriers can be extracted and hence, the barrier height can be approximated. The procedure is similar to the barrier height determination of the bicrystal interface as a function of stress, which was already described in chapter 5.3.2.

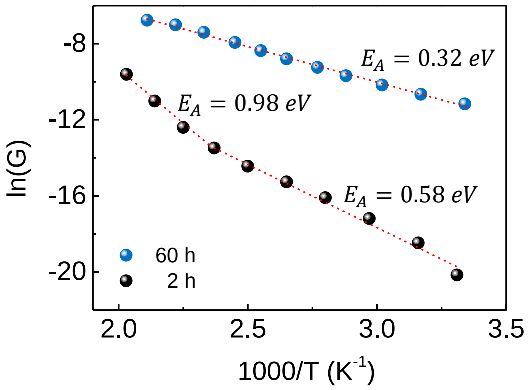

Figure 5-34: Arrhenius type plot of the conductance G determined from temperature-dependent impedance measurements in the stress-free state for the 2 and 60 h annealed single crystal – polycrystal structures.

From Arrhenius evaluation, a significant difference between the structures annealed for 2 and 60 h is evident. The structure annealed for 2 h shows a change in slope within the ln(G) vs 1/T plot, indicating the presence of a low- and a high temperature process. Similar effects were already observed in polycrystalline varistor ceramics, where the change in slope was attributed to distributions in potential barrier height.[168, 178] The activation energy of the low temperature process is determined to be 0.52 eV, while the high temperature process has an activation energy of 0.98 eV. The activation energy of the high temperature process is well in the range of barrier heights reported for polycrystalline varistor ceramics.[134] The lower activation energy at low temperatures, can be attributed to percolating pathways through the single crystal – polycrystal structure, which seem to dominate the current transport at room temperature and low voltages. On the other hand, for the 60 h annealed structure, only one process with significantly lower activation energy is detectable. The low activation energy of 0.32 eV determined for the 60 h annealed structure confirms the expected detrimental influence of the high temperature treatment on the initial potential barrier height during epitaxial growth and is most probably responsible for the dramatic increase in leakage current seen in *I-V* measurements.

Microstructural and electrical characterization, in stress-free state, of the single crystal – polycrystal structures reveals a profound influence of the high temperature treatment on the electrical properties. The high temperature treatment decreases the number of grain boundaries within the polycrystalline layer and by this, the number of electrostatic potential barriers between the two electrodes. Furthermore, the potential barrier height itself is decreased by ongoing high temperature treatment. In the following chapter, the influence of the changed microstructure and electrical characteristic on the attainable stress sensitivity is studied.

5.4.2. Stress sensitivity of single crystal – polycrystal structures

The orientation of the two single crystals was defined such that an ensuing polarization vector in both single crystals points towards the polycrystalline layer. Hence, at the grain boundaries between the polycrystal and the single crystals, positive piezoelectric charges should preferentially decrease an existing potential barrier. For the potential barriers at grain boundaries within the polycrystalline material, a statistical distribution of relative grain orientation is expected. Therefore, an existing potential barrier at such grain boundaries can be increased or decreased, depending on the grain boundary orientation. From stress-dependent measurements in polycrystalline varistor ceramics, it is known that due to percolation effects, the overall conductivity increases for a multitude of randomly oriented grain boundaries.[25, 168] Hence, an increase in conductivity is expected for the structures with the here chosen orientation under the application of compressive stress. Figure 5-35 shows the stress-dependent *I-V* measurements of the structures with increasing time for epitaxial growth.

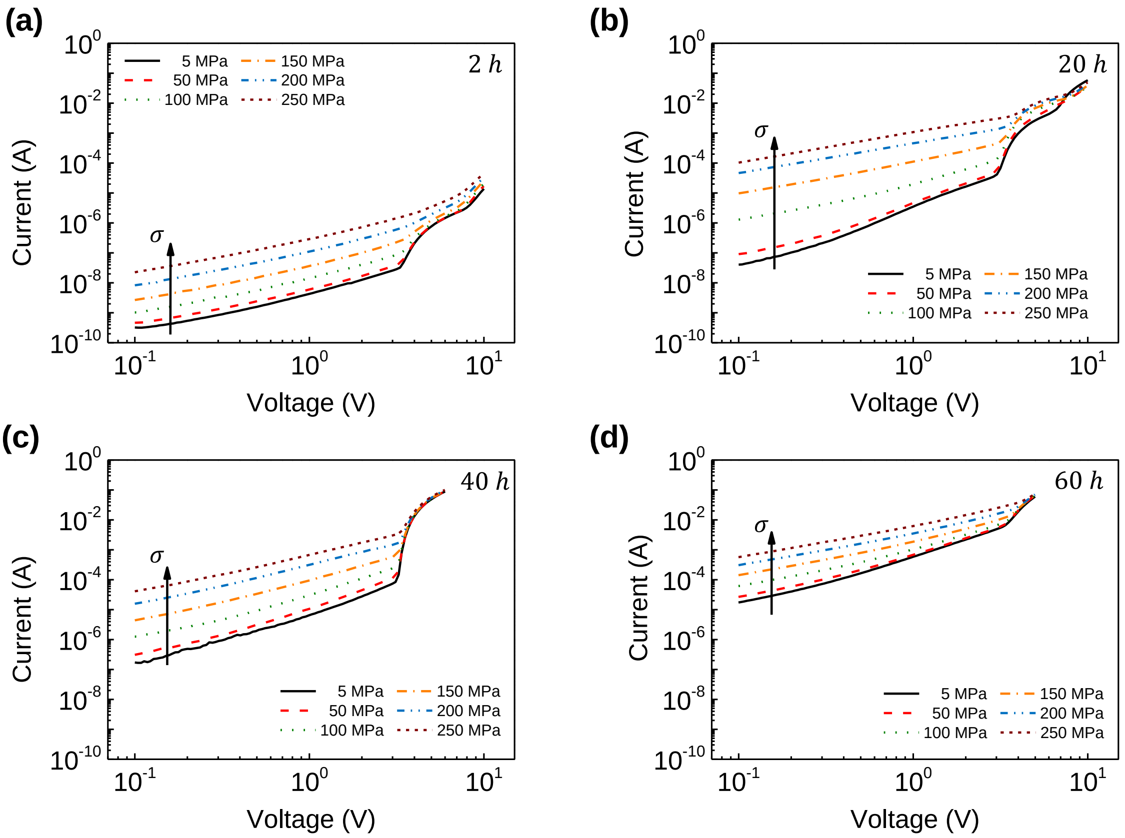

Figure 5-35: Stress-dependent *I*-*V* measurements of the single crystal – polycrystal structures annealed for 2 h (a), 20 h (b), 40 h (c), and 60 h (d).

For reasons of comparability, the plots of the *I*-*V* measurements for all structures are shown in the same current and voltage range. All structures feature a pronounced change in electrical conductivity under the application of uniaxial compressive stress. The highest change in conductivity can be observed in the pre-breakdown region at 0.1 V. To compare the stress sensitivities of the structures, the relative change in current ($\Delta I/I_0$) was determined at 0.1 V and is plotted as a function of annealing time (see Figure 5-36). For the shortest (2 h) annealed structure, a relative change in current of $\Delta I/I_0 = 73$ can be observed. By increasing the time for epitaxial growth to 20 h, the stress sensitivity can be dramatically increased to $\Delta I/I_0 = 2640$, whereas a further increase in annealing time does not lead to a further increase in stress sensitivity. The opposite is observed, when the annealing time is further increased, the stress sensitivity decreases to $\Delta I/I_0 = 253$ for the 40 h annealed structure and $\Delta I/I_0 = 32$ for the 60 h annealed structure. Regarding the stress sensitivity, 20 h of high temperature treatment is the optimum time. In contrast, the shortest (2 h) and the longest (60 h) annealing times feature the lowest stress sensitivities.

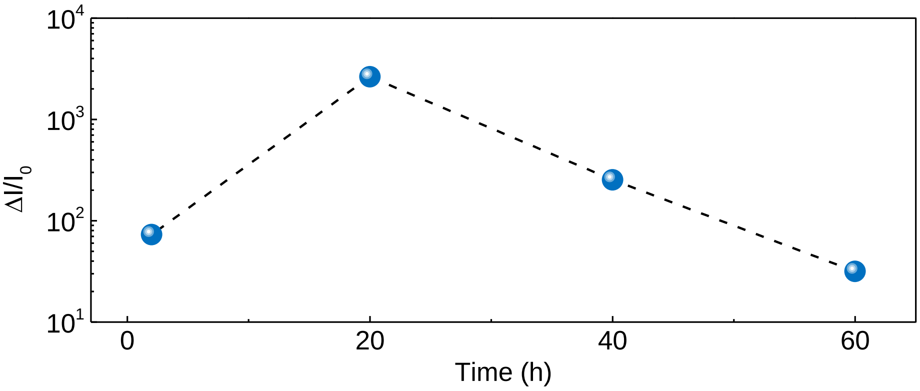

Figure 5-36: Relative change of current ($\Delta I/I_0$) determined at 0.1 V as a function of time for epitaxial growth.

Two competing mechanisms can be accounted for to explain the maximum in stress sensitivity for intermediate times of epitaxial growth. As described before, the grain orientation in the polycrystalline layer is random. Hence, the relative orientation of the polarization vectors in the two adjacent grains at a grain boundary within the polycrystalline layer is also randomly distributed. Under the application of mechanical stress, the orientation of the ensuing polarization vectors at one grain boundary within the polycrystalline layer can be in head-to-head, tail-to-tail, and head-to-tail respectively. As already described by Verghese and Clarke[25] and as confirmed within chapter 5.3.2, at an interface with head-to-head orientation, positive polarization charges will decrease an existing potential barrier whereas at interfaces with tail-to-tail orientation, negative polarization charges will increase an existing potential barrier. Even if the number of increasing and decreasing potential barriers in a polycrystalline material was the same, percolating pathways through the microstructure with a preferentially decreasing overall potential barrier height will evolve, due to the statistical relative grain orientation. Hence, an overall increase in electrical conductivity would be observed. For interfaces with head-to-tail orientation of the polarization vector, negative and positive polarization charges from the two grains will compensate each other. If the angle between the interface and both polarization vectors is the same, the amount of positive and negative polarization charge from the two adjacent grains is the same and no change in potential barrier height is expected. However, if the angle between the two polarization vectors and the corresponding interface is different, the piezoelectric charges will not be perfectly compensated. This consideration is of importance for the interfaces between the polycrystalline layer and the single crystals. The orientation of the single crystals is defined during the manufacturing process such, that an evolving polarization under compressive stress is positive. Therefore, at both interfaces between the polycrystalline layer and the single crystals exclusively positive polarization charges can be induced by the application of mechanical stress. Only in the unlikely event where the ensuing polarization vector within a grain adjacent to the single crystal generates negative piezoelectric charges and exhibits the same angle with respect to the interface as the polarization vector in the single crystal, no piezoelectric charge is generated at the interface. Across the whole interface the potential barriers between the polycrystalline layer and the single crystals are preferentially decreased when compared to the average potential barrier at randomly oriented grain boundaries. Now, with increasing time for epitaxial growth, the percentage of the favorably oriented interface between the polycrystalline layer and the single crystals is, in comparison to the overall number of grain boundaries, increased. Hence, the overall percentage of interfaces having electrostatic potential barriers which are preferentially decreased by mechanical stress increases. This phenomenon should result in an increasing stress sensitivity with increasing time for epitaxial growth and can rationalize the observed increase in stress sensitivity between the 2 h and 20 h annealed structure. However, it cannot explain the decreasing stress sensitivity with further increasing the time for epitaxial growth to 40 and 60 h. As demonstrated in chapter 5.4.1, the leakage current of the structures significantly increases with increasing time of the high temperature treatment. The increase in leakage current could be partially explained by the decreasing number of electrostatic potential barriers between the two outer electrodes. Nevertheless, the major contribution to the increasing leakage current is found to be induced by a decreasing initial potential barrier height due to the harsh temperature treatment during epitaxial growth. Since the achievable stress sensitivity in piezotronic devices is related to the ratio of the potential barrier resistance to the bulk resistance, a decreasing barrier resistance in the stress-free state will decrease the attainable stress sensitivity.[2]

5.4.3. Summary – Piezotronic effect of single crystal – polycrystal structures

In this chapter, the influence of the high temperature treatment during epitaxial solid-state transformation on the stress sensitivity of single crystal – polycrystal structures was discussed. By varying the time for epitaxial growth, the amount of remaining polycrystalline material between two well oriented single crystals could be adjusted. It is found, that structures with intermediate times of epitaxial growth (20 h and 40 h) feature higher stress sensitivities compared to shorter (2 h) and longer (60 h) annealed structures. The increasing stress sensitivity between the 2 h and 20 h annealed structures is attributed to the increasing percentage of ZnO-ZnO interfaces with favorably oriented polarization vectors regarding a desired lowering in potential barrier height. For longer times of epitaxial growth, a dramatic increase in leakage current due to the decreasing number of potential barriers between the electrodes and a detrimental influence of the high temperature treatment on the initial potential barrier height is identified. With increasing leakage current the attainable stress sensitivity is decreased with ongoing high temperature treatment. The above explained, competing mechanisms therefore rationalize the superior stress sensitivities obtained for single crystal – polycrystal structures with intermediate times of epitaxial growth. Compared to piezotronic systems based on polycrystalline varistor ceramics, the attainable stress sensitivity is comparable, but the operating voltages could be decreased down to 0.1 V. The applied approach therefore demonstrates the great potential of microstructural engineering to increase the sensitivity of piezotronic devices based on polycrystalline varistor ceramics.

6. Concluding remarks and outlook

The main achievement within this work was the successful preparation of individual ZnO bicrystal interfaces for piezotronic applications, as described in chapter 5.3. Epitaxial solid-state transformation of a polycrystalline sacrificial layer in between two well oriented ZnO single crystals could be applied to create bicrystal interfaces with precise control over the polarization vector orientation as well as the chemical composition at the interface. The chemical composition of the interface could be adjusted by defining the chemical composition of the polycrystalline sacrificial layer, which was based on a typical varistor composition. Hence, the bicrystal interfaces feature the same electrical properties as individual grain boundaries in a polycrystalline varistor ceramic. In contrast to polycrystalline varistor ceramics, the existence of only one potential barrier results in predictable electrical properties and low operating voltages for future applications. In addition, orienting the polarization vectors within the ZnO single crystals defines the sign of, and maximizes, the stress-induced piezoelectric polarization charges at the interface. Hence, the prepared bicrystals were the ideal system to investigate the piezotronic modulation of electrostatic potential barriers at doped ZnO-ZnO interfaces.

The bicrystal structures revealed an increase and decrease in potential barrier height for the generation of negative and positive piezoelectric charges, respectively. Compared to piezotronic devices based in metal-ZnO Schottky contacts, the concept of utilizing ZnO bicrystal interfaces features extremely high stress sensitivities, which is a consequence of a different physical mechanism behind the piezotronic modulation of electrostatic potential barriers. As stated in literature and confirmed within chapter 5.1 of this work, the stress sensitivity of Schottky contacts is limited by the spatial separation between stress-induced piezoelectric charges and screening charges within the metal. This spatial separation, hence, the thickness of the interfacial gap layer cannot easily be extended by experimental approaches, thereby being an inherent shortcoming of piezotronic devices based on Schottky contacts. On the other hand, the local charge distribution at varistor-like ZnO-ZnO interfaces, where a negative sheet charge is screened by two symmetric depletion regions, results in a direct interconnection between stress-induced piezoelectric charge and the negative sheet charge accumulated at the interface. Therefore, mechanical stress directly translates into a modulation of the potential barrier height at such interfaces resulting in superior stress sensitivities of the piezotronic systems based on varistor-like potential barriers compared to Schottky contacts.

However, the prolonged high temperature treatment during epitaxial solid-state transformation was found to have a detrimental influence on the initial potential barrier height at the bicrystal interface (see chapter 5.4). After 65 h of epitaxial growth, the loss of volatile dopants like Bi decreases the number of interfacial defect states which resulted in a potential barrier height of only 0.29 eV. Since already at 250 MPa, the potential barrier could be almost completely extinguished, the low initial potential barrier height was found to limit the attainable stress sensitivity of the bicrystal interfaces prepared by epitaxial solid-state transformation. To further increase the stress sensitivity, the negative sheet charge density should be increased by optimizing the preparation process. Furthermore, the Fermi-level pinning mechanism is deemed responsible for the different stress sensitivities of an increasing and a decreasing potential barrier observed for the bicrystals with changed polarity. A different density of defect states above and below the Fermi-level results in a different magnitude of the pinning mechanism. In contrast to a decreasing barrier, a lower stress sensitivity is found for an increasing barrier, which is believed to be an inherent feature of piezotronic devices based on varistor-type electrostatic potential barriers.

Regarding future developments, the here presented work demonstrates the great potential of individual varistor-type bicrystal interfaces for piezotronic applications. The different physical mechanism of the interaction between potential barrier height and piezoelectric polarization results in a superior performance of varistor-type bicrystal interfaces compared to metal-ZnO Schottky contacts, which were mainly studied until now. This finding can promote future research into the direction of piezotronics based on individual ZnO-ZnO interfaces. Future work should focus on optimizing the preparation process to gain a more precise control over the interfacial defect state distribution. One approach could be the introduction of dopants by thin film techniques like sputter deposition or thermal evaporation. The key is, to prevent the detrimental influence of the high temperature treatment during bicrystal fabrication. Manipulating the interface coherency as already demonstrated in literature could also facilitate an additional tool to gain control over the defect state distribution. In general, preparation techniques need to be easy, cheap and compatible with the trend of miniaturization in semiconductor technology in order to provide a real alternative for existing concepts. Therefore, the here presented approach can be seen as starting point for technological development of micro- and nano-sized ZnO-ZnO interfaces for piezotronic applications.

Appendix

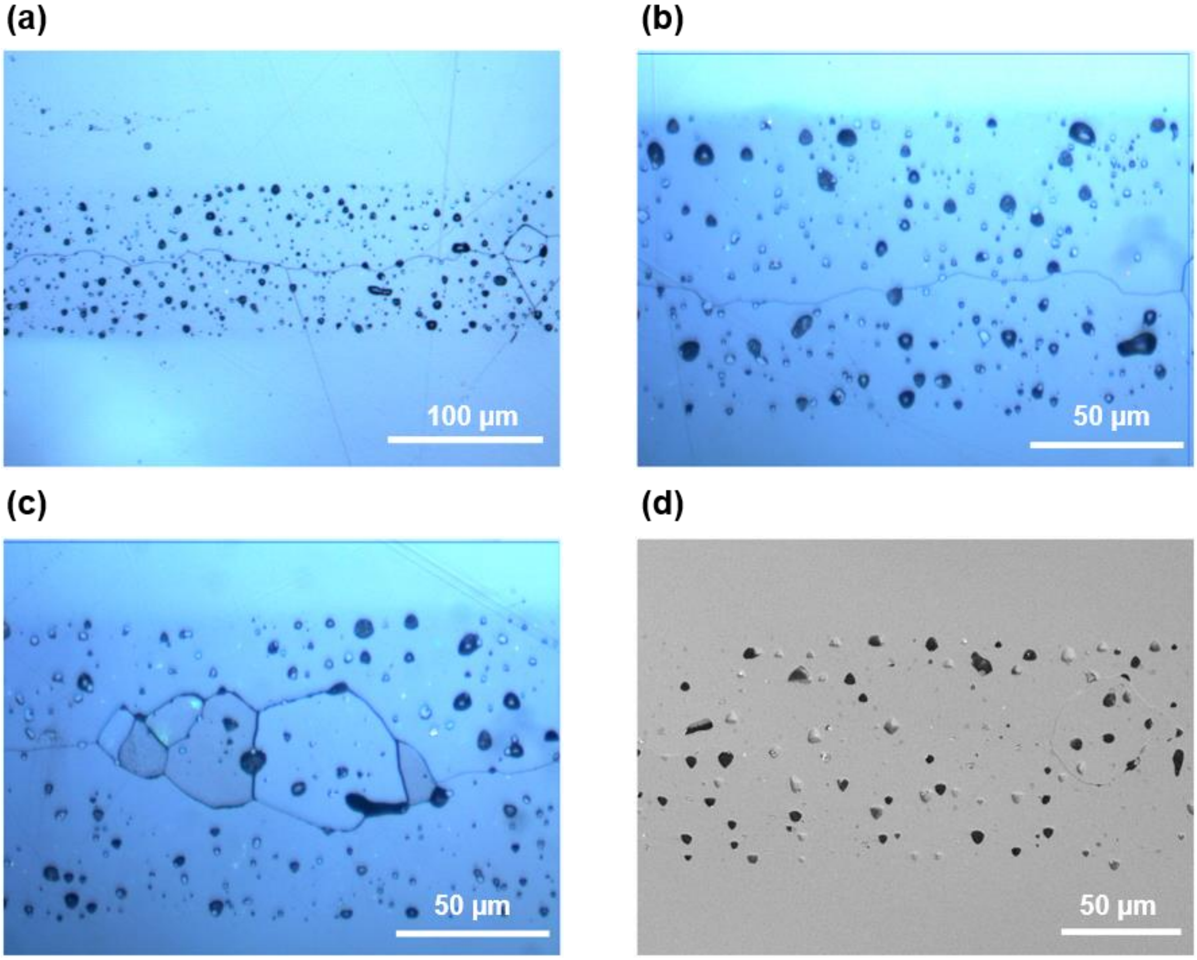

Figure A-1: Structural analysis of O|O bicrystal interface prepared by epitaxial solid-state transformation. Images (a) to (c) depict images taken by optical microscopy and image (d) features an SEM image of the interface. A single interface over a large area is present but, in some parts, individual grains or small amounts of remaining polycrystalline material are still present ((c) and (d)).

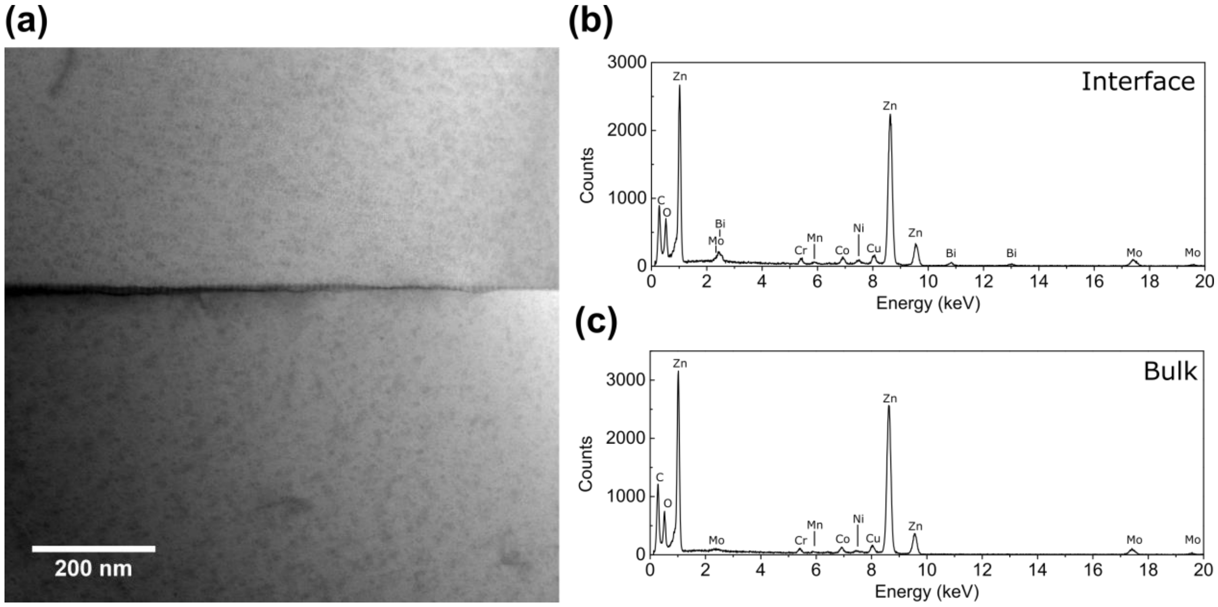

Figure A-2: EDS measurements of the O|O bicrystal at the interface and within the bulk. (a) BF-TEM image featuring the boundary region and the different positions where EDS measurements were taken. At the interface Bi can be detected (b), while within the bulk no Bi signal can be captured (c). In addition, Cr, Mn, Co, and Ni could be detected at the interface and within the bulk material. The Mo and Cu signal originate from the TEM sample holder grid.

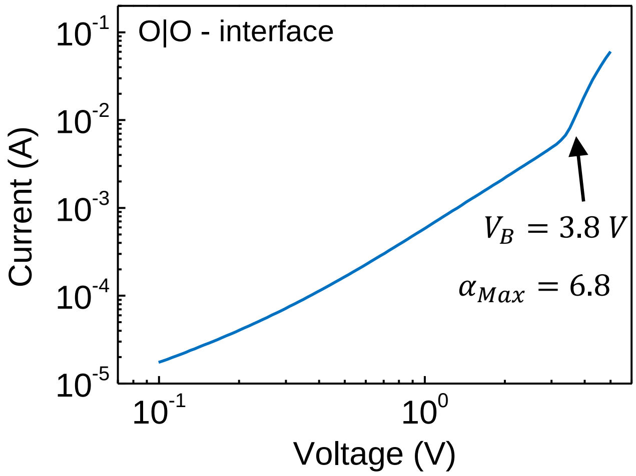

Figure A-3: Current-voltage characteristics of the bicrystals with O|O – interface used for temperature- and stress-dependent conductivity measurements.

References

1. Wang ZL. "Nanopiezotronics." *Advanced Materials* 2007, **19**(6): 889-892.

2. Wen X, Wu W, Pan C, Hu Y, Yang Q, Wang ZL. "Development and progress in piezotronics." *Nano Energy* 2015, **14**: 276-295.

3. Frömling T, Roumeng Y, Mintken M, Adelung R, Rödel J. "Piezotronic sensors." *MRS Bulletin* 2018, **43**(12): 941-945.

4. Ohshima E, Ogino H, Niikura I, Maeda K, Sato M, Ito M, Fukuda T. "Growth of the 2-in-size bulk ZnO single crystals by the hydrothermal method." *Journal of Crystal Growth* 2004, **260**(1-2): 166-170.

5. Wang ZL. "Zinc oxide nanostructures: growth, properties and applications." *Journal of Physics: Condensed Matter* 2004, **16**(25): R829-R858.

6. Yu ET, Dang XZ, Asbeck PM, Lau SS, Sullivan GJ. "Spontaneous and piezoelectric polarization effects in III–V nitride heterostructures." *Journal of Vacuum Science & Technology B: Microelectronics and Nanometer Structures Processing, Measurement, and Phenomena* 1999, **17**(4): 1742.

7. Yu ET, Sullivan GJ, Asbeck PM, Wang CD, Qiao D, Lau SS. "Measurement of piezoelectrically induced charge in GaN/AlGaN heterostructure field-effect transistors." *Applied Physics Letters* 1997, **71**(19): 2794-2796.

8. Ambacher O, Smart J, Shealy JR, Weimann NG, Chu K, Murphy M, Schaff WJ, Eastman LF, Dimitrov R, Wittmer L, Stutzmann M, Rieger W, Hilsenbeck J. "Two-dimensional electron gases induced by spontaneous and piezoelectric polarization charges in N- and Ga-face AlGaN/GaN heterostructures." *Journal of Applied Physics* 1999, **85**(6): 3222-3233.

9. Karrer U, Ambacher O, Stutzmann M. "Influence of crystal polarity on the properties of Pt/GaN Schottky diodes." *Applied Physics Letters* 2000, **77**(13): 2012-2014.

10. Yu ET, Dang XZ, Yu LS, Qiao D, Asbeck PM, Lau SS, Sullivan GJ, Boutros KS, Redwing JM. "Schottky barrier engineering in III–V nitrides via the piezoelectric effect." *Applied Physics Letters* 1998, **73**(13): 1880-1882.

11. Liu Y, Kauser MZ, Nathan MI, Ruden PP, Dogan S, Morkoç H, Park SS, Lee KY. "Effects of hydrostatic and uniaxial stress on the Schottky barrier heights of Ga-polarity and N-polarity n-GaN." *Applied Physics Letters* 2004, **84**(12): 2112-2114.

12. Chung KW, Wang Z, Costa JC, Williamson F, Ruden PP, Nathan MI. "Barrier height change in GaAs Schottky diodes induced by piezoelectric effect." *Applied Physics Letters* 1991, **59**(10): 1191-1193.

13. Strittmatter RP, Beach RA, Brooke J, Preisler EJ, Picus GS, McGill TC. "GaN Schottky diodes for piezoelectric strain sensing." *Journal of Applied Physics* 2003, **93**(9): 5675-5681.

14. Fattahi Comjani F, Willer U, Kontermann S, Schade W. "Influence of the metal-semiconductor contact by energy harvesting from vertically aligned zinc oxide nanowires." *Applied Physics Letters* 2014, **104**(14): 143113.

15. Pintilie L, Alexe M. "Metal-ferroelectric-metal heterostructures with Schottky contacts. I. Influence of the ferroelectric properties." *Journal of Applied Physics* 2005, **98**(12): 124103.

16. Pintilie L, Boerasu I, Gomes MJM, Zhao T, Ramesh R, Alexe M. "Metal-ferroelectric-metal structures with Schottky contacts. II. Analysis of the experimental current-voltage and capacitance-voltage characteristics of Pb(Zr,Ti)O_3 thin films." *Journal of Applied Physics* 2005, **98**(12): 124104.

17. Wang C, Jin K-j, Xu Z-t, Wang L, Ge C, Lu H-b, Guo H-z, He M, Yang G-z. "Switchable diode effect and ferroelectric resistive switching in epitaxial $BiFeO_3$ thin films." *Applied Physics Letters* 2011, **98**(19): 192901.

18. Choi T, Lee S, Choi YJ, Kiryukhin V, Cheong S-W. "Switchable Ferroelectric Diode and Photovoltaic Effect in $BiFeO_3$." *Science* 2009, **324:** 63-66.

19. Hong S, Choi T, Jeon JH, Kim Y, Lee H, Joo HY, Hwang I, Kim J-S, Kang SO, Kalinin SV, Park BH. "Large Resistive Switching in Ferroelectric $BiFeO_3$ Nano-Island Based Switchable Diodes." *Advanced Materials* 2013, **25**(16): 2339-2343.

20. Zhuravlev MY, Sabirianov RF, Jaswal SS, Tsymbal EY. "Giant Electroresistance in Ferroelectric Tunnel Junctions." *Physical Review Letters* 2005, **94**(24): 246802.

21. Garcia V, Fusil S, Bouzehouane K, Enouz-Vedrenne S, Mathur ND, Barthelemy A, Bibes M. "Giant tunnel electroresistance for non-destructive readout of ferroelectric states." *Nature* 2009, **460:** 81-84.

22. Pantel D, Goetze S, Hesse D, Alexe M. "Reversible electrical switching of spin polarization in multiferroic tunnel junctions." *Nature Materials* 2012, **11**(4): 289-293.

23. Wong J, Bundy FP. "Pressure effects on metal oxide varistors." *Applied Physics Letters* 1976, **29**(1): 49-50.

24. Emtage PR. "The physics of zinc oxide varistors." *Journal of Applied Physics* 1977, **48**(10): 4372.

25. Verghese PM, Clarke DR. "Piezoelectric contributions to the electrical behavior of ZnO varistors." *Journal of Applied Physics* 2000, **87**(9): 4430.

26. Baraki R, Novak N, Frömling T, Granzow T, Rödel J. "Bulk ZnO as piezotronic pressure sensor." *Applied Physics Letters* 2014, **105**(11): 111604.

27. Raidl N, Supancic P, Danzer R, Hofstätter M. "Piezotronically Modified Double Schottky Barriers in ZnO Varistors." *Advanced Materials* 2015, **27**(12): 2031-2035.

28. Wang ZL, Song J. "Piezoelectric Nanogenerators Based on Zinc Oxide Nanowire Arrays." *Science* 2006, **312:** 242-246.

29. Wang X, Zhou J, Song J, Liu J, Xu N, Wang ZL. "Piezoelectric Field Effect Transistor and Nanoforce Sensor Based on a Single ZnO Nanowire." *Nano Letters* 2006, **6**(12): 2768-2772.

30. Xu S, Qin Y, Xu C, Wei Y, Yang R, Wang ZL. "Self-powered nanowire devices." *Nat Nanotechnology* 2010, **5**(5): 366-373.

31. Cha SN, Seo JS, Kim SM, Kim HJ, Park YJ, Kim SW, Kim JM. "Sound-Driven Piezoelectric Nanowire-Based Nanogenerators." *Adcanced Materials* 2010, **22**(42): 4726-4730.

32. Li Z, Zhu G, Yang R, Wang AC, Wang ZL. "Muscle-Driven in Vivo Nanogenerator." *Advanced Materials* 2010, **22**(23): 2534-2537.

33. Wu W, Wei Y, Wang ZL. "Strain-Gated Piezotronic Logic Nanodevices." *Advanced Materials* 2010, **22**(42): 4711-4715.

34. Wen X, Wu W, Ding Y, Wang ZL. "Piezotronic Effect in Flexible Thin-Film Based Devices." *Advanced Materials* 2013, **25**(24): 3371-3379.

35. Wu W, Wang L, Li Y, Zhang F, Lin L, Niu S, Chenet D, Zhang X, Hao Y, Heinz TF, Hone J, Wang ZL. "Piezoelectricity of single-atomic-layer MoS_2 for energy conversion and piezotronics." *Nature* 2014, **514**(7523): 470-474.

36. Zhang Y, Liu Y, Wang ZL. "Fundamental Theory of Piezotronics." *Advanced Materials* 2011, **23**(27): 3004-3013.

37. Zhou J, Gu Y, Fei P, Mai W, Gao Y, Yang R, Bao G, Wang ZL. "Flexible Piezotronic Strain Sensor." *Nano Letters* 2008, **8**(9): 3035-3040.

38. Jenkins K, Nguyen V, Zhu R, Yang R. "Piezotronic Effect: An Emerging Mechanism for Sensing Applications." *Sensors* 2015, **15**(9): 22914-22940.

39. Lee S, Hinchet R, Lee Y, Yang Y, Lin Z-H, Ardila G, Montès L, Mouis M, Wang ZL. "Ultrathin Nanogenerators as Self-Powered/Active Skin Sensors for Tracking Eye Ball Motion." *Advanced Functional Materials* 2014, **24**(8): 1163-1168.

40. Bao R, Wang C, Dong L, Yu R, Zhao K, Wang ZL, Pan C. "Flexible and Controllable Piezo-Phototronic Pressure Mapping Sensor Matrix by ZnO NW/p-Polymer LED Array." *Advanced Functional Materials* 2015, **25**(19): 2884-2891.

41. Jaffe B, Cook WR, Jaffe H. *Piezoelectric Ceramics*. Academic Press Inc., 1971.

42. Shimura F. *Semiconductor Silicon Crystal Technology*. Academic Press Inc., 1989.

43. Kashiwaba Y, Katahira F, Haga K, Sekiguchi T, Watanabe H. "Hetero-epitaxial growth of ZnO thin films by atmospheric pressure CVD method." *Journal of Crystal Growth* 2000, **221:** 431-434.

44. Scharowsky E. "Optische und elektrische Eigenschaften von ZnO-Einkristallen mit ZnO-Überschuß." *Zeitschrift für Physik* 1953, **135:** 318-330.

45. Reynolds DC, Litton CW, Look DC, Hoelscher JE, Claflin B, Collins TC, Nause J, Nemeth B. "High-quality, melt-grown ZnO single crystals." *Journal of Applied Physics* 2004, **95**(9): 4802-4805.

46. Matsuoka M. "Nonohmic Properies of Zinc Oxide Ceramics." *Japanese Journal of Applied Physics* 1971, **10**(6): 736-746.

47. Dal Corso A, Posternak M, Resta R, Baldereschi A. "Ab initio study of piezoelectricity and spontaneous polarization in ZnO." *Physical Review B* 1994, **50**(15): 10715-10721.

48. Marcoc H, Özgür Ü. General Properties of ZnO. *Zinc Oxide*. WILEY-VHC Verlag GmbH & Co. KGaA, 2009.

49. Bragg WL, Darbyshire JA. "The structure of thin films of certain metallic oxides." *Transactions of the Faraday Society* 1932, **28:** 522-529.

50. Ashrafi A, Jagadish C. "Review of zincblende ZnO: Stability of metastable ZnO phases." *Journal of Applied Physics* 2007, **102**(7): 071101.

51. Bates CH, White WB, Roy R. "New High-Pressure Polymorph of Zinc Oxide." *Science* 1962, **137**(3534): 993-993.

52. Karzel H, Potzel W, Köfferlein M, Schiessl W, Steiner M, Hiller U, Kalvius GM, Blaha P, Schwarz K, Pasternak MP. "Lattice dynamics and hyperfine interactions in ZnO and ZnSe at high external pressures." *Physical Review B* 1996, **53**(17): 11427.

53. Jaffe JE, Hess AC. "Hartree-Fock study of phase changes in ZnO at high pressure." *Physical Review B* 1993, **48**(11): 7903-7909.

54. Schröer P, Krüger P, Pollmann J. "First-principles calculation of the electronic structure of the wurtzite semiconductors ZnO and ZnS." *Physical Review B* 1993, **47**(12): 6971-6980.

55. Li W-J, Shi E-R, Zhong W-Z, Yin Z-W. "Growth mechanism and growth habit of oxide crystals." *Journal of Crystal Growth* 1999, **203**(1-2): 186-196.

56. Iwanaga H, Shibata N, Nittono O, Kasuga M. "Crystal growth in c direction and crystallographic polarity in ZnO crystals." *Journal of Crystal Growth* 1978, **45**: 228-232.

57. Mariano AN, Hanneman RE. "Crystallographic Polarity of ZnO Crystals." *Journal of Applied Physics* 1963, **34**(2): 384-388.

58. Romano G, Mantini G, Di Carlo A, D'Amico A, Falconi C, Wang ZL. "Piezoelectric potential in vertically aligned nanowires for high output nanogenerators." *Nanotechnology* 2011, **22**(46): 465401.

59. Alexe M, Senz S, Schubert MA, Hesse D, Gösele U. "Energy Harvesting Using Nanowires?" *Advanced Materials* 2008, **20**(21): 4021-4026.

60. Hutson AR. "Piezoelectricity and conductivity in ZnO and CdS." *Physical Review Letters* 1960, **4**(10): 505-507.

61. Kobiakov IB. "Elastic, piezoelectric and dielectric properties of ZnO and CdS single crystals in a wide range of temperatures." *Solid State Communications* 1980, **35**(3): 305-310.

62. Sohn JI, Cha SN, Song BG, Lee S, Kim SM, Ku J, Kim HJ, Park YJ, Choi BL, Wang ZL, Kim JM, Kim K. "Engineering of efficiency limiting free carriers and an interfacial energy barrier for an enhancing piezoelectric generation." *Energy & Environmental Science* 2013, **6**(1): 97-104.

63. Posternak M, Baldereschi A, Catellani A, Resta R. "Ab Initio Study of the Spontaneous Polarization of Pyroelectric BeO." *Physical Review Letters* 1990, **64**(15): 1777-1780.

64. Massidda S, Resta R, Posternak M, Baldereschi A. "Polarization and dynamical charge of ZnO within different one-particle schemes." *Physical Review B* 1995, **52**(24): R16977-R16980.

65. Reynolds DC, Look DC, Jogai B, Litton CW, Cantwell G, Harsch WC. "Valence-band ordering in ZnO." *Physical Review B* 1999, **60**(4): 2340.

66. Srikant V, Clarke DR. "On the optical band gap of zinc oxide." *Journal of Applied Physics* 1998, **83**(10): 5447-5451.

67. Maeda K, Sato M, Niikura I, Fukuda T. "Growth of 2 inch ZnO bulk single crystal by the hydrothermal method." *Semiconductor Science and Technology* 2005, **20**(4): S49-S54.

68. Zhang SB, Wei SH, Zunger A. "Intrinsic n-type versus p-type doping asymmetry and the defect physics of ZnO." *Physical Review B* 2001, **63**: 075205.

69. Ellmer K, Klein A, Rech B. *Transparent Conductive Zinc Oxide: Basics and Applications in Thin Film Solar Cells*. Springer Berlin Heidelberg, 2008.

70. Look DC. "Recent advances in ZnO materials and devices." *Materials Science and Engineering: B* 2001, **80**: 383-387.

71. Janotti A, Van de Walle CG. "Fundamentals of zinc oxide as a semiconductor." *Reports on Progress in Physics* 2009, **72**(12): 126501.

72. McCluskey MD, Jokela SJ. "Defects in ZnO." *Journal of Applied Physics* 2009, **106**(7): 071101.

73. Erhart P, Albe K, Klein A. "First-principles study of intrinsic point defects in ZnO: Role of band structure, volume relaxation, and finite-size effects." *Physical Review B* 2006, **73**(20): 205203.

74. Janotti A, Van de Walle CG. "Native point defects in ZnO." *Physical Review B* 2007, **76**(16): 165202.

75. Janotti A, Van de Walle CG. "Oxygen vacancies in ZnO." *Applied Physics Letters* 2005, **87**(12): 122102.

76. Look DC, Hemsky JW, Sizelove JR. "Residual Native Shallow Donor in ZnO." *Physical Review Letters* 1999, **82**(12): 2552-2555.

77. Tuomisto F, Saarinen K, Look DC, Farlow GC. "Introduction and recovery of point defects in electron-irradiated ZnO." *Physical Review B* 2005, **72**(8): 085206.

78. Janotti A, Van de Walle CG. "New insights into the role of native point defects in ZnO." *Journal of Crystal Growth* 2006, **287**(1): 58-65.

79. Vlasenko LS, Watkins GD. "Optical detection of electron paramagnetic resonance for intrinsic defects produced in ZnO by 2.5-MeV electron irradiation in situ at 4.2 K." *Physical Review B* 2005, **72**(3): 035203.

80. Erhart P, Albe K. "Diffusion of zinc vacancies and interstitials in zinc oxide." *Applied Physics Letters* 2006, **88**(20): 201918.

81. Wenas WW, Yamada A, Takahashi K, Yoshino M, Konagai M. "Electrical and optical properties of boron-doped ZnO thin films for solar cells grown by metalorganic chemical vapor deposition." *Journal of Applied Physics* 1991, **70**(11): 7119-7123.

82. Fu Q, Hao S, Shen B, Duan X, Na H. "Preparation and optical–electrical properties of Al-doped ZnO films." *Research on Chemical Intermediates* 2012, **39**(2): 527-536.

83. Fortunato E, Raniero L, Silva L, Goncalves A, Pimentel A, Barquinha P, Aguas H, Pereira L, Goncalves G, Ferreira I. "Highly stable transparent and conducting gallium-doped zinc oxide thin films for photovoltaic applications." *Solar Energy Materials & Solar Cells* 2008, **92**(12): 1605-1610.

84. McCluskey MD, Jokela SJ. "Sources of n-type conductivity in ZnO." *Physica B: Condensed Matter* 2007, **401-402**: 355-357.

85. Van de Walle CG. "Hydrogen as a Cause of Doping in Zinc Oxide." *Physical Review Letters* 2000, **85**(5): 1012-1015.

86. Thomas DG, Lander JJ. "Hydrogen as a Donor in Zinc Oxide." *The Journal of Chemical Physics* 1956, **25**(6): 1136-1142.

87. Hofmann DM, Hofstaetter A, Leiter F, Zhou H, Henecker F, Meyer BK, Orlinskii SB, Schmidt J, Baranov PG. "Hydrogen: A Relevant Shallow Donor in Zinc Oxide." *Physical Review Letters* 2002, **88**(4): 045504.

88. Vines L, Monakhov EV, Schifano R, Mtangi W, Auret FD, Svensson BG. "Lithium and electrical properties of ZnO." *Journal of Applied Physics* 2010, **107**(10): 103707.

89. Mead CA. "Schottky Barrier Gated Field-Effect Transistor." *Proceedings of the IEEE* 1966, **54:** 307-308.

90. Schottky WH. "Halbleitertheorie der Sperrschicht." *Die Naturwissenschaften* 1938, **26**(52): 843-843.

91. Mott NF. "The theory of crystal rectifiers." *Proceedings of the Royal Society London* 1939, **171**(944): 27-38.

92. Sze SM. MOSFET and Related Devices. *Semiconductor Devices Physics and Technology*, vol. 2. Wiley & Sons, Inc, 1985.

93. Tung RT. "Recent advances in Schottky barrier concepts." *Materials Science and Engineering R* 2001, **35:** 1-138.

94. Tung RT. "Chemical Bonding and Fermi Level Pinning at Metal-Semiconductor Interfaces." *Physical Review Letters* 2000, **84**(26): 6078-6081.

95. Bardeen J. "Surface States and Rectification at a Metal Semi-Conductor Contact." *Physical Review* 1947, **71**(10): 717-727.

96. Tung RT. "Formation of an electric dipole at metal-semiconductor interfaces." *Physical Review B* 2001, **64**(20): 205310.

97. Tung RT. "Electron transport at metal-semiconductor interfaces: General theory." *Physical Review B* 1992, **45**(23): 13509-13523.

98. Brillson LJ, Lu Y. "ZnO Schottky barriers and Ohmic contacts." *Journal of Applied Physics* 2011, **109**(12): 121301.

99. Pearton SJ, Norton DP, Ip K, Heo YW, Steiner T. "Recent progress in processing and properties of ZnO." *Superlattices and Microstructures* 2003, **34**(1-2): 3-32.

100. Mead CA. "Surface Barriers on ZnSe and ZnO." *Physics Letters* 1965, **18:** 218.

101. Neville RC, Mead CA. "Surface Barriers on Zinc Oxide." *Journal of Applied Physics* 1970, **41**(9): 3795-3800.

102. Simpson JC, Cordaro JF. "Characterization of deep levels in zinc oxide." *Journal of Applied Physics* 1988, **63**(5): 1781-1783.

103. Brillson LJ, Mosbacker HL, Hetzer MJ, Strzhemechny Y, Jessen GH, Look DC, Cantwell G, Zhang J, Song JJ. "Dominant effect of near-interface native point defects on ZnO Schottky barriers." *Applied Physics Letters* 2007, **90**(10): 102116.

104. Allen MW, Durbin SM. "Influence of oxygen vacancies on Schottky contacts to ZnO." *Applied Physics Letters* 2008, **92**(12): 122110.

105. Coppa BJ, Davis RF, Nemanich RJ. "Gold Schottky contacts on oxygen plasma-treated, n-type ZnO(000-1)." *Applied Physics Letters* 2003, **82**(3): 400-402.

106. Mosbacker HL, Strzhemechny YM, White BD, Smith PE, Look DC, Reynolds DC, Litton CW, Brillson LJ. "Role of near-surface states in ohmic-Schottky conversion of Au contacts to ZnO." *Applied Physics Letters* 2005, **87**(1): 012102.

107. Coppa BJ, Fulton CC, Hartlieb PJ, Davis RF, Rodriguez BJ, Shields BJ, Nemanich RJ. "In situ cleaning and characterization of oxygen- and zinc-terminated, n-type, ZnO{0001} surfaces." *Journal of Applied Physics* 2004, **95**(10): 5856-5864.

108. Brillson LJ. "Transition in Schottky Barrier Formation with Chemical Reactivity." *Physical Review Letters* 1978, **40**(4): 260-263.

109. Mosbacker HL, Zgrabik C, Hetzer MJ, Swain A, Look DC, Cantwell G, Zhang J, Song JJ, Brillson LJ. "Thermally driven defect formation and blocking layers at metal-ZnO interfaces." *Applied Physics Letters* 2007, **91**(7): 072102.

110. Brillson LJ, Mosbacker HL, Hetzer MJ, Strzhemechny Y, Look DC, Cantwell G, Zhang J, Song JJ. "Surface and near-surface passivation, chemical reaction, and Schottky barrier formation at ZnO surfaces and interfaces." *Applied Surface Science* 2008, **254**(24): 8000-8004.

111. Kim H, Sohn A-r, Kim D-W. "Barrier Inhomogeneity in Ag Schottky Contacts to Bulk ZnO Grown by Different Methods." *Journal of the Korean Physical Society* 2012, **60**(3): 509-513.

112. Dong Y, Fang ZQ, Look DC, Cantwell G, Zhang J, Song JJ, Brillson LJ. "Zn- and O-face polarity effects at ZnO surfaces and metal interfaces." *Applied Physics Letters* 2008, **93**(7): 072111.

113. Allen MW, Miller P, Reeves RJ, Durbin SM. "Influence of spontaneous polarization on the electrical and optical properties of bulk, single crystal ZnO." *Applied Physics Letters* 2007, **90**(6): 062104.

114. Lee J-M, Kim K-K, Park S-J, Choi W-K. "Low-resistance and nonalloyed ohmic contacts to plasma treated ZnO." *Applied Physics Letters* 2001, **78**(24): 3842-3844.

115. Sheng H, Emanetoglu N, S. M, Feng S, Lu Y. "Nonalloyed Al Ohmic Contacts to $Mg_xZn_{1-x}O$." *Journal of Electronic Materials* 2002, **31**(7): 811-814.

116. Michaelson HB. "The work function of the elements and its periodicity." *Journal of Applied Physics* 1977, **48**(11): 4729-4733.

117. Moormann H, Kohl D, Heiland G. "Work function and band bending on clean cleaved zinc oxide surfaces." *Surface Science* 1979, **80**: 261-264.

118. Kim H-K, Kim K-K, Park S-J, Seong T-Y, Adesida I. "Formation of low resistance nonalloyed Al/Pt ohmic contacts on n-type ZnO epitaxial layer." *Journal of Applied Physics* 2003, **94**(6): 4225.

119. Chiou Y-Z, Lin K-W. "Annealing Effect of Transparent Ohmic Contacts to n-ZnO Epitaxial Films." *Journal of The Electrochemical Society* 2006, **153**(2): G141.

120. Stengel M, Spaldin NA. "Origin of the dielectric dead layer in nanoscale capacitors." *Nature* 2006, **443**: 679-682.

121. Stengel M, Vanderbilt D, Spaldin NA. "Enhancement of ferroelectricity at metal-oxide interfaces." *Nature Materials* 2009, **8**(5): 392-397.

122. Liu W, Zhang A, Zhang Y, Wang ZL. "First principle simulations of piezotronic transistors." *Nano Energy* 2015, **14**: 355-363.

123. Liu W, Zhang A, Zhang Y, Wang ZL. "Density functional studies on wurtzite piezotronic transistors: influence of different semiconductors and metals on piezoelectric charge distribution and Schottky barrier." *Nanotechnology* 2016, **27**(20): 205204.

124. Shannon JM. "Control of Schottky barrier height using highly doped surface layers." *Solid-State Electronics* 1976, **19**: 537-543.

125. Shannon JM. "Increasing the effective height of a Schottky barrier using low-energy ion implantation." *Applied Physics Letters* 1974, **25**(1): 75-77.

126. Shannon JM. "Reducing the effective height of a Schottky barrier using low-energy ion implantation." *Applied Physics Letters* 1974, **24**(8)**:** 369-371.

127. Stengel M, Aguado-Puente P, Spaldin NA, Junquera J. "Band alignment at metal/ferroelectric interfaces: Insights and artifacts from first principles." *Physical Review B* 2011, **83**(23).

128. Card H, Rhoderick E. "The effect of an interfacial layer on minority carrier injection in forward-biased silicon Schottky diodes." *Solid-State Electronics* 1973, **16:** 365-374.

129. Cowley AM, Sze SM. "Surface States and Barrier Height of Metal-Semiconductor Systems." *Journal of Applied Physics* 1965, **36**(10)**:** 3212-3220.

130. Hu Y, Klein BD, Su Y, Niu S, Liu Y, Wang ZL. "Temperature Dependence of the Piezotronic Effect in ZnO Nanowires." *Nano Letters* 2013, **13**(11)**:** 5026-5032.

131. Lu S, Qi J, Gu Y, Liu S, Xu Q, Wang Z, Liang Q, Zhang Y. "Influence of the carrier concentration on the piezotronic effect in a ZnO/Au Schottky junction." *Nanoscale* 2015, **7**(10)**:** 4461-4467.

132. Lu S, Liao Q, Qi J, Liu S, Liu Y, Liang Q, Zhang G, Zhang Y. "The enhanced performance of piezoelectric nanogenerator via suppressing screening effect with Au particles/ZnO nanoarrays Schottky junction." *Nano Research* 2016, **9**(2)**:** 372-379.

133. Gupta TK. "Application of Zinc Oxide Varistors." *Journal of the American Ceramic Society* 1990, **73**(7)**:** 1817-1840.

134. Clarke DR. "Varistor Ceramics." *Journal of the American Ceramic Society* 1999, **82:** 485-502.

135. Pike GE. "Semiconducting Polycrystalline Ceramics." *Materials Science and Technology* 1994, **11:** 731-754.

136. Blatter G, Greuter F. "Carrier transport through grain boundaries in semiconductors." *Physical Review B* 1986, **33**(6)**:** 3952-3966.

137. Greuter F, Blatter G. "Electrical properties of grain boundaries in polycrystalline compound semiconductors." *Semiconductor Science and Technology* 1990, **5:** 111-137.

138. Greuter F. "Electrically active interfaces in ZnO varistor." *Solid State Ionics* 1995, **75:** 67-78.

139. Stucki F, Greuter F. "Key role of oxygen at zinc oxide varistor grain boundaries." *Applied Physics Letters* 1990, **57**(5)**:** 446-448.

140. Selim FA, Gupta TK, Hower PL, Carlson WG. "Low voltage ZnO varistor: Device process and defect model." *Journal of Applied Physics* 1980, **51**(1)**:** 765-768.

141. Gambino JP, Kingery WD, Pike GE, Philipp HR, Levinson LM. "Grain boundary electronic states in some simple ZnO varistors." *Journal of Applied Physics* 1987, **61**(7)**:** 2571-2574.

142. Winston RA, Cordaro JF. "Grain-boundary interface electron traps in commercial zinc oxide varistors." *Journal of Applied Physics* 1990, **68**(12)**:** 6495-6500.

143. Greuter F, Blatter G, Rossinelli M, Schmückle F. "Bulk and grain boundary defects in polycrystalline ZnO." *Materials Science Forum* 1986, **10-12:** 235-240.

144. Sato Y, Buban JP, Mizoguchi T, Shibata N, Yodogawa M, Yamamoto T, Ikuhara Y. "Role of Pr Segregation in Acceptor-State Formation at ZnO Grain Boundaries." *Physical Review Letters* 2006, **97**(10).

145. Carlsson JM, Domingos HS, Bristowe PD, Hellsing B. "An Interfacial Complex in ZnO and its Influence on Charge Transport." *Physical Review Letters* 2003, **91**(16)**:** 165506.

146. Domingos HS, Carlsson JM, Bristowe PD, Hellsing B. "The Formation of Defect Complexes in a ZnO Grain Boundary." *Interface Science* 2004, **12:** 227-234.

147. Sato Y, Oba F, Yamamoto T, Ikuhara Y, Sakuma T. "Current–Voltage Characteristics across [0001] Twist Boundaries in Zinc Oxide Bicrystals." *Journal of the American Ceramic Society* 2002, **85:** 2142-2144.

148. Sato Y, Oba F, Yodogawa M, Yamamoto T, Ikuhara Y. "Current-Voltage Characteristic and Grain Boundary Structure in Undoped and Pr and Co Doped ZnO Bicrystals." *Materials Science Forum* 2005, **475-479:** 3867-3870.

149. Sato Y, Yamamoto T, Ikuhara Y. "Atomic Structures and Electrical Properties of ZnO Grain Boundaries." *Journal of the American Ceramic Society* 2007, **90**(2)**:** 337-357.

150. Leach C. "Grain boundary structures in zinc oxide varistors." *Acta Materialia* 2005, **53**(2)**:** 237-245.

151. Lee J-S, Maier J. "High Barrier Effects of $(000\bar{1})|(000\bar{1})$ Zinc Oxide Bicrystals: Implication for Varistor Ceramics with Inversion Boundaries." *Journal of Materials Research* 2005, **20**(08)**:** 2101-2109.

152. Park J-L, Park C, Kim D-Y, Jo W, Park C-J, Jeon S-Y, Lee J-S. "Polarity engineering in polycrystalline ZnO by inversion boundaries." *Applied Physics Letters* 2009, **94**(25)**:** 252108.

153. Kim J, Kimura T, Yamaguchi T. "Effect of Bismuth Oxide Content on the Sintering of Zinc Oxied." *Journal of the American Ceramic Society* 1989, **72:** 1390.

154. Wong J. "Sintering and varistor characteristics of $ZnO\text{-}Bi_2O_3$ ceramics." *Journal of Applied Physics* 1980, **51**(8)**:** 4453.

155. Olsson E, Dunlop GL, Österlund R. "Development of interfacial microstructure during cooling of a ZnO varistor material." *Journal of Applied Physics* 1989, **66**(10)**:** 5072-5077.

156. Mahan GD. "Intrinsic defects in ZnO varistors." *Journal of Applied Physics* 1983, **54**(7)**:** 3825-3832.

157. Sonder E, Austin MM, Kinser DL. "Effect of oxidizing and reducing atmospheres at elevated temperatures on the electrical properties of zinc oxide varistors." *Journal of Applied Physics* 1983, **54**(6)**:** 3566-3572.

158. Li J, Li S, Liu F, Alim MA. "The influence of heat-treatment on the current-voltage behavior of the $ZnO\text{-}Bi_2O_3$ based varistors." *Journal of Materials Science: Materials in Electronics* 2006, **17**(3)**:** 211-217.

159. Blatter G, Greuter F. "Electrical breakdown at semiconductor grain boundaries." *Physical Review B* 1986, **34**(12)**:** 8555-8572.

160. Mahan GD, Levinson LM, Philipp HR. "Theory of conduction in ZnO varistors." *Journal of Applied Physics* 1979, **50**(4)**:** 2799.

161. Tao M, Ai B, Dorlanne O, Loubiere A. "Different “single grain junctions” within a ZnO varistor." *Journal of Applied Physics* 1987, **61**(4)**:** 1562.

162. Olsson E, Dunlop GL. "Characterization of individual interfacial barriers in a ZnO varistor material." *Journal of Applied Physics* 1989, **66**(8)**:** 3666.

163. Pike GE. Electronic properties of ZnO Varistors: A new Model. In: Leamy GE, Pike GE, Seager CH (eds). *Grain Boundaries in Semiconductors*. Elsevier Science Publishing Company Inc.: Amsterdam, 1982, pp 369-380.

164. Pike GE, Kurtz SR, Gourley PL, Philipp HR, Levinson LM. "Electroluminescence in ZnO varistors: Evidence for hole contributions to the breakdown mechanism." *Journal of Applied Physics* 1985, **57**(12)**:** 5512-5518.

165. Gupta TK, Mathur MP, Carlson WG. "Effect of externaly applied pressure on zinc oxide varistors." *Journal of Electronic Materials* 1977, **6**(5)**:** 483-497.

166. Dorlanne O, Ai B, Destruel P, Loubière A. "Electrical characteristics of zinc oxide varistors subjected to hydrostatic pressure." *Journal of Applied Physics* 1985, **57**(12)**:** 5535-5538.

167. Doshchanov KM. "Piezoresistance of grain boundaries in piezoelectric crystals." *Soviet Physics: Semiconductors* 1977, **11**(9)**:** 1067-1068.

168. Baraki R, Novak N, Hofstätter M, Supancic P, Rödel J, Frömling T. "Varistor piezotronics: Mechanically tuned conductivity in varistors." *Journal of Applied Physics* 2015, **118**(8)**:** 085703.

169. Emtage PR. "Statistics and grain size in zinc oxide varistors." *Journal of Applied Physics* 1979, **50**(11)**:** 6833-6837.

170. Wang H, Bartkowiak M, Modine FA, Dinwiddie RB, Boatner LA, Mahan GD. "Nonuniform Heating in Zinc Oxide Varistors Studied by Infrared Imaging and Computer Simulation." *Journal of the American Ceramic Society* 1998, **81**(8)**:** 2013-2022.

171. Raidl N, Hofstätter M, Supancic P. "Piezotronic Effect on Electrical Characteristics of Bulk ZnO Varistors " *Advanced Engineering Materials* 2017, **19**(4)**:** 1600677.

172. Canessa E, Nguyen VL. "Non-linear I-V characteristics of double Schottky barriers and polycrystalline semiconductors " *Physica B: Condensed Matter* 1992, **179:** 335-341.

173. Bartkowiak M, Mahan GD, Modine FA, Alim MA. "Influence of ohmic grain boundaries in ZnO varistors." *Journal of Applied Physics* 1996, **79**(1)**:** 273.

174. Bartkowiak M, Mahan GD, Modine FA, Alim MA, Lauf R, McMillan A. "Voronoi network model of ZnO varistors with different types of grain boundaries." *Journal of Applied Physics* 1996, **80**(11)**:** 6516.

175. van Kemenade JTC, Eijnthoven RK. "Direct determination of barrier voltage in ZnO varistors." *Journal of Applied Physics* 1979, **50**(2)**:** 938-941.

176. Einzinger R. "Grain junction properties of ZnO varistors." *Applications of Surface Science* 1979, **3:** 390-408.

177. Nan C-W, Clarke DR. "Effect of Variations in Grain Size and Grain Boundary Barrier Heights on the Current-Voltage Characteristics of ZnO Varistors." *Journal of the American Ceramic Society* 1996, **79**(12)**:** 3185-3192.

178. Castro MS, Nunez GM, Resasco DE, Aldao CM. "Prebreakdown Conduction in ZnO Varistors." *Journal of the American Ceramic Society* 1992, **75**(4)**:** 800-804.

179. Schwing U, Hoffmann B. "ZnO single crystals with an intermediate layer of metal oxides—A macroscopic varistor model." *Journal of Applied Physics* 1980, **51**(8)**:** 4558.

180. Schwing U, Hoffmann B. "Model experiments describing the microcontact of ZnO varistors." *Journal of Applied Physics* 1985, **57**(12)**:** 5372.

181. Cheng C, He J, Hu J. "Naturally asymmetrical double-Schottky barrier model: Based on observation of bicrystal." *Applied Physics Letters* 2012, **101**(17)**:** 173508.

182. Cheng C, He J, Hu J. "Observation of the charged defect migration that causes the degradation of double-Schottky barriers using a nondestructive quantitative profiling technique." *Applied Physics Letters* 2014, **105**(13)**:** 133508.

183. Cheng C, Hu J, He J. "Characterization of dielectric behavior in ZnO electroceramic: Superior grain boundary, inferior grain boundary and grain." *Materials Letters* 2014, **132:** 240-242.

184. Lee J-S, Kim Y, Shin E-C, Maier J. "Positive temperature coefficient resistor behavior in praseodymium-doped ZnO (0001)|(0001) boundaries." *Applied Physics Letters* 2010, **96**(20)**:** 202104.

185. Zhou J, Fei P, Gu Y, Mai W, Gao Y, Yang R, Bao G, Wang ZL. "Piezoelectric-Potential-Controlled Polarity-Reversible Schottky Diodes and Switches of ZnO Wires." *Nano Letters* 2008, **8**(11)**:** 3973-3977.

186. Mantini G, Gao Y, D'Amico A, Falconi C, Wang ZL. "Equilibrium piezoelectric potential distribution in a deformed ZnO nanowire." *Nano Research* 2009, **2**(8)**:** 624-629.

187. Wang ZL. "Energy Harvesting Using Piezoelectric Nanowires-A Correspondence on "Energy Harvesting Using Nanowires?" by Alexe et al." *Advanced Materials* 2009, **21**(13)**:** 1311-1315.

188. Allen MW, Mendelsberg RJ, Reeves RJ, Durbin SM. "Oxidized noble metal Schottky contacts to n-type ZnO." *Applied Physics Letters* 2009, **94**(10)**:** 103508.

189. Schader FH. Mechanical Stability of the Electromechanical Properties and Phase Transitions in Lead-Containing and Lead-Free Ferroelectrics. PhD thesis, TU Darmstadt, Darmstadt, 2016.

190. Sawyer CB, Tower C. "Rochelle Salt as a Dielectric." *Physical Review* 1930, **35**(3)**:** 269-273.

191. Marks RA, Taylor ST, Mammana E, Gronsky R, Glaeser AM. "Directed assembly of controlled-misorientation bicrystals." *Nature Materials* 2004, **3**(10)**:** 682-686.

192. Gehringer M. Mechanisch modulierbare Leitfähigkeit in ZnO-basierten Einkristall-Polykristall-Einkristall Strukturen. Bachelor thesis, TU Darmstadt, 2017.

193. Keil P, Frömling T, Klein A, Rödel J, Novak N. "Piezotronic effect at Schottky barrier of a metal-ZnO single crystal interface." *Journal of Applied Physics* 2017, **121**(15)**:** 155701.

194. Hummel RE. *Electronic Properties of Materials*. Springer: New York, NY, 2011.

195. Ip K, Thaler GT, Yang H, Youn Han S, Li Y, Norton DP, Pearton SJ, Jang S, Ren F. "Contacts to ZnO." *Journal of Crystal Growth* 2006, **287**(1)**:** 149-156.

196. Werner JH, Güttler HH. "Barrier inhomogeneities at Schottky contacts." *Journal of Applied Physics* 1991, **69**(3)**:** 1522-1533.

197. Cheung SK, Cheung NW. "Extraction of Schottky diode parameters from forward current-voltage characteristics." *Applied Physics Letters* 1986, **49**(2)**:** 85-87.

198. Polyakov AY, Smirnov NB, Kozhukhova EA, Vdovin VI, Ip K, Heo YW, Norton DP, Pearton SJ. "Electrical characteristics of Au and Ag Schottky contacts on n-ZnO." *Applied Physics Letters* 2003, **83**(8)**:** 1575.

199. Barsoukov E, Ross Mcdonald J. *Impedance Spectroscopy Theory, Experiment, and Applications*. John Wiley & Sons, Inc: Hoboken, New Jersey, 2005.

200. Irvine JTS, Sinclair DC, West AR. "Electroceramics: Characterization by Impedance Spectroscopy." *Advanced Materials* 1990, **2**(3)**:** 132-138.

201. Proskuryakov YY, Durose K, Al Turkestani MK, Mora-Seró I, Garcia-Belmonte G, Fabregat-Santiago F, Bisquert J, Barrioz V, Lamb D, Irvine SJC, Jones EW. "Impedance spectroscopy of thin-film CdTe/CdS solar cells under varied illumination." *Journal of Applied Physics* 2009, **106**(4)**:** 044507.

202. Yim C, McEvoy N, Duesberg GS. "Characterization of graphene-silicon Schottky barrier diodes using impedance spectroscopy." *Applied Physics Letters* 2013, **103**(19)**:** 193106.

203. Yim C, McEvoy N, Kim HY, Rezvani E, Duesberg GS. "Investigation of the Interfaces in Schottky Diodes Using Equivalent Circuit Models." *ACS Applied Materials & Interfaces* 2013, **5**(15)**:** 6951-6958.

204. Chauhan KR, Mukhopadhyay I. "On the electrical and interface properties of nanostructured CdTe Schottky diodes electrodeposited from an ionic liquid medium." *Journal of Applied Physics* 2014, **115**(22)**:** 224506.

205. Look DC, Reynolds DC, Sizelove JR, Jones RL, Litton CW, Cantwell G, Harsch WC. "Electrical properties of bulk ZnO." *Solid State Communications* 1998, **105**(6)**:** 399-401.

206. Klein A, Green DJ. "Interface Properties of Dielectric Oxides." *Journal of the American Ceramic Society* 2016, **99**(2)**:** 369-387.

207. Chen F, Klein A. "Polarization dependence of Schottky barrier heights at interfaces of ferroelectrics determined by photoelectron spectroscopy." *Physical Review B* 2012, **86**(9).

208. Novak N, Keil P, Frömling T, Schader FH, Martin A, Webber KG, Rödel J. "Influence of metal/semiconductor interface on attainable piezoelectric and energy harvesting properties of ZnO." *Acta Materialia* 2019, **162:** 277-283.

209. Sze SM, Ng KK. Physics and Properties of Semiconductors - A Review. *Physics of Semiconductor Devices*, 3 edn. John Wiley & Sons Inc: Hoboken, New Jersey, 2007.

210. Wang X, Yu R, Peng W, Wu W, Li S, Wang ZL. "Temperature Dependence of the Piezotronic and Piezophototronic Effects in a-axis GaN Nanobelts." *Advanced Materials* 2015, **27**(48)**:** 8067-8074.

211. Yu R, Wang X, Wu W, Pan C, Bando Y, Fukata N, Hu Y, Peng W, Ding Y, Wang ZL. "Temperature Dependence of the Piezophototronic Effect in CdS Nanowires." *Advanced Functional Materials* 2015, **25**(33)**:** 5277-5284.

212. Damjanovic D. "Stress and frequency dependence of the direct piezoelectric effect in ferroelectric ceramics." *Journal of Applied Physics* 1997, **82**(4)**:** 1788-1797.

213. Roundy S, Wright PK, Rabaey J. "A study of low level vibrations as a power source for wireless sensor nodes." *Computer Communications* 2003, **26:** 1131-1144.

214. Li H, Tian C, Deng ZD. "Energy harvesting from low frequency applications using piezoelectric materials." *Applied Physics Reviews* 2014, **1:** 041301.

215. Hu Y, Xu C, Zhang Y, Lin L, Snyder RL, Wang ZL. "A Nanogenerator for Energy Harvesting From a Rotating Tire and its Application as a Self-Powered Pressure/Speed Sensor." *Advanced Materials* 2011, **23**(35)**:** 4068-4071.

216. Lee S, Bae S-H, Lin L, Yang Y, Park C, Kim S-W, Cha SN, Kim H, Park YJ, Wang ZL. "Super-Flexible Nanogenerator for Energy Harvesting from Gentle Wind and as an Active Deformation Sensor." *Advanced Functional Materials* 2013, **23**(19)**:** 2445-2449.

217. Fan FR, Tang W, Wang ZL. "Flexible Nanogenerators for Energy Harvesting and Self-Powered Electronics." *Advanced Materials* 2016, **28**(22)**:** 4283-4305.

218. Zhang Z, Liao Q, Zhang X, Zhang G, Li P, Lu S, Liu S, Zhang Y. "Highly efficient piezotronic strain sensors with symmetrical Schottky contacts on the monopolar surface of ZnO nanobelts." *Nanoscale* 2015, **7**(5)**:** 1796-1801.

219. Keil P, Baraki R, Novak N, Rödel J, Frömling T. "Gauge factors for piezotronic stress sensor in polycrystalline ZnO." *Journal of Physics D: Applied Physics* 2017, **50**(17)**:** 175106.

220. Keil P, Trapp M, Novak N, Frömling T, Kleebe HJ, Rödel J. "Piezotronic Tuning of Potential Barriers in ZnO Bicrystals." *Advanced Materials* 2018, **30**(10).

221. Lee J-S, Wiederhorn SM. "Effects of Polarity on Grain-Boundary Migration in ZnO." *Journal of the American Ceramic Society* 2004, **87**(7)**:** 1319-1323.

222. Hwang J-H, Mason TO, Vinayak PD. "Microanalytical Determination of ZnO Solidus and Liquidus Boundaries in the ZnO-Bi_2O_3 System." *Journal of the American Ceramic Society* 1994, **77**(6)**:** 499-504.

223. Sato Y, Yodogawa M, Yamamoto T, Shibata N, Ikuhara Y. "Dopant-segregation-controlled ZnO single-grain-boundary varistors." *Applied Physics Letters* 2005, **86**(15)**:** 152112.

224. Eda K, Iga A, Matsuoka M. "Current Creep in Nonohmic ZnO Ceramics." *Japanese Journal of Applied Physics* 1979, **18**(5)**:** 997-998.

225. Mukae K, Tsuda K, Nagasawa I. "Capacitance-vs-voltage characteristics of ZnO varistors." *Journal of Applied Physics* 1979, **50:** 4475-4476.

226. Saeger CH, Pike GE. "Grain boundary states and varistor behavior in silicon bicrystals." *Applied Physics Letters* 1979, **35:** 709-711.

227. Taylor WE, Odell NH, Fan HY. "Grain Boundary Barriers in Germanium." *Physical Review* 1952, **88**(4)**:** 867-875.

228. Schipani F, Aldao CM, Ponce MA. "Schottky barriers measurements through Arrhenius plots in gas sensors based on semiconductor films." *AIP Advances* 2012, **2**(3)**:** 032138.

229. Zhang DH, Brodie DE. "Effects of annealing ZnO films prepared by ion-beam-assisted reactive deposition." *Thin Solid Films* 1994, **238:** 95-100.

230. Kurchania R, Kale GM. "Oxygen potential in molten tin and Gibbs energy formation of SnO_2 employing and oxygen sensor." *Journal of Materials Research* 2000, **15**(7)**:** 1576-1582.

231. Kim ED, Oh MH, Kim CH. "Effects of annealing on the grain boundary potential barrier of ZnO varistors." *Journal of Materials Science* 1986, **21:** 3491-3496.

232. Keil P, Gehringer M, Frömling T, Novak N, Rödel J. "ZnO-based single crystal-polycrystal structures for piezotronic applications." *Journal of the American Ceramic Society* 2019, in print.

233. Hennings DFK, Hartung R, Reijnen PJL. "Grain Size Control in Low-Voltage Varistor." *Journal of the American Ceramic Society* 1990, **73**(3)**:** 645-648.

Acknowledgement

First and foremost, I want to thank Prof. Jürgen Rödel for giving me the opportunity to complete this doctoral thesis within his working group (NAW). Besides giving great scientific guidance, his exceptional organization of the working group could not provide a better environment for writing a thesis. I am grateful for having such a mentor as an example for my scientific as well as development.

I want to wholeheartedly thank “my” postdocs, Dr. Till Frömling and Dr. Nikola Novak who were directly involved in the ZnO project. I really enjoyed working with you every day and I have learned a lot from you in our numerous discussions. Writing papers, discussing results, planning experiments, supervising students, and visiting conferences were both excellent and challenging tasks I was happy to experience with you. Thank you for reading my manuscript and providing fast and valuable feedback. Thank you, Nikola, for also being available and for providing advice, even after you moved back to Slovenia. Thank you for the great time I could share with you!

I want to thank Prof. Andreas Klein for being the second reviewer of this work. I am also grateful to Prof. Hans-Joachim Kleebe and Prof. Jörg J. Schneider for contributing as examiners.

Furthermore, I want to thank all my collaborators with whom I could work together during the past years. I am grateful to Prof. Hans-Joachim Kleebe and Maximilian Trapp for TEM imaging of the bicrystal interfaces. I want to thank Prof. Andreas Klein for insightful discussions on Schottky contacts and for organization of the PAK 928 and the ZnO workshop in Edesheim. Philipp Wendel, thank you for your support with the sputter deposition of doped ZnO layers. I am also indebted to Prof. Kyle G. Webber, Dr. Florian Schader, and Dr. Alexander Martin for hosting us at FAU Erlangen-Nürnberg to measure the piezoelectric properties of ZnO. Further, I want to thank Prof. Bai-Xiang Xu and Ziqi Zhou as well as PD Dr. Erion Gjonaj and Kyle Taylor for insightful discussions on the theoretical description of the piezotronic effect at ZnO bicrystal interfaces and grain boundaries of polycrystals. Many thanks to Prof. Marin Alexe for giving me the opportunity to visit your laboratories in Warwick as a guest scientist.

The experimental work of this thesis would not have been possible without great technical support. Thank you, Daniel Isaia, for constructing the well working mini-load frame from just a sketch as starting point and for general support with all stress dependent measurements. I also want to thank Patrick Breckner for writing the LabView program as well as for any help regarding the IT infrastructure. I also acknowledge the help of Michael Heyse who trained me in sample preparation, especially when it came to delicate issues, your input was highly valuable. Gila Völzke always supported me with all kinds of administrative procedures. Thank you for keeping the group running as smoothly as it does.

I also had the chance to supervise two great students: Maximilian Gehringer and Daniel Bremecker. It was a pleasure to work with you on not always easy tasks. I also want to thank Maximilian Gehringer for supporting me as a HIWI in the laboratory. I am happy to see that you two will now continue as PhD students in our group.

A special thank-you goes to all the NAW members who not only were colleagues, but also became friends. Florian and Sebastian, it was an awesome experience to master all challenges starting from the first Bachelor course to the completion of a PhD thesis together with you. I had a great time with you, and I am sure, there is more to come. Jan, I am glad to have met you here at NAW. I enjoyed every discussion with you on any topic and admire your motivational skills, when it comes to organizing sport events or other group activities. Every working group would be glad to have a guy like you! I also want to thank Marion for all the nice discussions, it was great to have someone next door to always talk to. Virginia, Yoshi, Lukas, and Qaisar, it was an honor to share an office with you. I am very grateful to all current and former NAW members for creating such a pleasant as well as productive working environment.

Finally, I want to thank my family for their love and support during my whole life. I thank my parents Heike and Gerhard for giving me the chance to enjoy this education with all the help and support one could wish for. Furthermore, I want to thank my brother Tom for always being there for me.

For financial support under the project number RO954/28-1, I want to thank the German Research Foundation.

Curriculum vitae

Personal details

Name	Peter Keil
Date of birth	01.03.1990
Place of birth	Darmstadt
Nationality	German

Education

05/2015 – 05/2019	Nichtmetallisch-Anorganische Werkstoffe, Prof. Dr. Jürgen Rödel, Technische Universität Darmstadt: PhD student in materials science
10/2009 – 04/2015	Material und Geowissenschaften, Technische Universität Darmstadt: Student of materials science (B.Sc. and M.Sc.)
08/2006 – 07/2009	Gymnasiale Oberstufe, Albert-Einstein-Schule, Groß-Bieberau: Abitur

Work experience

05/2015 – 12/2018	Nichtmetallisch-Anorganische Werkstoffe, Prof. Dr. Jürgen Rödel, Technische Universität Darmstadt: Research associate and PhD student
05/2017 – 07/2017	Department of Physics, Prof. Dr. Marin Alexe, University of Warwick: Visiting fellow

Publications

P. Keil, M. Trapp, N. Novak, T. Frömling, H-J. Kleebe, J. Rödel; *Piezotronic Tuning of Potential Barriers in ZnO Bicrystals*; Advanced Materials 2018, 30, 1705573.

P. Keil, T. Frömling, A. Klein, J. Rödel, N. Novak; *Piezotronic effect at Schottky barrier of a metal-ZnO single crystal interface*; Journal of Applied Physics 2017, 121, 155701.

P. Keil, M. Gehringer, T. Frömling, N. Novak, J. Rödel; *ZnO-based single crystal-polycrystal structures for piezotronic applications*; Journal of the American Ceramic Society 2019, in print.

P. Keil, R. Baraki, N. Novak, J. Rödel, T. Frömling; *Gauge factors for piezotronic stress sensor in polycrystalline ZnO*; Journal of Physics D: Applied Physics 2017, 50, 175106.

N. Novak, **P. Keil**, T. Frömling, F.H. Schader, A. Martin, K.G. Webber, J. Rödel; *Influence of metal/semiconductor interface on attainable piezoelectric and energy harvesting properties of ZnO*; Acta Materialia 2019, 162, 277-283.

B-X. Xu, Z-Q. Zhou, **P. Keil**, T. Frömling; *An extended grain boundary barrier height model including the impact of internal electric field;* AIP Advances, 8, 115126.

Y. Pu, L. Zhang, **P. Keil**, N. Novak, T. Frömling; *Impact of mechanical stress on barium titanate-positive temperature coefficient resistive material*; Journal of Materials Science 2018, 53, 16243-16251.

Conference contributions

P. Keil, M. Trapp, N. Novak, T. Frömling, H-J. Kleebe, J. Rödel; *Piezotronic performance of doped bicrystal interfaces*; 4th international conference on nanogenerators and piezotronics; 05/2018; Seoul, Korea; poster contribution.

P. Keil, N. Novak, T. Frömling, J. Rödel; *Mechanistic insight into varistor piezotronics using doped ZnO bicrystals*; 3rd euro intelligent materials; 06/2017; Kiel, Germany; oral contribution.

P. Keil, N. Novak, T. Frömling, J. Rödel; *How to improve the impact of piezoelectric charges in ZnO-based piezotronic systems*; 9th international workshop on ZnO; 10-11/2016; Taipei, Taiwan; oral contribution.

P. Keil, N. Novak, T. Frömling, J. Rödel; *Mechanistic insight into varistor piezotronics using doped ZnO bicrystals*; ISAF-ECAPED-PFM Conference; 08/2016; Darmstadt, Germany; poster contribution.

Y. Li, M. Höfling, **P. Keil**, J. Rödel; Hexagonal evolution of an amphitheater-like lateral crack below Vickers indent in ZnO; ACerS Basic Science Division: Ceramographic Exhibit and Competition, Columbus, USA